

International Journal of

# **Rotating Machinery**

Special Issue

Active and Passive Flow Control of Turbomachines

Guest Editors: N. Sitaram, K. Funazaki, and Seyed G. Saddoughi



---

# **Active and Passive Flow Control of Turbomachines**

International Journal of Rotating Machinery

---

## **Active and Passive Flow Control of Turbomachines**

Guest Editors: N. Sitaram, K. Funazaki,  
and Seyed G. Saddoughi



Copyright © 2013 Hindawi Publishing Corporation. All rights reserved.

This is a special issue published in “International Journal of Rotating Machinery.” All articles are open access articles distributed under the Creative Commons Attribution License, which permits unrestricted use, distribution, and reproduction in any medium, provided the original work is properly cited.

## Editorial Board

S. Acharya, USA  
A. A. Afjeh, USA  
H. Joon Ahn, Korea  
R. S. Amano, USA  
F. E. Ames, USA  
L. San Andres, USA  
J. Antoni, France  
S. V. Apte, USA  
H. J. Bauer, Germany  
D. E. Bently, USA  
D. E. Bohn, Germany  
G. BOIS, France  
C. E. Brennen, USA  
Mustafa Canakci, Turkey  
G. M. Carlomagno, Italy  
M. K. Chyu, USA  
A. Corsini, Italy  
N. Feng, Australia  
D. P. Fleming, USA  
Koji Fujimoto, Japan  
Luis Gato, Portugal  
G. A. Gerolymos, France  
J. P. Gostelow, UK  
C. Hah, USA  
E. J. Hahn, Australia  
A. Hamed, USA  
J-C. Han, USA  
Hiroshi Hayami, Japan  
R. C. Hendricks, USA

H. Heshmat, USA  
D. T. Hountalas, Greece  
Z. Huang, China  
N. Iki, Japan  
Tariq Iqbal, Canada  
M. Ishizuka, Japan  
Takuzo Iwatsubo, Japan  
David Japikse, USA  
Y. Kaneko, Japan  
K. Kawaike, Japan  
F. Ken-ichi, Japan  
T. Seop Kim, Korea  
S. A. Kinnas, USA  
R. G. Kirk, USA  
Ching-Pang Lee, USA  
A. W. Lees, UK  
R. F. Martinez-Botas, UK  
Shigenao Maruyama, Japan  
H. Masjuki, Malaysia  
Eric Maslen, USA  
Fabian Mauss, Germany  
David U. Mba, UK  
Jiun-Jih Miau, Taiwan  
Akira Murata, Japan  
Agnes Muszynska, USA  
V. T. Nagaraj, USA  
M. Razi Nalim, USA  
E.Y.K. Ng, Singapore  
Osamu Nozaki, Japan

Yutaka Ohta, Japan  
T. Okamura, Japan  
Yoji Okita, Japan  
I. Paraschivoiu, Canada  
R. Payri, Spain  
Paolo Pennacchi, Italy  
Sergio Preidikman, USA  
R. B. Rivir, USA  
T. Sattelmayer, Germany  
J. T. Sawicki, USA  
M. T. Schobeiri, USA  
E. Sciubba, Italy  
T. W. Simon, USA  
O. SINGH, India  
S. Jin Song, Korea  
T. Sonoda, Japan  
F. Sun, UK  
Ken-Ichiro Takeishi, Japan  
H. A. Toliyat, USA  
Wei Tong, USA  
Y. Tsujimoto, Japan  
Ting Wang, USA  
T. Watanabe, Japan  
B. Weigand, Germany  
Dave Wisler, USA  
S. L. K. Wittig, Germany  
K. Yamaguchi, Japan  
Y. Yokono, Japan

# Contents

**Active and Passive Flow Control of Turbomachines**, N. Sitaram, K. Funazaki, and Seyed G. Saddoughi  
Volume 2013, Article ID 372181, 1 page

**Experimental Investigation and Passive Flow Control of a Cavitating Centrifugal Pump**,  
Spyridon D. Kyparissis and Dionissios P. Margaris  
Volume 2012, Article ID 248082, 8 pages

**Effects of Input Voltage on Flow Separation Control for Low-Pressure Turbine at Low Reynolds Number by Plasma Actuators**, Takayuki Matsunuma and Takehiko Segawa  
Volume 2012, Article ID 902548, 10 pages

**Study and Control of a Radial Vaned Diffuser Stall**, Aurélien Marsan, Isabelle Trébinjac, Sylvain Coste, and Gilles Leroy  
Volume 2012, Article ID 549048, 12 pages

**Leakage Characteristic of Helical Groove Seal Designed in Reactor Coolant Pump**, Meng Zhang, Xiao-fang Wang, Sheng-li Xu, and Shuo Yin  
Volume 2012, Article ID 619459, 8 pages

**Control of Surge in Centrifugal Compressor by Using a Nozzle Injection System: Universality in Optimal Position of Injection Nozzle**, Toshiyuki Hirano, Takanori Uchida, and Hoshio Tsujita  
Volume 2012, Article ID 259293, 8 pages

**Encounters with Vortices in a Turbine Nozzle Passage**, J. P. Gostelow, A. Mahallati, W. E. Carscallen, and A. Rona  
Volume 2012, Article ID 928623, 10 pages

**Aerothermal Analysis of a Turbine Casing Impingement Cooling System**, Riccardo Da Soghe, Bruno Facchini, Mirko Miccio, and Antonio Andreini  
Volume 2012, Article ID 103583, 10 pages

## Editorial

# Active and Passive Flow Control of Turbomachines

**N. Sitaram,<sup>1</sup> K. Funazaki,<sup>2</sup> and Seyed G. Saddoughi<sup>3</sup>**

<sup>1</sup> Department of Mechanical Engineering, Indian Institute of Technology Madras, Chennai 600 036, India

<sup>2</sup> Department of Mechanical Engineering, Iwate University, Morioka, Iwate, Japan

<sup>3</sup> Department of Aero-Thermal & Mechanical Systems, GE Global Research, 1 Research Circle, Niskayuna, NY 12309, USA

Correspondence should be addressed to N. Sitaram; [nsitaram@iitm.ac.in](mailto:nsitaram@iitm.ac.in)

Received 24 December 2012; Accepted 24 December 2012

Copyright © 2013 N. Sitaram et al. This is an open access article distributed under the Creative Commons Attribution License, which permits unrestricted use, distribution, and reproduction in any medium, provided the original work is properly cited.

Turbomachines are used in a wide range of applications. Increasing the efficiency and operating range of turbomachines reduces fuel consumption of gas turbine power plants and other applications. Over the years, many attempts have been made to achieve these objectives. The present special issue addresses these goals with special emphasis on active and passive flow control techniques.

This special issue compiles 7 original research articles that describe active and passive flow control techniques applied to different types of turbomachines. The theme for this special issue is set by J. P. Gostelow et al. They describe various types of vortices encountered in a transonic turbine nozzle blade passage. Active and passive control of these vortices is essential to improve the performance of turbines.

There are two more papers on control of turbine flows. The paper by R. Da Soghe et al. describes aerothermal analysis of a turbine casing impingement cooling system. T. Matsunuma and T. Segawa systematically varied the input voltage of plasma actuators to reattach the simulated boundary layer on the suction surface of a turbine at a low Reynolds number. The low-pressure turbine of aircraft gas turbine power plants operating at high altitudes operates at low Reynolds numbers. Losses in turbines operating at low Reynolds numbers increase rapidly due to large separation occurring on the suction surfaces of the turbine blades. Many researchers used dielectric barrier discharge (DBD) plasma actuators to actively control flow separation, tip clearance flows, and so forth in turbines and other turbomachinery components. The present paper by T. Matsunuma and T. Segawa is a great addition to the available data that addresses the effects of input voltage to plasma actuators on flow control effectiveness.

Two papers describe active and passive flow control techniques applied to centrifugal compressors. A. Marsan et al. numerically investigated boundary layer suction technique applied to the radial diffuser of a transonic centrifugal compressor. They had presented an efficient control technique, which used a suction mass flow rate of 0.1% of global mass flow to increase the compressor operating range by 40%. T. Hirano et al. experimentally investigated a passive nozzle injection system to control surge and rotating stall in high speed centrifugal compressors. They demonstrated optimum circumferential position of the injection nozzle.

S. Kyparissis and D. Margaritis tested impellers with three different leading edge angles to optimize the leading edge angle to reduce cavitation development and enhance the performance of a centrifugal pump.

Active and passive flow control techniques are being extensively investigated in the primary components of turbomachinery. However to further improve the performance of turbomachinery, active and passive flow control techniques need to be applied to secondary components of turbomachines, such as seals. The last paper of the special issue by M. Zhang et al. addresses leakage flow characteristics of seals used in reactor coolant pumps. They had numerically shown that helical groove seal controls the leakage along the front surface of the impeller face due to its higher resistance than the circumferential grooved seal.

It is hoped that this special issue will provide useful information to wide readership from academia, industry and research establishments and inspire new and more efficient control techniques.

N. Sitaram  
K. Funazaki  
Seyed G. Saddoughi

## Research Article

# Experimental Investigation and Passive Flow Control of a Cavitating Centrifugal Pump

**Spyridon D. Kyparissis and Dionissios P. Margaritis**

*Fluid Mechanics Laboratory, Mechanical Engineering and Aeronautics Department, University of Patras, 26500 Patras, Greece*

Correspondence should be addressed to Spyridon D. Kyparissis, [kypariss@mech.upatras.gr](mailto:kypariss@mech.upatras.gr)

Received 17 July 2012; Revised 15 November 2012; Accepted 6 December 2012

Academic Editor: N. Sitaram

Copyright © 2012 S. D. Kyparissis and D. P. Margaritis. This is an open access article distributed under the Creative Commons Attribution License, which permits unrestricted use, distribution, and reproduction in any medium, provided the original work is properly cited.

Passive flow control techniques are used to improve the flow field and efficiency of centrifugal pumps and turbomachines, in general. An important phenomenon that mechanical engineers have to take into account is cavitation. It leads to the decrease of the pump performance and total head. In the present experimental study, a centrifugal pump is investigated in cavitating conditions. A passive flow control is realized using three different blade leading edge angles in order to reduce the cavitation development and enhance the pump performance. The experiments are carried out in a pump test rig specially designed and constructed, along with the impellers. The head drop and total efficiency curves are presented in order to examine the effect of the blade leading edge angle on the cavitation and pump performance. Finally, the vapour distribution along with the blades is illustrated for the tested blade leading edge angles.

## 1. Introduction

Cavitation is a very complex phenomenon including phase changes and viscous effects. When the local pressure within a flow with water as medium becomes equal to the vaporization pressure of the water, bubbles begin to form and are further transported to regions of higher pressure where they collapse. This bubble collapse can cause material damage and erosion.

Various researchers have considerably contributed in studying the cavitation in centrifugal pumps, applying passive flow control techniques and realizing a series of experiments. On the other hand, there is a limited number of works regarding the effect of the blade leading edge angle on the pump cavitation. Hirschi et al. [1] presented the results obtained with a 3D numerical method allowing the prediction of the cavitation behaviour of a centrifugal pump and compared this prediction to model tests. Hofmann et al. [2] studied experimentally the cavitation of two centrifugal pumps that can hold different runner geometries as well as different leading edge geometries within the same runner. Frobenius et al. [3] realized numerical simulations and experimental investigations of the cavitating flow through

a centrifugal pump impeller of low specific speed. Coutier-Delgosha et al. [4] investigated a special test pump with two-dimensional curvature blade geometry in cavitating and noncavitating conditions using different experimental techniques.

Siljegovic et al. [5] concluded that passive flow control can effectively modulate flow conditions in a capillary driven microfluidic device. Ulas [6] designed and studied experimentally two cavitating venturis to deliver the desired mass flow rates for specific conditions. Escaler et al. [7] carried out an experimental investigation in order to evaluate the detection of cavitation in actual hydraulic turbines. Japikse et al. [8] realized a series of tests and improved the stability of compressors and turbopumps using passive flow control. Luo et al. [9] studied experimentally the effect of impeller inlet geometry on performance improvement for a centrifugal pump. Wu et al. [10] carried out an experimental study in order to analyze the cavitation of a centrifugal pump and its effect on hydrodynamic performance during transient operation. Kyparissis and Margaritis [11–13] studied experimentally and computationally a centrifugal pump with double-arc synthetic blade design method in cavitating and noncavitating conditions, applying different rotational speeds.



The present experimental study and passive flow control are concerned with the effect of the blade leading edge angle on the cavitation of a centrifugal pump applying the double-arc synthetic blade design method [14–16], with rotational speed of 1200 rpm and flow rate of 35 m<sup>3</sup>/h. The experiments are carried out in a pump test rig specially designed and constructed, along with the impellers. The test section allows optical observation of the flow field and cavitation with the aid of the stroboscopic light source. The head drop and total efficiency curves are presented in order to investigate the effect of the blade leading edge angle on the cavitation and pump performance. In addition, the vapour distribution along with the blades is depicted for the tested blade leading edge angles.

## 2. Experimental Rig and Procedure

The experimental study is performed using the pump test rig shown in Figure 1. The supplying tank (1) of the pumping installation is filled with water from the water supply. The pressure at the examined pump inlet is measured by the absolute pressure transducer (2). Furthermore, the study of cavitation is realized applying a wide range of pressures at the pump inlet that can be set by changing the pressure in the supply tank with the aid of a vacuum pump (3). The fluid temperature is measured by a temperature sensor (4) and is kept almost constant and equal to 25°C. The fluid level in the supply tank is read from the level meter (5) and the fluid-free surface pressure is measured by a vacuum-pressure gauge (6). The pump flow rate is measured using the electromagnetic flowmeter (7). Moreover, the flow rate regulation is obtained by throttling a butterfly valve (8) installed at the discharge pipe. The differential pressure between the pump inlet and outlet is measured by the differential pressure transducer (9). The pump is driven by a three-phase AC electric motor (10) of 2.2 kW and maximum rotational speed of 1410 rpm. The rotational speed can be continuously varied by an inverter (11). The pump suction cover (12) and a part of the suction pipe (13) are made from plexiglas. Transparent parts of the pump test rig allow observation of fluid flow inside the impeller and photography of the development of cavitation in flow passage of the impeller. The measurement data are acquired by the data acquisition system and LabVIEW platform (14). The main dimensions of the pump test rig and the regions where the pressure transducers are installed are shown in Figure 2.

For the realization of the cavitation test, the vacuum pump is set in operation and the air is removed from the tank, until a specific value of pressure is recorded by the vacuum-pressure gauge for every measurement. The pump rotational speed is kept constant and the butterfly valve is kept in a given position in order to have constant flow rate. For every measurement, the total head is computed according to the following formula:

$$H = \frac{\Delta p}{\rho g} + \Delta z + \frac{u_d^2 - u_s^2}{2g}. \quad (1)$$

The differential pressure  $\Delta p$  is measured by the differential pressure transducer (9). Moreover, the water density

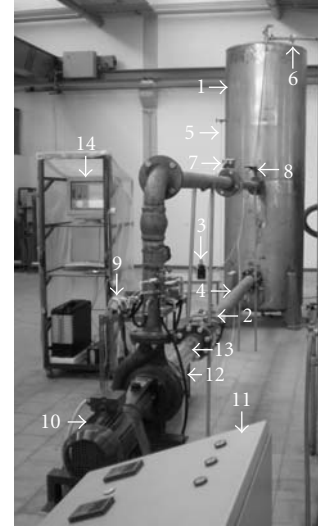


FIGURE 1: The complete experimental setup along with the instrumentation system.

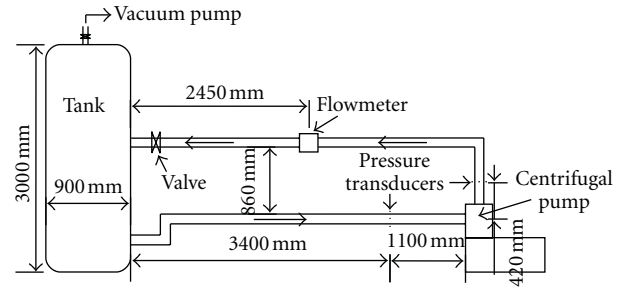


FIGURE 2: The main dimensions of the pump test rig.

for the temperature of 25°C is found  $\rho = 997 \text{ kg/m}^3$ . The discharge velocity  $u_d$  and the suction velocity  $u_s$  are calculated according to the corresponding flow rate  $Q$  measured by the electromagnetic flowmeter (7). The gravitational acceleration is determined as  $g = 9.807 \text{ m/s}^2$  and the elevation difference between the pump inlet and the region where the discharge pressure is measured is calculated  $\Delta z = 0.42 \text{ m}$ .

In addition, the net positive suction head available is computed according to the following equation:

$$\text{NPSHa} = \frac{p_s}{\rho g} + \frac{u_s^2}{2g} - \frac{p_v}{\rho g}. \quad (2)$$

The suction pressure  $p_s$  is measured by the absolute pressure transducer (2) and the vaporization pressure of the water for the temperature of 25°C is found  $p_v = 3290.5 \text{ Pa}$ .

Finally, the total efficiency  $\eta$  is computed according to the following expression:

$$\eta = \frac{\rho g Q H}{\sqrt{3} V I}. \quad (3)$$

The voltage  $V$  and the amperage  $I$  are measured by the inverter (11).

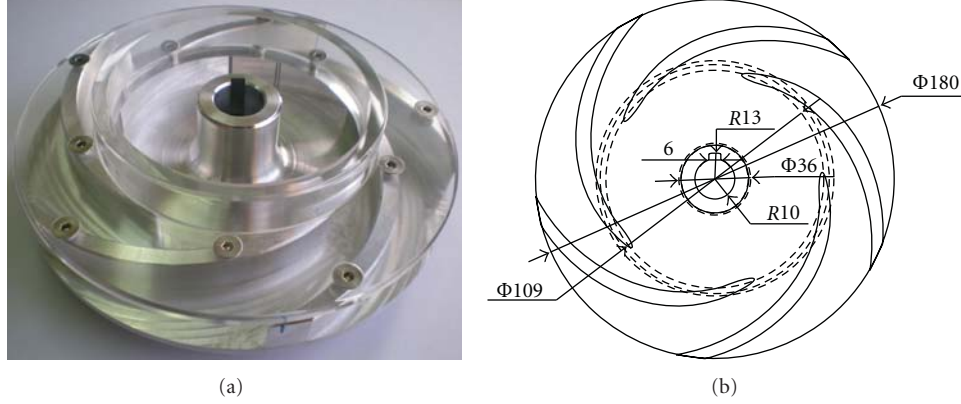


FIGURE 3: The examined impeller geometry and the scaled drawing (in mm) with blade leading edge angle of 9 deg.

Moreover, during every measurement, the cavitation is illustrated using the stroboscopic light. The NPSH value that the first bubble appears, according to the visualization of cavitation, is the net positive suction head required NPSHr.

The measuring equipment consists of an absolute and a differential pressure transducer, a temperature sensor, and an electromagnetic flowmeter. In order to measure the static pressure at the suction side of the pump, an absolute pressure transducer from ABB 2600T series, model 264NS with a base accuracy  $\pm 0.075\%$  is applied. Moreover, the pressure difference between the discharge and suction region of the pump is measured using a differential pressure transducer from ABB 2600T series, model 264DS with a base accuracy  $\pm 0.075\%$ . In addition, temperature is measured with the temperature sensor of the ABB SensyTemp TSP111 series. Furthermore, the measurement of the flow rate is realized using an electromagnetic flowmeter ABB FXE4000 COPA-XE/MAG-XE, model DE41F with a base accuracy  $\pm 0.5\%$ .

The rotational speed of the three phase electric motor can be continuously varied by the inverter Fuji Electric FVR-E9S series.

The study of cavitation is realized using the vacuum pump series LABOPORT N 816.3 KN.45.18. Series N 816.3 diaphragm pumps are double-head, dry-running devices used in a wide range of laboratory applications. They transfer and pump down without contamination.

The measurement data from the pressure transducers, flowmeter, and temperature sensor are acquired by the analog input module cFP-AI-110. The National Instruments cFP-AI-110 is an 8-channel single-ended input module for direct measurement of millivolt, low voltage, or milliamper current signals from a variety of sensors and transmitters. It delivers filtered low-noise analog inputs with 16-bit resolution and 5 S/s sampling rate. Finally, this analog input module is connected to LabVIEW platform (14).

### 3. Blade Design Analysis

**3.1. Impeller Geometry.** Three impeller geometries have been constructed using aluminium alloy 7075-T6, which is composed of zinc as the primary alloying element. It is strong, with strength comparable to many steels and has

TABLE 1: Main characteristics of the tested impellers.

Impeller characteristics	Values
Suction pipe diameter $D_s$ , mm	100
Diameter of the impeller at the suction side $D_1$ , mm	108
Diameter of the impeller at the pressure side $D_2$ , mm	180
Impeller width at the suction side $b_1$ , mm	15.6
Impeller width at the pressure side $b_2$ , mm	15.6
Blade leading edge angle $\beta_1$ , deg	9, 15, 21
Blade trailing edge angle $\beta_2$ , deg	20
Maximum blade thickness $S$ , mm	7.5
Number of blades $z$	5

good fatigue strength and average machinability, but has less resistance to corrosion than many other aluminium alloys. 7075-T6 is a heat temper grade of aluminium alloy 7075. It has an ultimate tensile strength of 510–538 MPa and yield strength of at least 434–476 MPa. In addition, the tested impellers have a removable transparent cover disk made of plexiglas in order to observe the fluid flow and the cavitation, as shown in Figures 3, 4, and 5.

The impellers have been designed according to the dimensions of the Caprari MEC—A2/80A volute, which is installed in the pump test rig. The main characteristics of the three tested impellers are presented in Table 1.

**3.2. Double-Arc Synthetic Method: DASM.** In the present work, the double-arc synthetic method (DASM) [14–16] is applied for the impellers blade design of the centrifugal pump. It is a simple design method that combines two Pfeleiderer's double-arc methods [17]. There are published computational studies [14–16] that compare DASM with the Pfeleiderer's [17] methods and it is observed that a centrifugal pump has better efficiency applying DASM.

As shown in Figure 6, the auxiliary circle  $C_a$  is drawn, according to the following formula:

$$d_1 = D_1 \sin \beta_1, \quad (4)$$

where  $D_1$  is the diameter of the impeller at the suction side and  $\beta_1$  is the blade leading edge angle.

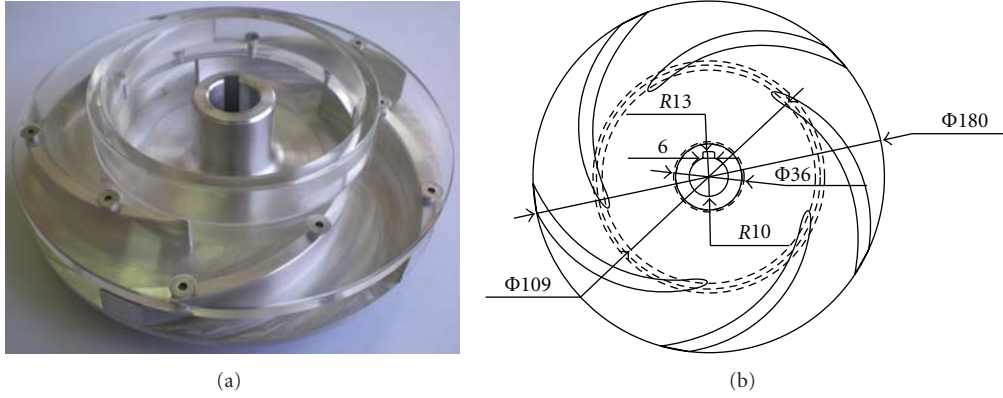


FIGURE 4: The examined impeller geometry and the scaled drawing (in mm) with blade leading edge angle of 15 deg.

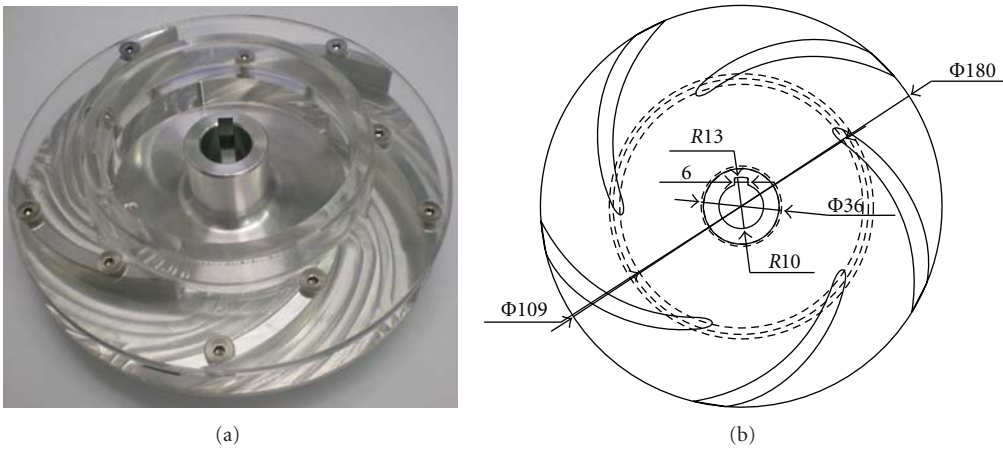


FIGURE 5: The examined impeller geometry and the scaled drawing (in mm) with blade leading edge angle of 21 deg.

The periphery of the suction side is divided to five parts, just as the number of blades  $z$ . The tangents of the auxiliary circle from the points E and C are intersected to the point A. Afterwards, point A is shifted to the point L, which is the center of curvature for the first arc EY and the radius  $R_1$  is the distance of the points E and L, as formulated in the following expression:

$$R_1 = 1.2(AE). \quad (5)$$

The point P is at the extension of the line that connects the points A and C at distance equal to the distance of the points A and E. Applying DASM the point P is shifted to Y, according to the following expression:

$$EY = 0.75 EP. \quad (6)$$

The angle between the lines OY and LY is defined as  $\beta$  and the distance between the points O and Y is defined as  $r$ , as shown in Figure 6. The radius  $R_2$  of the second arc YH is the distance of the points K and Y and is obtained from the following expression:

$$R_2 = \frac{1}{2} \frac{(D_2/2)^2 - r^2}{(D_2/2) \cos \beta_2 - r \cos \beta}, \quad (7)$$

where  $D_2$  is the diameter of the impeller at the pressure side and  $\beta_2$  is the blade trailing edge angle.

## 4. Experimental Results

In the present study, the experimental investigation and passive flow control are realized in order to examine the pump performance and cavitation development for three different blade leading edge angles. Studying the noncavitating performance, the total head and the total efficiency as functions of the flow rate are illustrated in Figures 7 and 8, for the three examined blade leading edge angles and rotational speed of 1200 rpm. As shown in Figure 8, the flow rate to the best efficiency point is approximately 22 m<sup>3</sup>/h for 9 deg, 34 m<sup>3</sup>/h for 15 deg, and 43 m<sup>3</sup>/h for 21 deg.

The total head drops for the rotational speed of 1200 rpm, flow rate of 35 m<sup>3</sup>/h, and three examined blade leading edge angles of 9, 15, and 21 deg are depicted in Figure 9. The ordinate is the total head of the pump, while the abscissa is the net positive suction head available. There are four capital letters in parentheses corresponding to the vapour distributions in Figures 12, 13, 14, and 15. The filled points represent the experimental cases, where cavitation has been developed. It is noticed that as the NPSHa decreases the total head decreases slowly for all the tested blade leading edge angles. As the water in the suction pipe approaches the impeller eye, it has velocity and acceleration. In addition, it has to change its direction to enter the impeller, because

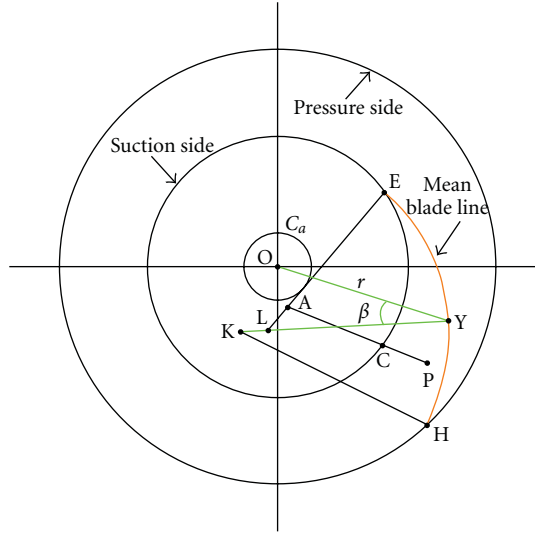


FIGURE 6: Representation of the mean blade line using DASM.

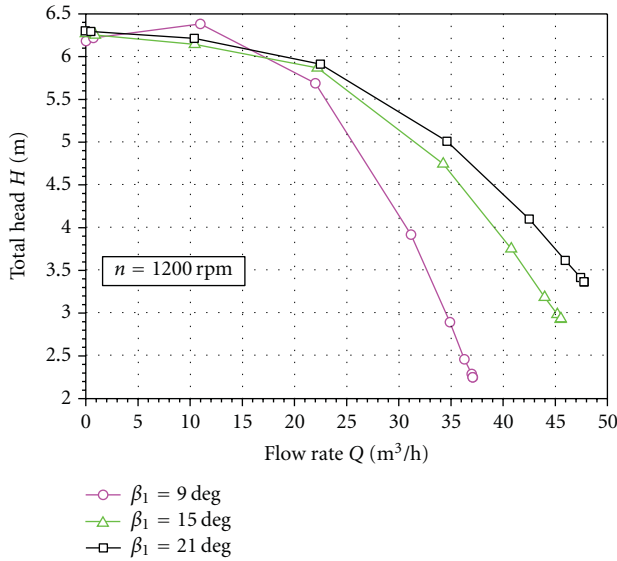


FIGURE 7: The total head as a function of the flow rate, studying the noncavitating performance.

of the blade leading edge angle. Losses in terms of total head occur due to each of the above reasons and because of friction. For the blade leading edge angle of 15 deg, no cavitation is noticed, for the examined pressures at the pump inlet. Nevertheless, there is head drop as the NPSHa decreases, because there are cavitation bubbles, very small and cannot be observed using the stroboscopic light. These bubbles block the flow passage between the blades and cause the head drop. Examining the blade leading edge angle of 9 deg, cavitation starts to be developed for the net positive suction head of 5.13 m, which is the corresponding NPSHr for 9 deg. In addition, testing the 21 deg, the cavitation begins for NPSH = 2.29 m, which is the corresponding NPSHr for 21 deg. Realizing a series of experiments the maximum total head drops for the three above mentioned studied

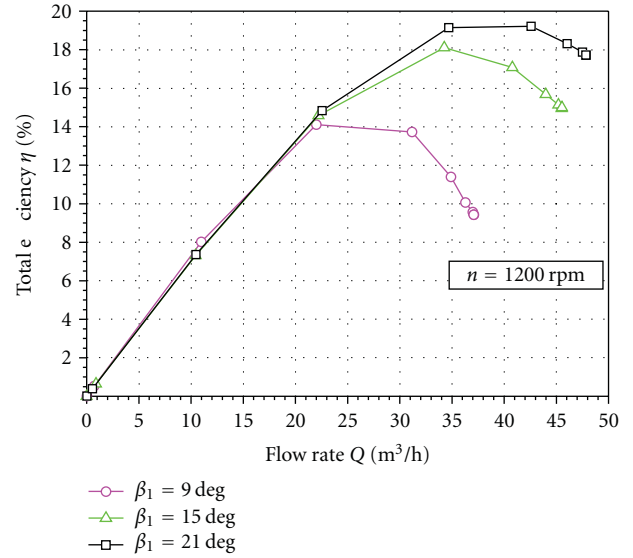


FIGURE 8: The total efficiency as a function of the flow rate, studying the noncavitating performance.

blade leading edge angles are 13.32%, 4.46%, and 6.80%, respectively. For the blade leading edge angles 9 and 21 deg, when cavitation starts to be developed the corresponding head drops are 5.47% and 5.49%, respectively. Thus, it is observed that for both the cases that cavitation begins, the total head is reduced by 5.5% instead of 3% that the Hydraulic Institute defines. The NPSHr can be from 2 to 20 times the 3% that the Hydraulic Institute defines, depending on pump design [18]. The cavity length when the cavitation bubbles appear is measured 4 and 7 mm for 9 and 21 deg, respectively. Moreover, it is noticed that as the blade leading edge angle increases the total head increases as well. Finally, as the net positive suction head available decreases the pump flow rate is kept almost constant, in spite of the cavitation development.

Furthermore, in Figure 10 the change of the total head with the blade leading edge angle is depicted, for three different values of the net positive suction head available. Figure 10 contributes to the recording of the total head values in respect of the change of the blade leading edge angle. It is observed that as the blade leading edge angle increases, the total head increases as well. For the blade leading edge angles between 15 and 21 deg, the total head is almost the same for the net positive suction head available values of 6 and 9 m. Finally, for the lowest examined value of the net positive suction head available, the total head has the lowest values for all the examined blade leading edge angles, because as the net positive suction head decreases the total head decreases as well, as shown in Figure 9.

In Figure 11 the change of the total efficiency with the net positive suction head available is presented, for the three examined blade leading edge angles, rotational speed of 1200 rpm, and flow rate of 35 m³/h. It is observed that the change of the total efficiency with the NPSHa is similar to the change of the total head with the NPSHa, as shown in



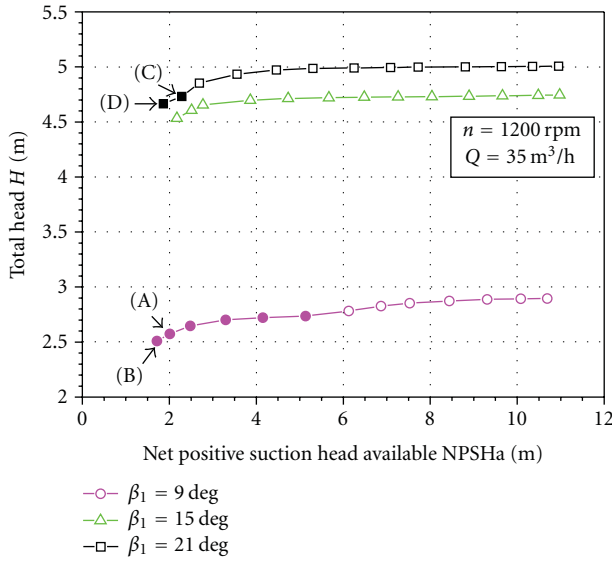


FIGURE 9: Total head drop curves, where cavitation has been developed to the filled points.

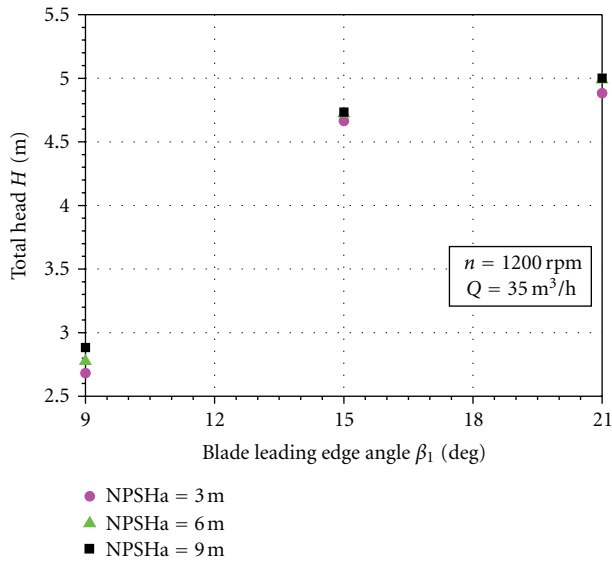


FIGURE 10: The change of the total head with the blade leading edge angle for three different values of the net positive suction head available.

Figure 9. As the blade leading edge angle increases the total efficiency increases as well. In addition, for the lowest values of the  $NPSHa$ , much faster decrease of the total efficiency is observed, for all the tested blade leading edge angles. Examining the blade leading edge angles 15 and 21 deg, fluctuations are observed to the total efficiency, because of the unstable measurements of both the voltage and the amperage.

The uncertainty on the measurements has been evaluated from the resolution of the data acquisition system, realizing multiple experiments with deviation from the presented data, approximately  $\pm 0.10\%$ . The relative uncertainty for the total head is  $0.07\%$  for all the examined blade leading

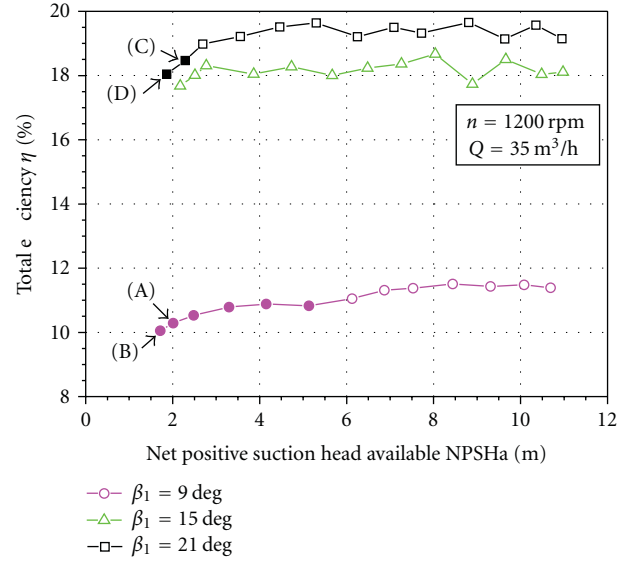


FIGURE 11: The change of the total efficiency with the net positive suction head available for rotational speed of 1200 rpm and flow rate of  $35 \text{ m}^3/\text{h}$ .

edge angles. For the net positive suction head available, the relative uncertainty varies from  $0.08\%$  to  $0.10\%$  for 9 deg and 21 deg and  $0.08\%$  to  $0.09\%$  for 15 deg. Finally, for the total efficiency, the relative uncertainty varies from  $0.54\%$  to  $0.55\%$  for 9 deg and is  $0.53\%$  for 15 deg and 21 deg.

Furthermore, in the present experimental study the vapour distribution between the blades at the leading edge is illustrated using the stroboscopic light. The vapour is caused by the strong curvature of the streamlines along the front shroud, where low values of the net positive suction head prevail. Two of the cavitation cases of 9 deg are depicted in Figures 12 and 13, where a scaling bar is added to each figure, representing a length of 10 mm and a letter is added in parentheses corresponding to the letter in Figures 9 and 11. Thus Figure 12 corresponds to the point A and Figure 13 corresponds to the point B. Testing the blade leading edge angle of 9 deg, the cavitation is observed at the leading edge in the region of the pressure side. Moreover, it is noticed that as the net positive suction head decreases, lower pressures between the blades prevail and the cavity length increases. As the cavity length increases the total head and total efficiency decrease, as shown in Figures 9 and 11, due to flow blockage from cavitation vapour in the blades.

In Figures 14 and 15 the cavitation is developed at the leading edge in the region of the suction side for the blade leading edge angle of 21 deg. Figure 14 corresponds to the point C and Figure 15 corresponds to the point D. The region where the cavitation is developed is different from the corresponding of 9 deg. As the blade leading edge angle decreases, the passage between the blades decreases, lower pressures prevail in this region and the cavitation is developed at the pressure side. On the other hand, for blade leading edge angle of 21 deg, the lowest pressures prevail at the suction side of the blades and cavitation is developed in this region. Examining the blade leading edge angle of

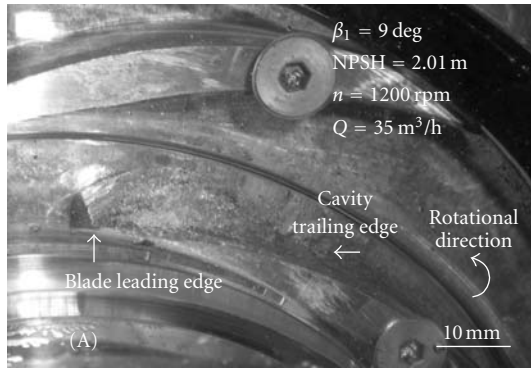


FIGURE 12: Illustration of cavitation for the blade leading edge angle of 9 deg and NPSH equal to 2.01 m.

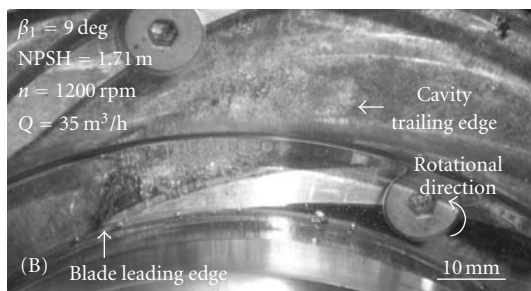


FIGURE 13: Illustration of cavitation for the blade leading edge angle of 9 deg and NPSH equal to 1.71 m.

15 deg, no cavitation is observed, because the testing flow rate of  $35 \text{ m}^3/\text{h}$  is almost equal to the corresponding of the best efficiency point for 15 deg. For 9 deg, the testing flow rate of  $35 \text{ m}^3/\text{h}$  is greater than its corresponding best efficiency point, thus the cavitation is developed at the pressure side of the blades. On the other hand, for 21 deg, the testing flow rate  $35 \text{ m}^3/\text{h}$  is less than its corresponding best efficiency point and the cavitation is developed at the suction side of the blades. Moreover, the cavity length for 21 deg is smaller than the corresponding of 9 deg, because lower net positive suction head values prevail for blade leading edge angle of 9 deg, as shown in Figures 9 and 11.

## 5. Conclusions

The present experimental study and passive flow control are concerned with the effect of the blade leading edge angle on the cavitation and performance of a centrifugal pump. A pump test rig has been developed in order to realize a passive flow control with different blade leading edge angles, allowing optical observation of the cavitation development with the aid of a stroboscopic light source.

The rotational speed of 1200 rpm and flow rate of  $35 \text{ m}^3/\text{h}$  are applied. Studying the effect of the blade leading edge angle on the cavitation, it is observed that as the blade leading edge angle increases, both the total head and the total efficiency increase for the examined operating conditions. Moreover, it is noticed that as the net positive suction head decreases the total head decreases slowly for all the examined blade leading edge angles.

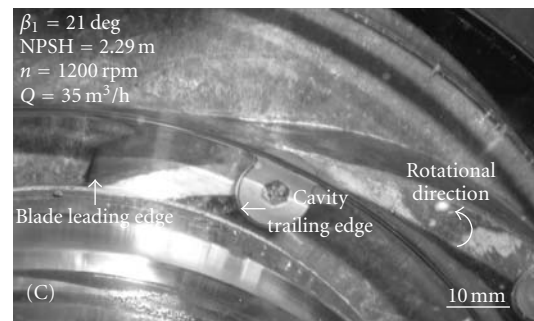


FIGURE 14: Illustration of cavitation for the blade leading edge angle of 21 deg and NPSH equal to 2.29 m.



FIGURE 15: Illustration of cavitation for the blade leading edge angle of 21 deg and NPSH equal to 1.86 m.

Examining the blade leading edge angle of 9 deg, the cavitation is developed at the leading edge in the region of the pressure side. On the other hand, for 21 deg, the cavitation is developed at the leading edge in the region of the suction side. Finally, for the blade leading edge angle of 15 deg, there is no cavitation development and the danger of the pump damage and erosion is eliminated. Thus, the costs of maintenance of the centrifugal pumps are limited, applying the blade leading edge angle of 15 deg.

Further research work is planned to be accomplished experimentally and computationally, studying the effect of different blade design methods on the cavitation of a centrifugal pump and applying passive flow control with different impeller geometrical characteristics and operating conditions.

## References

- [1] R. Hirschi, P. Dupont, F. Avellan, J. N. Favre, J. F. Guelich, and E. Parkinson, "Centrifugal pump performance drop due to leading edge cavitation: numerical predictions compared with model tests," *Journal of Fluids Engineering*, vol. 120, no. 4, pp. 705–711, 1998.
- [2] M. Hofmann, B. Stoffel, J. Friedrichs, and G. Kosyna, "Similarities and geometrical effects on rotating cavitation in two scaled centrifugal pumps," in *Proceedings of the 4th International Symposium on Cavitation (CAV '01)*, pp. 20–23, California Institute of Technology, Pasadena, Calif, USA, June 2001.

- [3] M. Frobenius, R. Schilling, J. Friedrichs, and G. Kosyna, "Numerical and experimental investigations of the cavitating flow in a centrifugal pump impeller," in *Proceedings of the ASME Joint U.S.-European Fluids Engineering Conference (FEDSM '02)*, pp. 361–368, Montreal, Canada, July 2002.
- [4] O. Coutier-Delgosha, R. Fortes-Patella, J. L. Reboud, M. Hofmann, and B. Stoffel, "Experimental and numerical studies in a centrifugal pump with two-dimensional curved blades in cavitating condition," *Journal of Fluids Engineering*, vol. 125, no. 6, pp. 970–978, 2003.
- [5] V. Siljegovic, N. Milicevic, and P. Griss, "Passive, programmable flow control in capillary force driven microfluidic networks," in *Proceedings of the 13th International Conference on Solid-State Sensors and Actuators and Microsystems (TRANSDUCERS '05)*, pp. 1565–1568, Seoul, Korea, June 2005.
- [6] A. Ulas, "Passive flow control in liquid-propellant rocket engines with cavitating venturi," *Flow Measurement and Instrumentation*, vol. 17, no. 2, pp. 93–97, 2006.
- [7] X. Escaler, E. Egusquiza, M. Farhat, F. Avellan, and M. Coussirat, "Detection of cavitation in hydraulic turbines," *Mechanical Systems and Signal Processing*, vol. 20, no. 4, pp. 983–1007, 2006.
- [8] D. Japikse, K. N. Oliphant, and D. O. Baun, "Stability Enhancement of Compressors and Turbopumps by Passive Flow Control," Thermal and Fluids Analysis Works (TFAWS), College Park, MD, USA, 7–11 August 2006.
- [9] X. Luo, Y. Zhang, J. Peng, H. Xu, and W. Yu, "Impeller inlet geometry effect on performance improvement for centrifugal pumps," *Journal of Mechanical Science and Technology*, vol. 22, no. 10, pp. 1971–1976, 2008.
- [10] D. Wu, L. Wang, Z. Hao, Z. Li, and Z. Bao, "Experimental study on hydrodynamic performance of a cavitating centrifugal pump during transient operation," *Journal of Mechanical Science and Technology*, vol. 24, no. 2, pp. 575–582, 2010.
- [11] S. D. Kyparissis and D. P. Margaris, "Experimental study in a centrifugal pump with double-arc synthetic blade design method in cavitating and non-cavitating conditions," in *Proceedings of the 4th International Conference on Experiments / Process / System Modeling / Simulation / Optimization, (IC-EpsMsO '11)*, Athens, Greece, July 2011.
- [12] S. D. Kyparissis and D. P. Margaris, "Experimental investigation of cavitation in a centrifugal pump with double-arc synthetic blade design method," *International Review of Mechanical Engineering*, vol. 5, no. 5, pp. 884–892, 2011.
- [13] S. D. Kyparissis and D. P. Margaris, "Experimental and computational study on the effects of the cavitation to the total head of a centrifugal pump," in *Proceedings of the 5th International Conference from Scientific Computing to Computational Engineering (IC-SCCE '12)*, Athens, Greece, July 2012.
- [14] S. D. Kyparissis, E. C. Douvi, E. E. Panagiotopoulos, D. P. Margaris, and A. E. Filios, "CFD flowfield analysis and hydrodynamic double-arc blade design effects for optimum centrifugal pump performance," *International Review of Mechanical Engineering*, vol. 3, no. 3, pp. 284–292, 2009.
- [15] S. D. Kyparissis, E. C. Douvi, E. E. Panagiotopoulos, D. P. Margaris, and A. E. Filios, "Parametric study performance of a centrifugal pump based on simple and double-arc blade design methods," in *Proceedings of the 3rd International Conference on Experiments / Process / System Modeling / Simulation / Optimization (IC-EpsMsO '09)*, pp. 8–11, Athens, Greece, July 2009.
- [16] S. D. Kyparissis, D. P. Margaris, E. E. Panagiotopoulos, and A. E. Filios, "CFD analysis on the effects of the blade design method to the centrifugal pump performance," *International Review of Mechanical Engineering*, vol. 3, no. 5, pp. 553–561, 2009.
- [17] C. Pfleiderer, *Die Kreiselpumpen Für Flüssigkeiten Und Gase*, Springer, Berlin, Germany, 1961.
- [18] P. Girdhar and O. Moniz, *Practical Centrifugal Pumps: Design, Operation and Maintenance*, Elsevier, Oxford, UK, 2005.

## Research Article

# Effects of Input Voltage on Flow Separation Control for Low-Pressure Turbine at Low Reynolds Number by Plasma Actuators

**Takayuki Matsunuma and Takehiko Segawa**

*Turbomachinery Group, Energy Technology Research Institute, National Institute of Advanced Industrial Science and Technology (AIST), 1-2-1 Namiki, Ibaraki, Tsukuba 3058564, Japan*

Correspondence should be addressed to Takayuki Matsunuma, t-matsunuma@aist.go.jp

Received 23 July 2012; Revised 2 November 2012; Accepted 7 November 2012

Academic Editor: N. Sitaram

Copyright © 2012 T. Matsunuma and T. Segawa. This is an open access article distributed under the Creative Commons Attribution License, which permits unrestricted use, distribution, and reproduction in any medium, provided the original work is properly cited.

Active flow control using dielectric barrier discharge (DBD) plasma actuators was investigated to reattach the simulated boundary layer separation on the suction surface of a turbine blade at low Reynolds number,  $Re = 1.7 \times 10^4$ . The flow separation is induced on a curved plate installed in the test section of a low-speed wind tunnel. Particle image velocimetry (PIV) was used to obtain instantaneous and time-averaged two-dimensional velocity measurements. The amplitude of input voltage for the plasma actuator was varied from  $\pm 2.0$  kV to  $\pm 2.8$  kV. The separated flow reattached on the curved wall when the input voltage was  $\pm 2.4$  kV and above. The displacement thickness of the boundary layer near the trailing edge decreased by 20% at  $\pm 2.0$  kV. The displacement thickness was suddenly reduced as much as 56% at  $\pm 2.2$  kV, and it was reduced gradually from  $\pm 2.4$  kV to  $\pm 2.8$  kV (77% reduction). The total pressure loss coefficient, estimated from the boundary layer displacement thickness and momentum thickness, was 0.172 at the baseline (actuator off) condition. The total pressure loss was reduced to 0.107 (38% reduction) at  $\pm 2.2$  kV and 0.078 (55% reduction) at  $\pm 2.8$  kV.

## 1. Introduction

Blade Reynolds numbers for the low-pressure turbine of small- and medium-sized gas turbines for aircraft propulsion can drop to below  $2.5 \times 10^4$  at high altitudes, where the air density is low [1]. At these low Reynolds numbers, the boundary layer is dominated by laminar flow and is susceptible to flow separation and strong secondary vortices that develop into increased losses, leading to reduced performance.

Newly developed high-efficiency small-scale gas turbines for industrial power generation also encounter the low Reynolds number problem because of the increased viscosity caused by high turbine inlet temperatures and miniaturization of the cascade [2]. Several studies focusing on the aerodynamics of turbine cascades at low Reynolds numbers have been published [3–7].

Different passive and active flow control techniques have been developed to increase the efficiency of the turbine blade at low Reynolds numbers [8]. Passive control devices, such as dimples and fixed turbulators, are traditional approaches to trigger transition and induce reattachment, but create undesirable drag at high Reynolds number. Active control devices can be employed only when needed. Vortex generating jets (VGJs) and plasma actuators are prominent subjects of recent research in active flow control.

The application of dielectric barrier discharge (DBD) plasma actuator was demonstrated by Roth et al. [9] in 1998 and has been developed over the last decade from fundamental studies to a wide range of applications [10].

Figure 1 shows a simple schematic configuration of a DBD plasma actuator. The DBD plasma actuator consists of a dielectric layer sandwiched between top and bottom electrodes. Applying high voltages at high frequencies



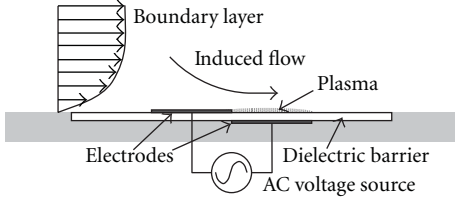


FIGURE 1: Schematics of plasma actuator.

(approximately 1 kHz~50 kHz) between the top and bottom electrodes forms a layer of glow discharge plasma across the dielectric surface. This induces a tangential air jet with a strong horizontal velocity component. It is known that the direction of the resultant tangential jet is constant and independent of which electrode the voltage is applied to, and independent of the polarity of the applied voltage [11].

DBD plasma actuators have also been used in a number of low-pressure turbine separation control studies [12–18]. In order to distinguish this work from these prior studies, this paper focused on the presentation of detailed PIV flow data and accompanying analysis at various input voltage of the plasma actuator.

The objective of this study is to investigate the most effective active flow control operation of DBD plasma actuators by simplified experiments. The experimental results in this study will be used as the fundamental data for considering the application of DBD plasma actuators for the annular turbine wind tunnel with a single-stage axial-flow turbine [19, 20]. This paper presents the results of particle image velocimetry (PIV) measurement to understand the flow mechanisms and the effect of different amplitude of the plasma actuator input voltage.

## 2. Experimental Facility and Method

Figure 2 shows the measurement system. The wind tunnel is a low-speed, open-circuit, blower-type facility with 305 mm × 85 mm × 65 mm test section.

A curved wall plate (streamwise length  $L = 100$  mm) was installed in the test section of the wind tunnel in order to simulate the separated flow on the suction surface of a turbine blade. Figure 3 shows the geometry and the design-surface velocity distribution, derived from an inviscid calculation, at the midspan of the corresponding turbine rotor blade in the annular turbine wind tunnel in AIST [19, 20]. Table 1 shows the nondimensional parameters of the corresponding turbine rotor midspan. The shape of the curved wall was designed using a simple one-dimensional continuity argument to match the design surface velocity and pressure distributions of the corresponding turbine blade. A plasma actuator was mounted at the front of the adverse pressure gradient region (deceleration region) on the curved wall.

Particle image velocimetry (PIV) was employed to quantify the behavior of the flow field around the curved wall. The laser was a 25 mJ/pulse, double-pulse Nd-YAG laser (MiniLase II, 20 Hz, New Wave Research Co. Ltd.). Atomized

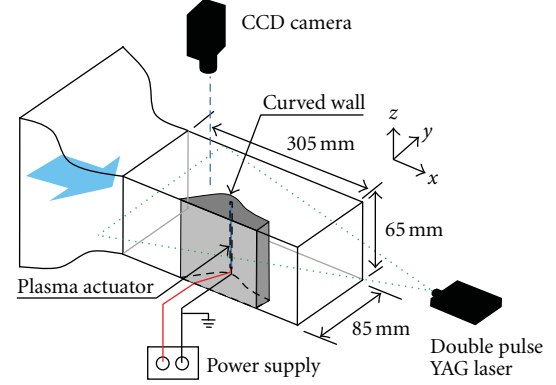


FIGURE 2: Measurement system.

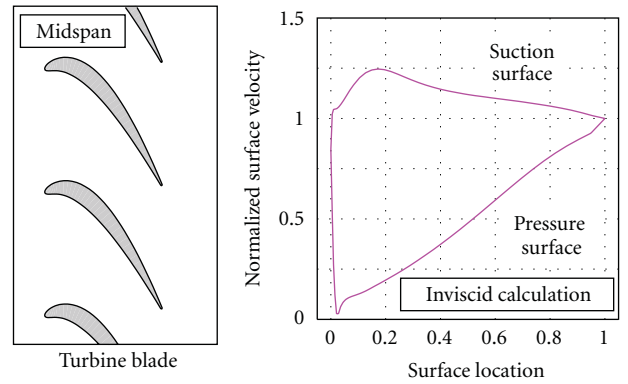


FIGURE 3: Corresponding turbine rotor.

TABLE 1: Nondimensional parameters of corresponding turbine rotor (midspan).

Inlet blade angle	$\beta_1$	21.8 deg
Exit blade angle	$\beta_2$	63.4 deg
Blade turning angle	$\beta_1 + \beta_2$	85.2 deg
Stagger angle	$\xi$	47.6 deg
Diffusion factor	$D$	0.198
Solidity (chord/pitch)	$C/S$	1.42
Trailing edge thickness/passag width	$t/w$	0.032

Diocetyl sebacate (DOS) oil with a mean particle diameter of  $1 \mu\text{m}$  was injected upstream of the test section via a pressurized oil chamber. Image pairs were taken by a camera (PIV CAM 13-8, TSI Inc.), which has  $1,280 \times 1,024$  pixel resolution. TSI software calculated the velocity vectors from the peak correlation of groups of particles between frames, using conventional cross-correlation algorithms on a  $32 \times 32$  pixel grid. In order to calculate the averaged velocity distributions, 50 instantaneous velocity distributions were measured at each experimental condition in this study. It should be noted that the PIV data in the vicinity of the plasma actuator possesses lower reliability than that in the main flow, due to the laser reflections from the top electrode of the plasma actuator, the large velocity gradients across

the induced jet, and the possibility that the seeding particles are influenced by the electric field [21, 22].

Figure 4 shows the test section geometry and PIV measurement grids. In these experiments, the rotating speed of the wind tunnel blower was kept constant. The streamwise velocity of the main flow near the trailing edge ( $x = 100$  mm) was almost constant,  $U_{x,\text{main flow}} \approx 2.25$  m/s, for each input voltage condition, as shown later in Figure 11. Therefore, the Reynolds number based on the streamwise length of the curved wall,  $L$ , and the streamwise velocity of the main flow near the trailing edge,  $U_x$ , was  $Re = 1.7 \times 10^4$ .

The edge of the top electrode of the plasma actuator, where the surface plasma is formed, was located at  $x = 30.6$  mm from the leading edge. A thin sheet of polyimide (125  $\mu\text{m}$  thickness, relative permittivity  $\epsilon' \approx 3$ ) was used as the dielectric barrier of the plasma actuator. As for the electrodes, thin sheets of copper (thickness = 35  $\mu\text{m}$ ) were glued and pressed onto the both sides of the dielectric. A high voltage, high-frequency power supply (PG1040F, PSI Inc.), which can output bipolar sinusoidal waveforms, was used to supply input signals to the top and bottom electrodes. The bottom electrode was connected to ground,  $V_g = 0$  V. The amplitude of input voltage to the top electrode  $V_{AC}$  was varied from 2.0 kV to 2.8 kV (4.0–5.6 kV<sub>p-p</sub>). The frequency of input voltage  $f_p$  was fixed at  $f_p = 8.1$  kHz.

### 3. Results and Discussion

**3.1. Instantaneous Absolute Velocity Distributions.** Figure 5 shows a sample of the PIV images, the instantaneous absolute velocity, and vorticity distributions for the baseline condition (plasma actuator off). Massive flow separation is visualized in the flow deceleration region in the PIV image of Figure 5(a). The large low-velocity region, drawn by blue contours in Figure 5(b), corresponds to the flow separation. (The criteria for separation or reattachment of the boundary layer are based on the boundary layer shape factor  $H_{12}$ , as shown in Figure 15 later). The separated boundary layer is stable from the streamwise location  $x = 20$  mm (starting position of the flow separation) to  $x = 70$  mm (namely 70% chord length position). The separated flow downstream of  $x = 70$  mm becomes unstable and large clockwise vortices are generated.

Figure 6 shows a sample of the PIV images, the instantaneous absolute velocity and vorticity distributions for the flow control condition (plasma actuator on, input voltage  $V_{AC} = \pm 2.8$  kV, maximum input voltage in this study). The separated flow region is dramatically reduced by flow control using the plasma actuator. The flow separation from  $x = 20$  mm became unstable after  $x = 40$  mm ~ 50 mm and small clockwise vortices were generated. The similar phenomenon of the smaller flow structure by the effect of the plasma actuator was observed in the flow visualization by Marks et al. [18]. The flow control using plasma actuator results in attached flow before the trailing edge.

**3.2. Time-Averaged Absolute Velocity Distributions.** Figure 7 shows enlarged views of the time-averaged absolute velocity

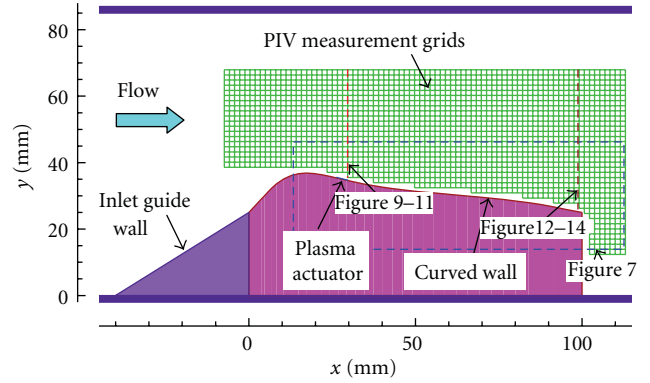


FIGURE 4: Test section and PIV grids.

distributions in the separation region (blue dashed frame in Figure 4) at various input voltages. These distributions were calculated by averaging 50 instantaneous velocity distributions as shown in Figures 5 and 6. In these figures, streamlines were superimposed upon the velocity contours.

The large separation region observed in the baseline (actuator off) condition in Figure 7(a) is gradually reduced by the effect of active control in Figures 7(b), 7(c), 7(d), 7(e), and 7(f).

In the baseline condition in Figure 7(a), large reverse flow is observed in the separation region. In the flow control case of  $V_{AC} = \pm 2.0$  kV in Figure 6(b), a large recirculation exists in the separation region, and the low-velocity region is slightly reduced near the trailing edge. In the flow control case of  $V_{AC} = \pm 2.2$  kV in Figure 6(c), the recirculation in the separation region become reduced in size and the position of its center moves upstream. The separated flow reattaches onto the surface of the curved wall before the trailing edge. In Figures 6(d), 6(e), and 6(f), at  $V_{AC} = \pm 2.4$  kV ~  $\pm 2.8$  kV, as the input voltage is increased, the recirculation in the separation region become smaller and moves more upstream. The reduction of the separation region was observed in the LDV measurements by Huang et al. [13], the PIV measurements by Boxx et al. [16], total pressure measurements by Burman et al. [17], and the surface pressure measurements by Marks et al. [18].

**3.3. Turbulence Intensity Distributions.** Figure 8 shows turbulence intensity distributions at various input voltages. In these figures, velocity vectors were superimposed upon the turbulence intensity contours. The turbulence intensity was calculated as follows:

$$Tu = \frac{\sqrt{(u_x'^2 + u_y'^2)/2}}{U_{x,\text{main flow}}} \quad (1)$$

The turbulence intensity was normalized by the averaged streamwise velocity of the main flow near the trailing edge at  $x = 99.1$  mm,  $U_{x,\text{main flow}} \approx 2.25$  m/s, as shown in Figure 11 later.

In the baseline condition in Figure 8(a), a high turbulence intensity region exists at the boundary line between

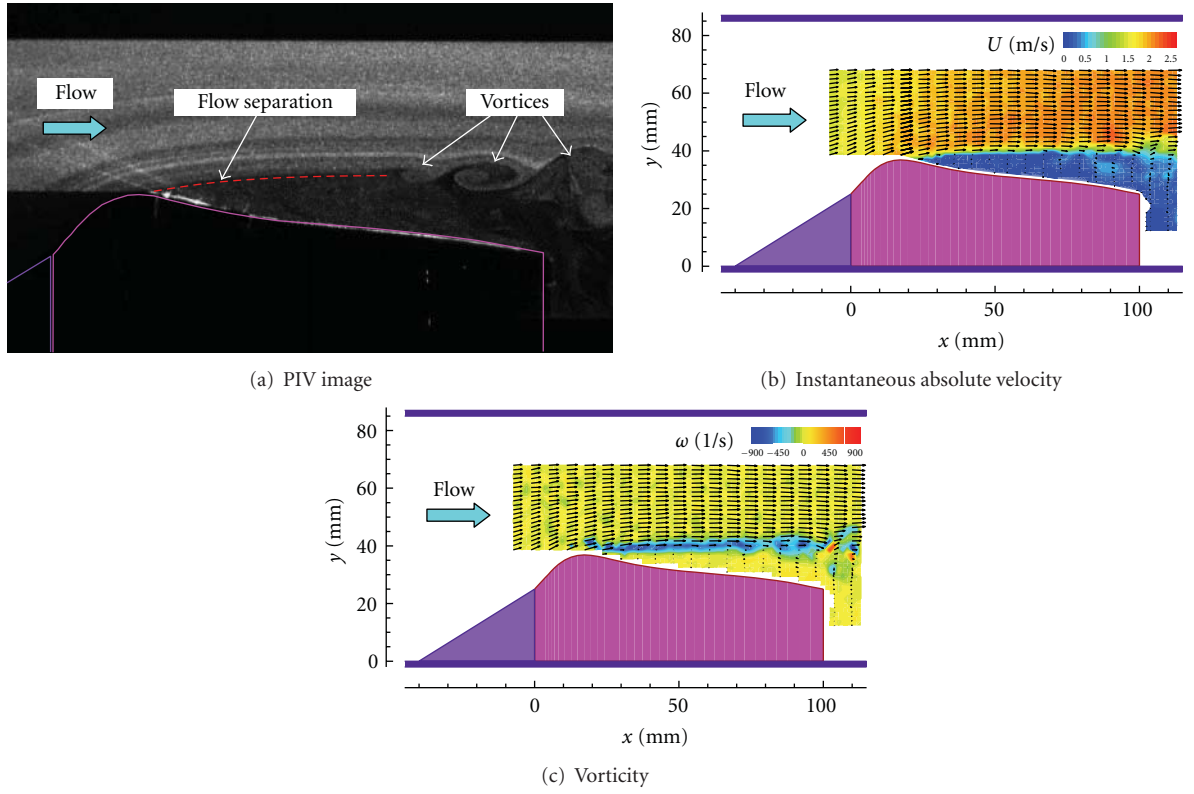
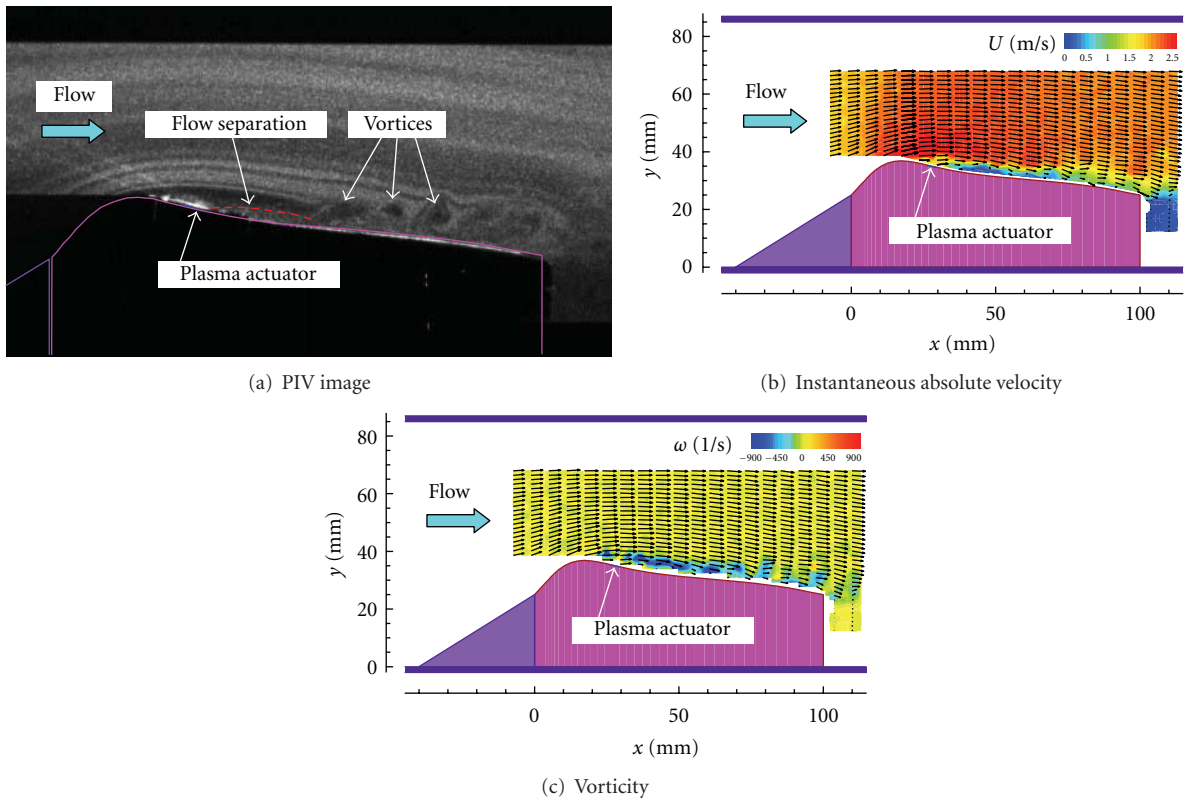


FIGURE 5: PIV measurements (baseline, plasma actuator off).

FIGURE 6: PIV measurements (flow control,  $V_{AC} = \pm 2.8$  kV).

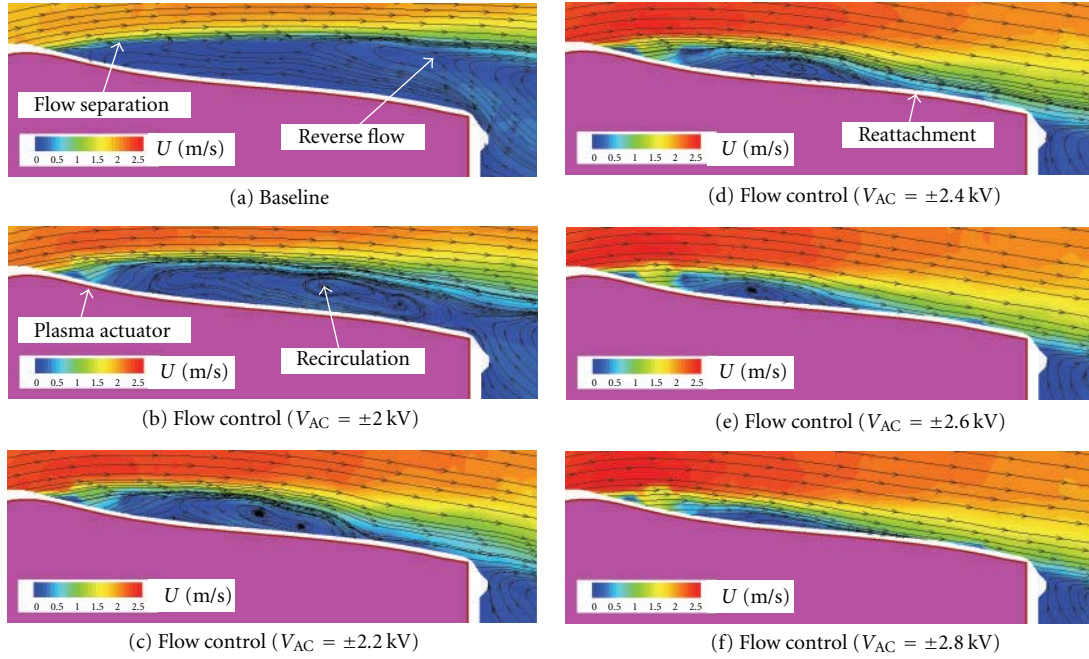


FIGURE 7: Time-averaged absolute velocity distributions and stream lines near curved wall at various DBD-PA input voltages.

the main flow and the separated flow. A wide high turbulence intensity region is suddenly generated after  $x = 70$  mm. This phenomenon corresponds to the fact that the separated boundary layer is stable from  $x = 20$  mm to  $x = 70$  mm and becomes unstable after  $x = 70$  mm, as shown in Figure 5. The wide high turbulence intensity region after  $x = 70$  mm is due to the unstable transitional separated boundary layer.

In the flow control case of  $V_{AC} = \pm 2.0$  kV in Figure 8(b), the high turbulence intensity region is generated after  $x = 50$  mm, which is further upstream than the baseline condition.

In the flow control case of  $V_{AC} = \pm 2.2$  kV in Figure 8(c), the high turbulence intensity region moves even further upstream and closer to the curved wall than that in  $V_{AC} = \pm 2.0$  kV condition, Figure 8(b).

In Figures 8(c), 8(d), 8(e), and 8(f), as the input voltage is increased, the high turbulence intensity region moves more upstream and closer to the curved wall and becomes smaller in width.

**3.4. Velocity Distributions Around Plasma Actuator.** Figure 9 shows the vertical distribution of the streamwise velocity  $U_x$  near the center of the plasma actuator,  $x = 29.7$  mm,  $x/L = 0.297$  (red dashed line in Figure 4). The vertical position  $y = 34.6$  mm corresponds to the surface of the curved wall. In the baseline condition (black line in the figure), the average streamwise velocity of the main flow is 2.05 m/s. The streamwise velocity in the boundary layer at  $y \leq 40$  mm is close to zero due to the flow separation near the curved wall. At  $V_{AC} = \pm 2.0$  kV (red line), the average streamwise velocity of the main flow increases to 2.26 m/s (10% increase from the baseline condition). The streamwise velocity in the boundary

layer increases to 0.73 m/s. At  $V_{AC} = \pm 2.2$  kV (pink), the average streamwise velocity of the main flow increases to 2.48 m/s (21% increase from the baseline) and that in the boundary layer increases to 0.89 m/s. At  $V_{AC} = \pm 2.4$  kV (orange), the average streamwise velocity of the main flow increases slightly to 2.51 m/s and that in the boundary layer increases to 1.27 m/s. At maximum input voltage of  $V_{AC} = \pm 2.8$  kV (blue), the average streamwise velocity of the main flow increases to 2.58 m/s (26% increase from the baseline) and that in the boundary layer increases to 1.66 m/s.

Figure 10 shows the vertical distribution of the vertical velocity  $U_y$  near the plasma actuator. The positive value means upward flow in the  $y$ -direction and the negative value means downward flow.

In the baseline condition (black line), the vertical velocity of the main flow at  $y = 42$  mm is 0.27 m/s. As the input voltage is increased, the vertical velocity of the main flow is gradually reduced by the effect of active flow control of the plasma actuator. At maximum voltage of  $V_{AC} = \pm 2.8$  kV (blue), the vertical velocity of the main flow at  $y = 40$  mm becomes  $-0.07$  m/s (0.34 m/s decrease from the baseline condition).

The vertical velocity of the boundary layer at  $y \leq 40$  mm is almost zero in the baseline condition. At  $V_{AC} = \pm 2.0$  kV (red line), the vertical velocity in the boundary layer increases to 0.3 m/s due to the induced flow by the plasma actuator. As the input voltage is increased, the vertical velocity in the boundary layer is gradually reduced.

Figure 11 shows the vertical distribution of the flow angle  $\theta$  near the plasma actuator. The positive value means upward flow and the negative value means downward flow. As the input voltage is increased, the flow angle in both the main flow and in the boundary layer is gradually reduced by



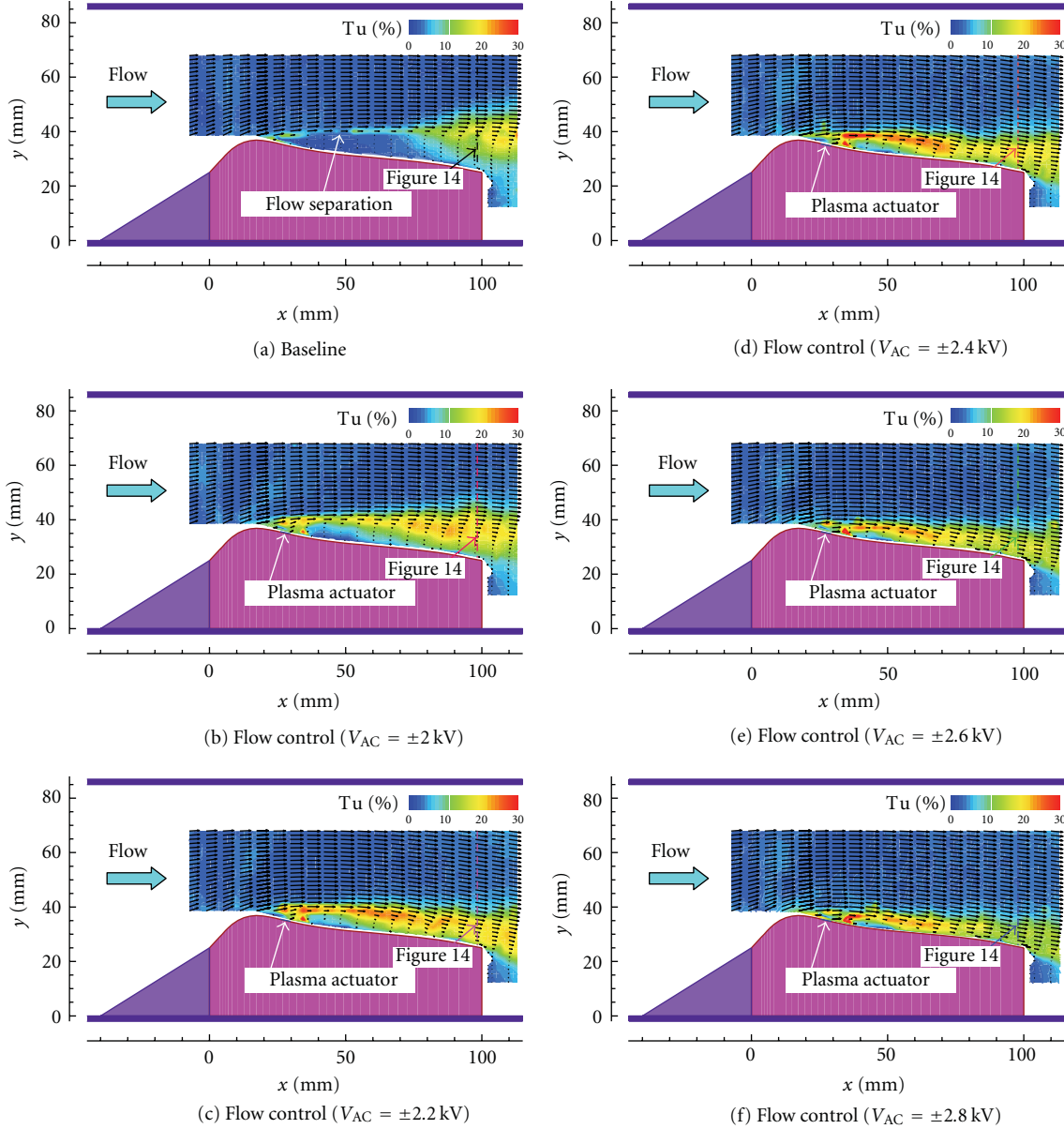


FIGURE 8: Turbulence intensity distributions at various DBD-PA input voltages.

the effect of active flow control of the plasma actuator (i.e., decrease in separation angle). At  $V_{AC} = \pm 2.8$  kV, the flow angle is reduced 9 deg in the main flow and 23 deg in the boundary layer, respectively.

**3.5. Velocity Distributions Near Trailing Edge.** Figure 12 shows the vertical distribution of the streamwise velocity near the trailing edge,  $x = 99.1$  mm,  $x/L = 0.991$  (brown dashed line in Figure 4). The bottom of the vertical axis (vertical position  $y = 25$  mm) corresponds to the surface of the curved wall at the trailing edge. The streamwise velocity of the main flow is almost constant ( $U_{x, \text{main flow}} \approx 2.25$  m/s) for all input voltage conditions. In the baseline condition (black line in the figure), large velocity deficit with reverse flow

exists near the surface of the curved wall. The boundary layer thickness (distance between the curved wall surface and the vertical position with 99% of the main flow velocity) is approximately 21 mm (from  $x = 25$  mm to  $x = 46$  mm). At  $V_{AC} = \pm 2.0$  kV (red line), the reverse flow is reduced but the boundary layer thickness is the same as the baseline. At  $V_{AC} = \pm 2.2$  kV (pink), the velocity in the boundary layer is suddenly increased. The reverse flow region completely disappears and the boundary layer thickness is reduced to 17 mm. At  $V_{AC} = \pm 2.4$  kV (orange), the shape of the velocity distributions in the boundary layer becomes quite linear. At  $V_{AC} = \pm 2.6$  kV and  $V_{AC} = \pm 2.8$  kV (green and blue), the velocity distributions in the boundary layer is further improved and the shape becomes convex.

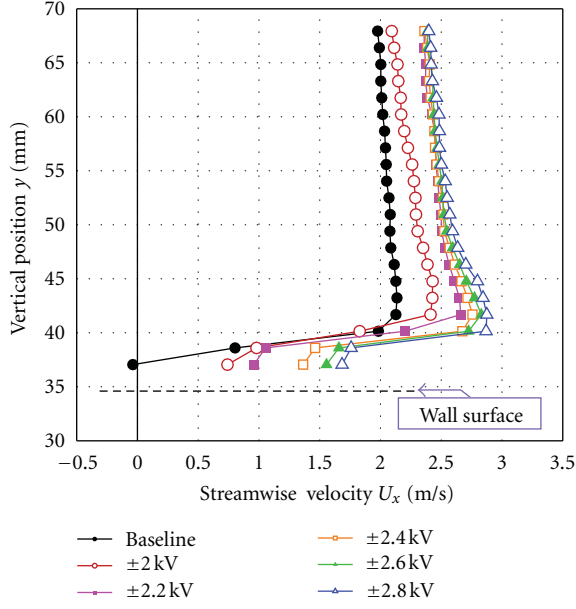


FIGURE 9: Streamwise velocity distributions near plasma actuator ( $x = 29.7$  mm).

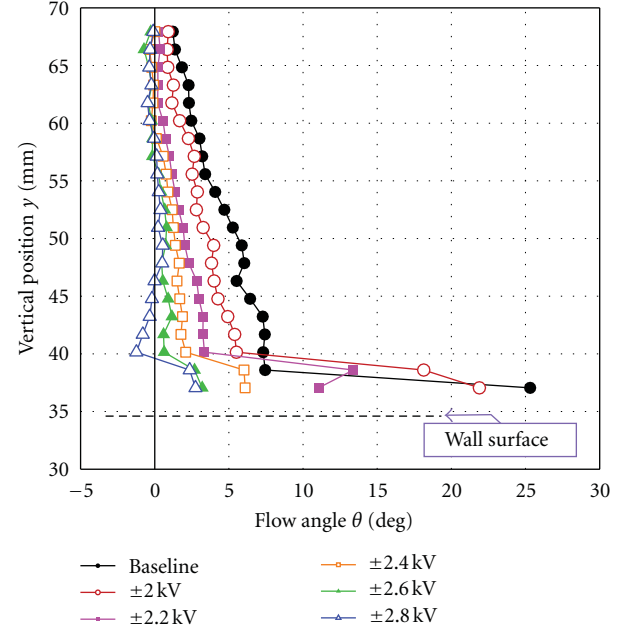


FIGURE 11: Flow angle distributions near plasma actuator ( $x = 29.7$  mm).

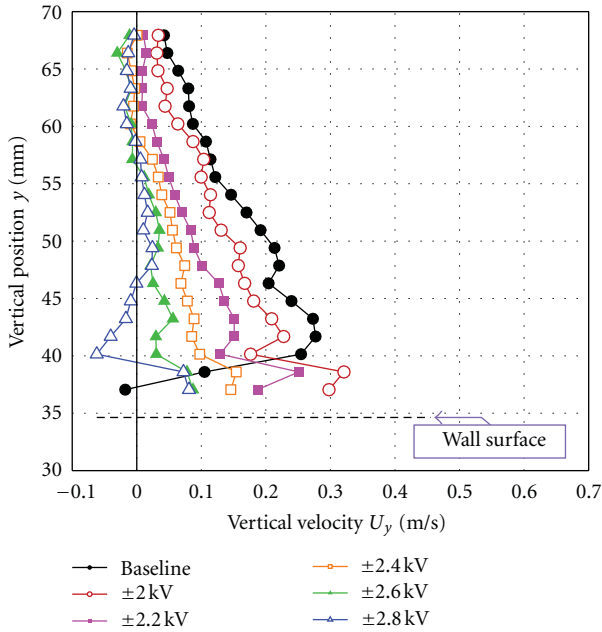


FIGURE 10: Vertical velocity distributions near plasma actuator ( $x = 29.7$  mm).

Figure 13 shows vertical distributions of the vertical velocity  $U_y$  near the trailing edge,  $x = 99.1$  mm. As the input voltage is increased, the vertical velocity in both the main flow and in the boundary layer is reduced (maximum 0.42 m/s reduction at  $V_{AC} = \pm 2.8$  kV).

Figure 14 shows vertical distributions of the turbulence intensity near the trailing edge,  $x = 99.1$  mm (dashed lines in Figure 8). Although the turbulence intensity of the main flow at the baseline is 2.1% for the baseline, that of the flow

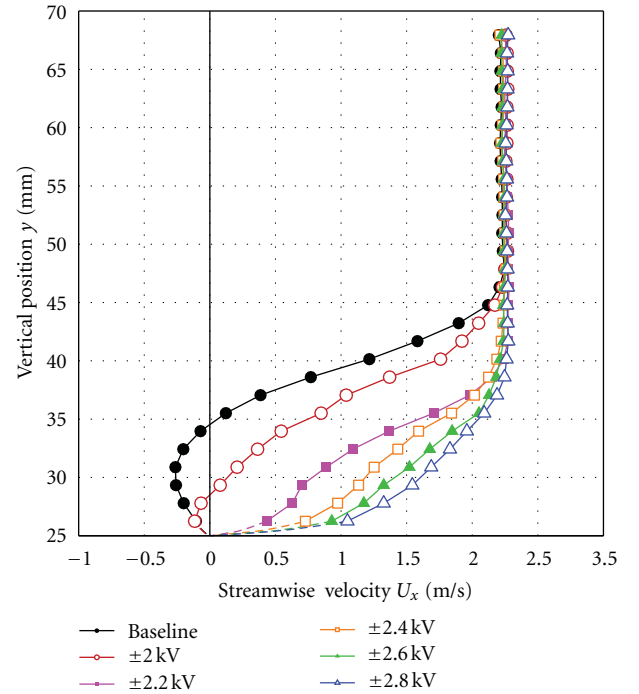


FIGURE 12: Streamwise velocity distributions near trailing edge ( $x = 99.1$  mm).

control conditions increase to 2.8% at  $V_{AC} = \pm 2.2$  kV and to 3.7% ~ 3.9% at  $V_{AC} = \pm 2.4$  kV ~ 2.8 kV. The slight increase in the turbulence intensity of the main flow is due to the flow fluctuation generated by the plasma actuator AC operation. In the baseline condition, the maximum turbulence intensity in the boundary layer is 17.5%. The maximum turbulence

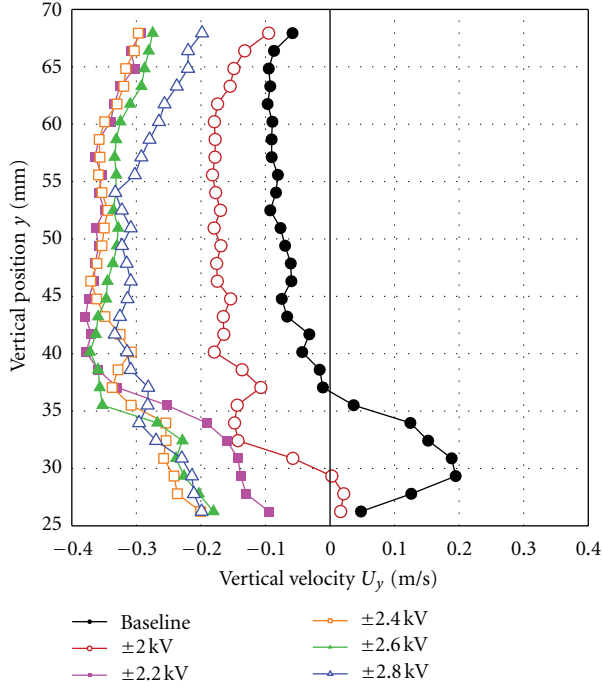


FIGURE 13: Vertical velocity distributions near trailing edge ( $x = 99.1$  mm).

intensity increases to 20% at  $V_{AC} = \pm 2.0$  kV  $\sim 2.4$  kV, and decreases to 16% and 14% at  $V_{AC} = \pm 2.6$  kV at  $V_{AC} = \pm 2.8$  kV, respectively. As the input voltage is increased, the vertical location of the maximum turbulence intensity moves closer to the wall, suggesting reattachment of the separated boundary layer. The similar phenomenon of the turbulence intensity change by the effect of the plasma actuator was observed in the PIV measurements by Boxx et al. [16].

**3.6. Boundary Layer Displacement Thickness and Momentum Thickness at Trailing Edge.** Figure 15 shows the displacement thickness,  $\delta_1$ , of the boundary layer near the trailing edge. The displacement thickness decreased by 20% at  $\pm 2.0$  kV. The displacement thickness is suddenly reduced as much as 56% at  $\pm 2.2$  kV, and it is reduced gradually from  $\pm 2.4$  kV to  $\pm 2.8$  kV (77% reduction).

Figure 16 shows the momentum thickness,  $\delta_2$ , of the boundary layer near the trailing edge. The momentum thickness is 2.45 mm at the baseline condition. The momentum thickness slightly increases to 2.61 mm (6.5% rise) at  $V_{AC} = \pm 2.4$  kV, where the shape of boundary layer velocity is a straight line, as shown in Figure 12. The momentum thickness then decreases to 1.95 mm (20.4% reduction) at  $V_{AC} = \pm 2.8$  kV.

**3.7. Boundary Layer Shape Factor at Trailing Edge.** Figure 17 shows the boundary layer shape factor  $H_{12}(=\delta_1/\delta_2)$  near the trailing edge. The shape factor  $H_{12}$  is 6.40 at the baseline condition and reduces as the amplitude of input voltage increases.

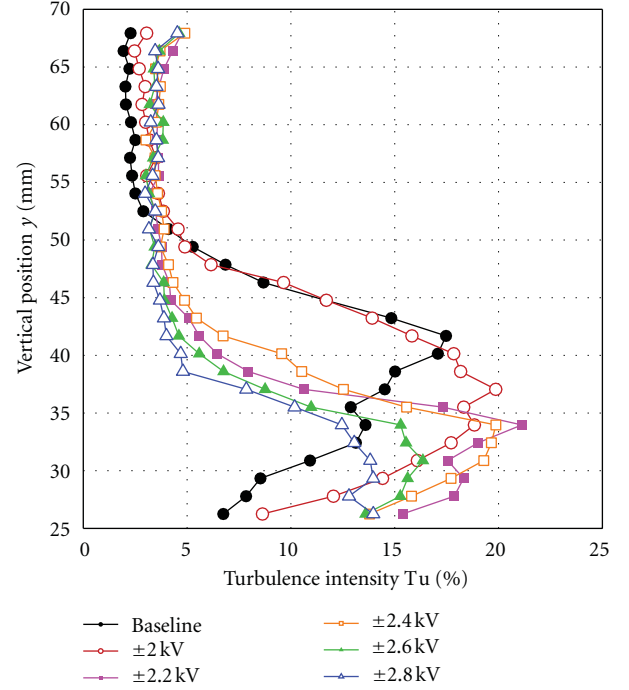


FIGURE 14: Turbulence intensity distributions near trailing edge ( $x = 99.1$  mm).

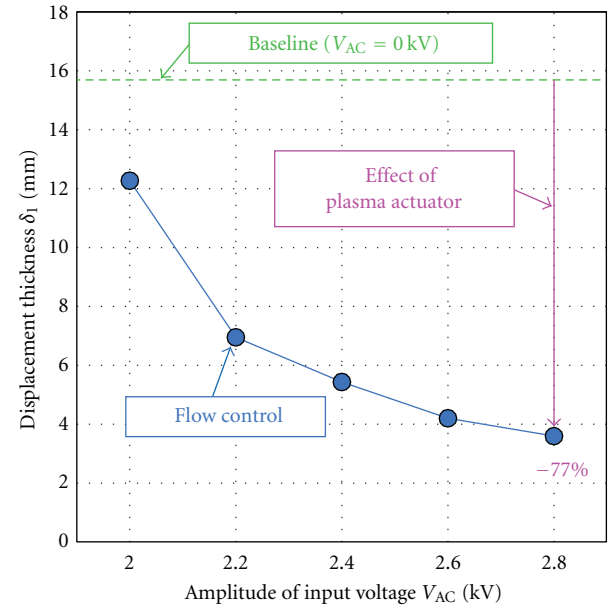


FIGURE 15: Displacement thickness of boundary layer near trailing edge ( $x = 99.1$  mm).

An empirical single-variable correlation using  $H_{12}$  was developed for incipient and full detachment and for reattachment of turbulent boundary layers on two-dimensional surfaces [23]. The  $H_{12}$  criteria of the correlation are  $H_{12} \geq 4.0$  for separated region (full detachment),  $2.2 \leq H_{12} \leq 4.0$  for intermittent detachment, and  $H_{12} \leq 2.2$  for attached boundary layer (reattachment).

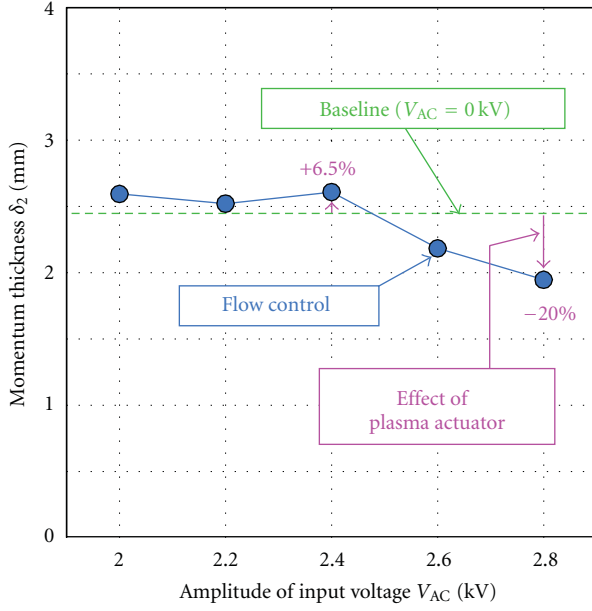


FIGURE 16: Momentum thickness of boundary layer near trailing edge ( $x = 99.1$  mm).

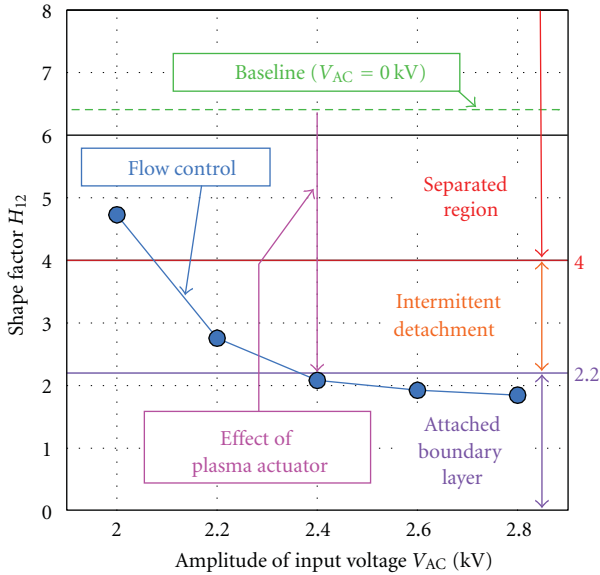


FIGURE 17: Shape factor  $H_{12}$  near trailing edge ( $x = 99.1$  mm).

From the correlation, the boundary layer at baseline and  $V_{AC} = \pm 2.0$  kV is separated, that at  $V_{AC} = \pm 2.2$  is intermittently detached, and that at  $V_{AC} = \pm 2.4$ ,  $\pm 2.6$  and  $\pm 2.8$  kV is reattached.

**3.8. Total Pressure Loss Estimation.** Figure 18 shows total pressure loss estimation. The total pressure loss coefficient,  $C_{Pt}$ , was estimated from the boundary layer displacement thickness,  $\delta_1$ , and momentum thickness,  $\delta_2$ , using the following correlation [24]:

$$C_{Pt} = \left( \frac{\delta_1 + t}{w} \right)^2 + \frac{2\delta_2}{w} - \frac{C_{pb}}{w}, \quad (2)$$

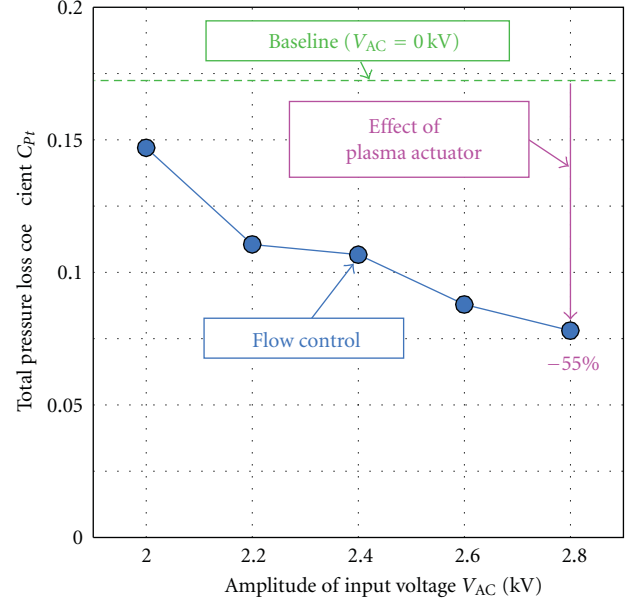


FIGURE 18: Total pressure loss estimation.

where  $w$  is passage width (60 mm),  $t$  is trailing edge thickness (1.9 mm), and  $C_{pb}$  is base pressure coefficient. Because the  $C_{pb}$  value is unknown in this study, the typical value of  $C_{pb} = -0.15$  is used for this estimation. The third term including  $C_{pb}$  is about 3~6% of  $C_{Pt}$ ; therefore, the effect of unknown  $C_{pb}$  value is considered to be relatively smaller than the first and second terms.

The total pressure loss coefficient is 0.172 at the baseline condition. The total pressure loss is reduced to 0.107 (38% reduction) at  $\pm 2.2$  kV, and 0.078 (55% reduction) at  $\pm 2.8$  kV.

## 4. Conclusions

Active flow control using dielectric barrier discharge plasma actuators was investigated to reattach the simulated separation flow over the suction surface of a turbine blade at low Reynolds number,  $Re = 1.7 \times 10^4$ . The flow separation was induced on a curved plate installed in the test section of a low-speed wind tunnel. Particle image velocimetry (PIV) was used to obtain instantaneous and time-averaged two-dimensional velocity measurements. The amplitude of input voltage for the plasma actuator was varied from  $\pm 2.0$  kV to  $\pm 2.8$  kV. Due to the flow control using the plasma actuator, the separated flow was successfully reduced. The decrease in displacement thickness of the boundary layer near the trailing edge was 20% at  $\pm 2.0$  kV. The displacement thickness was suddenly reduced by as much as 56% at  $\pm 2.2$  kV and it was reduced gradually from  $\pm 2.4$  kV to  $\pm 2.8$  kV (77% reduction). The total pressure loss coefficient, estimated from the boundary layer displacement thickness and momentum thickness, was 0.172 at the baseline condition. The total pressure loss coefficient was reduced to 0.107 (38% reduction) at  $\pm 2.2$  kV, and 0.078 (55% reduction) at  $\pm 2.8$  kV.



## Nomenclature

$C_{pb}$ :	Base pressure coefficient, $-0.15$ (typical value)
$C_{Pt}$ :	Total pressure loss coefficient $C_{Pt} = (P_{t_{in}} - P_{t_{out}})/((1/2)\rho U_{out}^2)$
$D$ :	Diffusion factor $D = 1 - (U_{out}/U_{max})$
$f_p$ :	Frequency of input voltage
$H_{12}$ :	Shape factor $(=\delta_1/\delta_2)$
$L$ :	Streamwise length of curved wall, 100 mm
$P_{t_{in}}$ :	Total pressure at inlet
$P_{t_{out}}$ :	Mass-averaged total pressure at outlet
$Re$ :	Reynolds number
$Tu$ :	Turbulence intensity
$t$ :	Trailing edge thickness, 1.9 mm
$U$ :	Absolute velocity
$U_{out}$ :	Mass-averaged absolute velocity at outlet
$U_{max}$ :	Maximum absolute velocity
$U_x$ :	Streamwise velocity
$U_{x,main flow}$ :	Averaged streamwise velocity of main flow near trailing edge
$u'_x$ :	Random fluctuation (turbulence) component of streamwise velocity
$U_y$ :	Vertical velocity
$u'_y$ :	Random fluctuation (turbulence) component of vertical velocity
$V_{AC}$ :	Amplitude of input voltage
$w$ :	Flow passage width at trailing edge, 60 mm
$x$ :	Streamwise (horizontal) distance
$y$ :	Vertical distance
$\delta_1$ :	Boundary layer displacement thickness
$\delta_2$ :	Boundary layer momentum thickness
$\theta$ :	Flow angle
$\rho$ :	Density.

## Acknowledgments

This study was supported by Grant-in-Aid for Young Scientists (B) of KAKENHI (no. 20760124) from The Ministry of Education, Culture, Sports, Science and Technology (MEXT), Japan. The authors would like to sincerely thank Dr. Timothy Jukes of the University of Nottingham for his helpful advice.

## References

- [1] R. Sondergaard, R. B. Rivir, and J. P. Bons, "Control of low-pressure turbine separation using vortex-generator jets," *Journal of Propulsion and Power*, vol. 18, no. 4, pp. 889–895, 2002.
- [2] H. Arakawa, T. Suzuki, K. Saito, S. Tamura, and S. Kishi, "Research and development of 300 kW class ceramic gas turbine project in Japan," ASME Paper 97-GT-87, 1997.
- [3] C. G. Murawski, R. Sondergaard, R. B. Rivir, K. Vafai, T. W. Simon, and R. J. Volino, "Experimental study of the unsteady aerodynamics in a linear cascade with low Reynolds number low pressure turbine blades," ASME Paper 97-GT-95, 1997.
- [4] W. Lou and J. Hourmouziadis, "Separation bubbles under steady and periodic-unsteady main flow conditions," *ASME Journal of Turbomachinery*, vol. 122, no. 4, pp. 634–643, 2000.
- [5] R. J. Howell, O. N. Ramesh, H. P. Hodson, N. W. Harvey, and V. Schulte, "High lift and aft-loaded profiles for low-pressure turbines," *ASME Journal of Turbomachinery*, vol. 123, no. 2, pp. 181–188, 2001.
- [6] R. J. Volino and L. S. Hultgren, "Measurements in separated and transitional boundary layers under low-pressure turbine airfoil conditions," *ASME Journal of Turbomachinery*, vol. 123, no. 2, pp. 189–197, 2001.
- [7] K. W. Van Treuren, T. Simon, M. von Koller, A. R. Byerley, J. W. Baughn, and R. Rivir, "Measurements in a turbine cascade flow under ultra low Reynolds number conditions," *ASME Journal of Turbomachinery*, vol. 124, no. 1, pp. 100–106, 2002.
- [8] R. B. Rivir, R. Sondergaard, and J. P. Bons, "Control of separation in turbine boundary layers," AIAA Paper 2004-2201, 2004.
- [9] J. R. Roth, D. M. Sherman, and S. P. Wilkinson, "Boundary layer flow control with a one atmosphere uniform flow discharge," AIAA Paper 98-0328, 1998.
- [10] T. C. Corke, C. L. Enloe, and S. P. Wilkinson, "Dielectric barrier discharge plasma actuators for flow control," *Annual Review of Fluid Mechanics*, vol. 42, pp. 505–529, 2010.
- [11] Y. B. Suzen and P. G. Huang, "Simulations of flow separation control using plasma actuators," AIAA Paper 2006-877, 2006.
- [12] J. Huang, T. C. Corke, and F. O. Thomas, "Plasma actuators for separation control of low-pressure turbine blades," AIAA Paper 2003-1027, 2003.
- [13] J. Huang, T. C. Corke, and F. O. Thomas, "Unsteady plasma actuators for separation control of low-pressure turbine blades," *AIAA Journal*, vol. 44, no. 7, pp. 1477–1487, 2006.
- [14] D. P. Rizzetta and M. R. Visbal, "Numerical investigation of plasma-based flow control for a transitional highly-loaded low-pressure turbine," AIAA Paper 2007-938, 2007.
- [15] Y. B. Suzen, P. G. Huang, and D. E. Ashpis, "Numerical simulations of flow separation control in low-pressure turbines using plasma actuators," AIAA Paper 2007-937, 2007.
- [16] I. G. Boxx, J. M. Newcamp, M. E. Franke, N. M. Woods, and R. B. Rivir, "A PIV study of a plasma discharge flow-control actuator on a flat plate in an aggressive pressure induced Separation," ASME Paper GT2006-91044, 2006.
- [17] D. Burman, T. W. Simon, U. Kortshagen, and D. Ernie, "Separation control using plasma actuators: steady flow in low pressure turbines," ASME Paper GT-2011-46807, 2011.
- [18] C. Marks, R. Sondergaard, and M. Wolff, "Experimental comparison of DBD plasma actuators for low Reynolds number separation control," ASME Paper GT-2011-45397, 2011.
- [19] T. Matsunuma, "Effects of Reynolds number and freestream turbulence on turbine tip clearance flow," *ASME Journal of Turbomachinery*, vol. 128, no. 1, pp. 166–177, 2006.
- [20] T. Matsunuma, "Unsteady flow field of an axial-flow turbine rotor at a low Reynolds number," *ASME Journal of Turbomachinery*, vol. 129, no. 2, pp. 360–371, 2007.
- [21] P. Magnier, D. Hong, A. Leroy-Chesneau, J. M. Bauchire, and J. Hureau, "Control of separated flows with the ionic wind generated by a DC corona discharge," *Experiments in Fluids*, vol. 42, no. 5, pp. 815–825, 2007.
- [22] T. N. Jukes and K.-S. Choi, "Dielectric-barrier-discharge vortex generators: characterisation and optimisation for flow separation control," *Experiments in Fluids*, vol. 52, no. 2, pp. 329–345, 2012.
- [23] S. J. Kline, J. G. Bardina, and R. C. Strawn, "Correlation of the detachment of two-dimensional turbulent boundary layers," *AIAA Journal*, vol. 21, no. 1, pp. 68–73, 1983.
- [24] J. D. Denton, "Loss mechanisms in turbomachines," *ASME Journal of Turbomachinery*, vol. 115, no. 4, pp. 621–656, 1993.

## Research Article

# Study and Control of a Radial Vaned Diffuser Stall

**Aurélien Marsan,<sup>1</sup> Isabelle Trébinjac,<sup>2</sup> Sylvain Coste,<sup>1</sup> and Gilles Leroy<sup>1</sup>**

<sup>1</sup> Turbomeca, Safran Group, BP 17, 64511 Bordes Cedex, France

<sup>2</sup> LMFA, UMR 5509, Ecole Centrale de Lyon, UCB Lyon I and INSA, 69134 Ecully Cedex, France

Correspondence should be addressed to Aurélien Marsan, aurelien.marsan@ec-lyon.fr

Received 20 July 2012; Accepted 29 October 2012

Academic Editor: Seyed G. Saddoughi

Copyright © 2012 Aurélien Marsan et al. This is an open access article distributed under the Creative Commons Attribution License, which permits unrestricted use, distribution, and reproduction in any medium, provided the original work is properly cited.

The aim of the present study is to evaluate the efficiency of a boundary layer suction technique in case of a centrifugal compressor stage in order to extend its stable operating range. First, an analysis of the flow pattern within the radial vaned diffuser is presented. It highlights the stall of the diffuser vanes when reaching a low massflow. A boundary layer separation in the hub-suction side corner grows when decreasing the massflow from the nominal operating point to the surge and finally leads to a massive stall. An aspiration strategy is investigated in order to control the stall. The suction slot is put in the vicinity of the saddle that originates the main separating skin-friction line, identified thanks to the analysis of the skin-friction pattern. Several aspiration massflow rates are tested, and two different modelings of the aspiration are evaluated. Finally, an efficient control is reached with a removal of only 0,1% of the global massflow and leads—from a steady-state calculations point of view—to an increase by 40% of the compressor operating range extent.

## 1. Introduction

The stable operation of compressors is limited towards low massflow by the occurrence of flow instabilities. To prevent the release of these instabilities, that can be destructive, compressors never operate closer to the stability limit than a chosen massflow. That is called the “surge-margin.” Essential for the stability of the compressor working, it is however in this forbidden part of the operating map that the compressor delivers its maximum pressure ratio, and the surge margin is thus detrimental to the performance of the stage.

The flow phenomena that cause compressor surge are not yet well known. They need to be understood in order to drive design changes that can increase the operating range of the compressor. For the centrifugal compressors, several studies have identified the diffuser as a key zone for the inception of instabilities. In particular, large boundary layer separations may occur in this element as the operating point moves towards surge, leading to rotating stall and/or surge.

A number of investigations have then been done, trying to improve the surge margin using control techniques. Raw [1] demonstrated surge margin improvement by using “porous drilling” to bleed flow from the region of the diffuser

throat. Spakovszky [2] demonstrated an improvement of the surge-margin when injecting air through the shroud surface of the vaneless space in the forward-tangent direction. Skoch [3] continued the investigations and demonstrated other techniques to extend the stable range of the same machine: reverse-tangent injection through the shroud surface of the vaneless space or retractable control tubes inserted through the shroud-side injectors openings. Then, he observed that each of the improvement techniques had the effect of reducing the diffuser leading edge incidence and concluded that reducing the average swirl angle across the span of the vaneless space as the compressor approached surge was the important control action and may be caused by the mere obstruction of the vaneless space due to presence of the injection nozzles.

In the same series of experiments, Skoch also evaluated the effects of hub-side injection into the diffuser throat, since PIV measurements had revealed a hub-corner stall on the pressure side of the vanes of the diffuser, that could suggest the use of air injection into the diffuser passage to energize the flow and control the separation. But these attempts did not demonstrate any significant surge-margin improvement [4]. The only slight effects were found to be due, as for

shroud injection, to the obstruction caused by the injection nozzles and confirmed the previous conclusions made by Skoch about the importance of the angle at diffuser inlet.

The present work also focuses on the development of a control technique in order to extend the stable operating range of a centrifugal compressor. But instead of using injection, and decreasing the flow angle, it aims at controlling the separations that may occur, by using a boundary layer suction technique. That control action has indeed already been used in axial compressor stages or cascades and has provided attractive results [5–8].

An analysis of the flow is first presented, based on the solutions of both steady-state and unsteady simulations. Skin-friction patterns are drawn and reveal the topology of the flow.

Considering the localizations of the singular elements and separation skin-friction lines, an aspiration strategy is discussed and then implemented in the steady-state simulations. Several massflow rate removals are tested, and numerical performances of the aspirated compressor stage are presented.

## 2. Test Case

The test case is a centrifugal compressor stage manufactured by TURBOMECA, Groupe Safran, used for propelling helicopters, and that is representative of the present state of Turbomeca's technical know-how. It is composed of a backswept splitted unshrouded impeller, a radial vaned diffuser, and an axial diffuser. The relative Mach number at impeller leading edge at shroud is about 1, whereas the flow in the diffuser is transonic. The axial diffuser is not taken into account in this study.

Experimental data used for computing the reference performance curves of the test case were provided by Turbomeca and were obtained during the characterization of the compressor stage. In particular, the static pressure was probed at the entry of the impeller, in the middle of the vaneless diffuser, and at the diffuser outlet. As an example, at the diffuser outlet, the experimental value of static pressure is the result of an average over 31 holes equally distributed along the circumference and all connected to the same annular chamber where the pressure is measured.

## 3. Numerical Procedure

Computations were performed with the elsA software developed at Onera. This code solves the compressible RANS equations by a cell-centered finite volume method. The turbulence model chosen for this study is the two-equation model of Smith (k-l), that was shown by Rochuon [9] and Trébinjac et al. [10] to provide results in a good accordance with the experiments in the case of a transonic centrifugal compressor stage. Both steady-state and unsteady numerical computations were performed.

For steady-state simulations, the mixing-plane approach is used for modeling the impeller-diffuser interaction, and the computation domain is reduced to one single passage per

row thanks to a hypothesis of uniformity of flow within all passages.

For the unsteady simulations, a phased-lagged hypothesis is used. The main assumptions of the phase-lagged approach are the geometrical uniformity of the passages and the scrolling of the rotor blades in front of the stator blades as the unique source of flow temporal fluctuations. Under such conditions, there is only a phase difference between the states of passages, and computational domain may be reduced to a single passage per row.

The exit static pressure is set using a prescribed ratio between the pressure and the massflow values through the mesh exit section. This technique, in comparison with a classic simple prescription of the outlet static pressure, allows modeling the flow in the compressor stage beyond the peak of the compressor characteristic, that is necessary in order to study the limit of a compressor operating range, as pointed out by Hill IV [11].

In the elsA software, the prescribed ratio is respected thanks to an evolution of the outlet static pressure between two successive iterations according to the following relation:

$$[p_s]^{(n+1)} = [p_s]^{(n)} \times \left( 1 + \Lambda \times \left[ \frac{[p_s/\dot{m}]^{(n)}}{[p_s/\dot{m}]^{(\text{ref})}} - 1 \right] \right) \quad (1)$$

with  $\Lambda \in [0; 1]$ .

## 4. Stage Mesh

H, C, and O topologies are employed to create a structured multiblock mesh with the commercial meshing software Numeca Autogrid. The complete mesh is composed of 25 blocks, 18 of which describing the impeller geometry and 7 the diffuser. The tip clearance is meshed with an O-H topology, in order to ensure a matching connection with the C-mesh block around the impeller blade and the H behind its trailing edge. As for the vane of the diffuser, it is rounded by an O-block.

The number of points in the impeller tip clearance height is 21.

Fillets are not included. That could be the point for some future extension of study.

The cell width at walls is set to  $1 \mu\text{m}$ . That corresponds to a  $y^+$  parameter approximately equal to 1 along all solid surfaces.

Computations with a more refined mesh in the diffuser, including  $4\text{e}6$  points in the diffuser passage and a coarser one with only  $4\text{e}5$  in the diffuser passage, have also been performed in order to evaluate the mesh dependency of the numerical flow field and in particular of boundary layer separations that occur in the diffuser. Cell width at walls and mesh in the impeller passage have been kept the same.

Table 1 exposes the main dimensions of the meshes, the H-blocks upstream of the impeller, and downstream of the diffuser being not taken into account.

TABLE 1: Main mesh dimensions without upstream and downstream H-blocks.

	Impeller passage	Diffuser passage coarser/normal/refined
Meridional direction	217	73/141/277
Tangential direction	137	37/81/153
Height direction	81	65/77/89

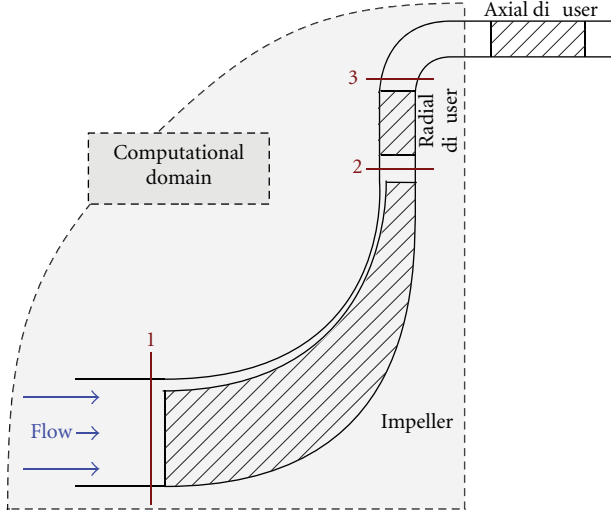


FIGURE 1: Numbering of planes used for performance computation.

## 5. Performance Coefficients Computation

In order to ensure that the flow fields resulting from the numerical simulations are valid, performance curves computed from numerical and experimental data are compared. The numbering of the planes used to express the results is shown in Figure 1. Planes 2 and 3 are planes at constant radius, located at the middle of the vaneless diffuser space and just downstream of the diffuser blade trailing edge, respectively.

When comparing experimental and numerical data, the static pressure numerical values are probed at exactly the same locations than the static pressure sensors. When comparing numerical results only, with and without aspiration, for example, the values are averaged in the entire plane, surface-weighted for static quantities and mass-weighted for total ones.

All performance coefficients are calculated assuming the following hypothesis.

- (i) The area-averaged static pressure values in planes are supposed to be equal to the mean value between the hub static pressure and the shroud one. That allows to calculate total quantities from static pressure measurements at endwalls.
- (ii) The Euler theorem is applied, assuming that the direction of the flow at the impeller inlet is perfectly axial. That is used in order to calculate the flow conditions at diffuser inlet.

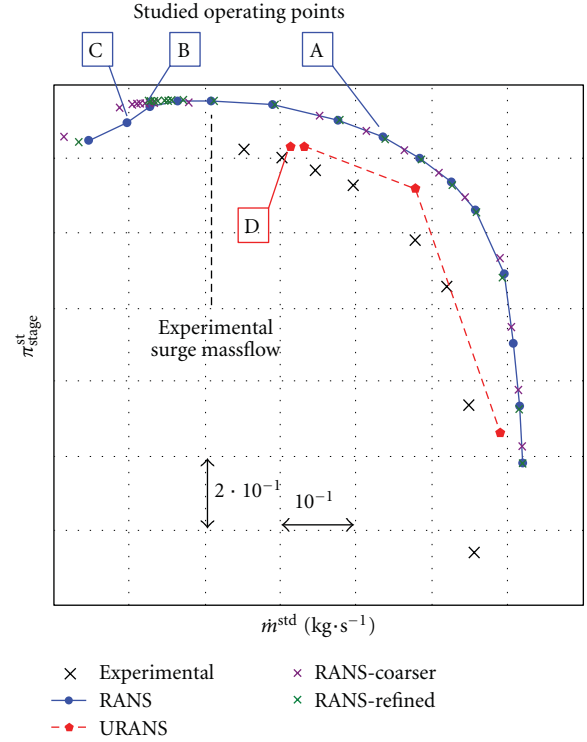


FIGURE 2: Total-to-static compressor stage pressure ratio.

One important parameter for characterizing the diffusion efficiency is the static pressure recovery coefficient of the diffuser stage. It is defined as the pressure rise through the diffuser divided by the inlet dynamic pressure:

$$C_{p,2-3} = C_{p,\text{diffuser}} = \frac{p_{s,3} - p_{s,2}}{P_{t,2} - p_{s,2}}. \quad (2)$$

Performance data relating to the radial vane diffuser are plotted as functions of the ratio (3); Rochuon [9] has demonstrated that this ensures the Mach number and the flow angle to be preserved at the diffuser inlet:

$$C_{\text{impeller}} = \frac{\dot{m}^{\text{std}}}{\pi_{\text{impeller}}^{\text{st}}}. \quad (3)$$

## 6. Overall Performance

Figures 2 and 3 give, respectively, the experimental and numerical total-to-static pressure ratio and the total-to-static isentropic efficiency of the impeller-diffuser compressor stage. Both steady and unsteady numerical results are plotted.

As already observed in a previous work [10], a better correspondence is obtained between experiment and unsteady simulations compared to the stationary ones. In particular, the steady-state computations overvalue the blockage massflow and the pressure ratio of the compressor stage. In addition, operating points that are fully acceptable under convergence criteria can be obtained for massflow much lower than the experimental surge massflow. A global stabilizing effect is due to the mixing-plane approach, to



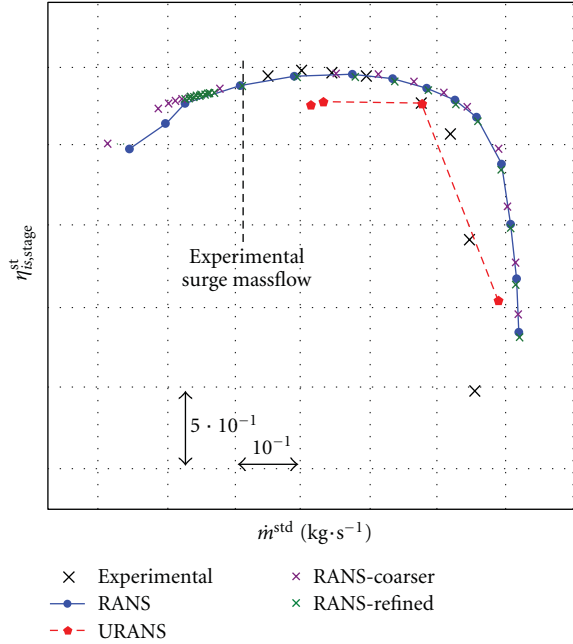


FIGURE 3: Total-to-static compressor stage isentropic efficiency.

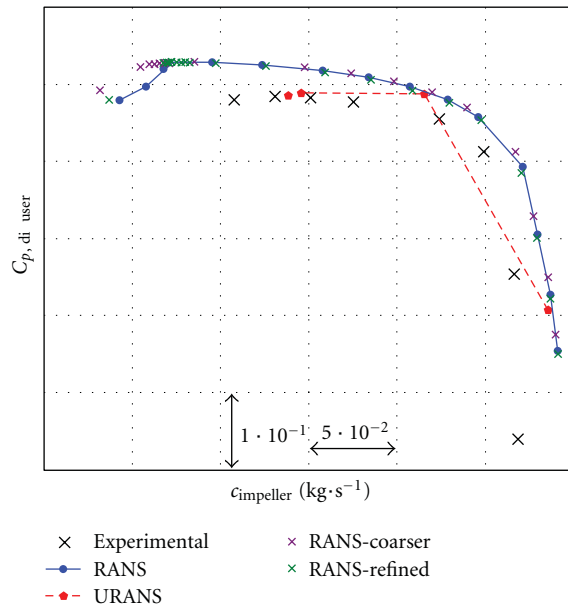


FIGURE 4: Diffuser static pressure recovery coefficient.

the hypothesis of uniformity between the rows passages, and to the evolution of the outlet boundary condition (1). That confirms the important role played by the time-dependent phenomena when reaching the limit of the stable operating range, especially for transonic compressors with small radial gap between impeller and diffuser, in which the flow is significantly affected by diffuser-impeller interactions.

Figure 4 shows the static pressure recovery through the radial vaned diffuser. Again, a better accordance of the URANS simulation with experiments has to be noticed.

Regarding the steady-state simulations, a sudden decrease of the diffuser static pressure recovery occurs when decreasing the massflow and suggests a stall of the diffuser vanes. With the coarser mesh, the decrease is less steep and is predicted at a lower massflow than with the two more refined meshes. However, the study of the flow topology does not reveal any significant difference in stall inception, which will be further presented, and the stall of the diffuser can be considered as mesh independent.

Even if the steady-state model is unable to predict correctly the surge massflow, flow structures that limit its stable numerical operating range can be analyzed, since convergence criteria are respected. Moreover, the existence of the boundary layer separation is also predicted by the phase-lagged model.

A common method to analyze flow separations is the topological study of the skin-friction pattern [12], that can be experimentally observed using, for example, oil stream spread on the solid surfaces by the flow. The next section presents such a study applied on steady-state numerical flow fields. It highlights the growth of a boundary layer separation on the suction side of the diffuser vanes, finally leading to a complete stall when reaching the massflow corresponding to the breakdown of the static pressure recovery coefficient.

## 7. Skin-Friction Pattern for Understanding 3D Flow Separations

Since Prandtl [14] has shown that a two-dimensional flow separates from a no-slip boundary at points where the skin friction vanishes and admits a negative gradient, the comprehension of three-dimensional flow separations has been significantly improved. First, Legendre used the geometric theory of two-dimensional smooth vector fields in order to analyse the skin-friction patterns, locating the critical points and drawing the skin-friction trajectories [12]. The possible critical points are listed in Figure 5.

Later, Lighthill [15] proposed that the convergence of skin-friction lines is a necessary criterion for separation. Contrary to two-dimensional flows, separations occur in three dimensions along particular lines and not at points since the fluid can escape in the third direction. Détery [16] used this criterion in order to analyze a number of separated flow phenomena.

More recently, Surana et al. [13, 17, 18] demonstrated an exact theory of three-dimensional flow separations, taking into account the strength of the skin-friction lines convergence. They found in particular that only four types of separation lines—shown in Figure 6—can engender a unique and well-defined separation surface in physical flow fields. They also demonstrated, thanks to the hyperbolicity of the skin-friction lines, why a potential separation line may not lead to an effective three-dimensional separation.

In the following, the skin-friction patterns on wall surfaces in the diffuser are discussed for the operating points identified in Figure 2. The skin-friction lines are represented using the line integral convolution technique which is a filtering technique to locally blur texture along a vector field

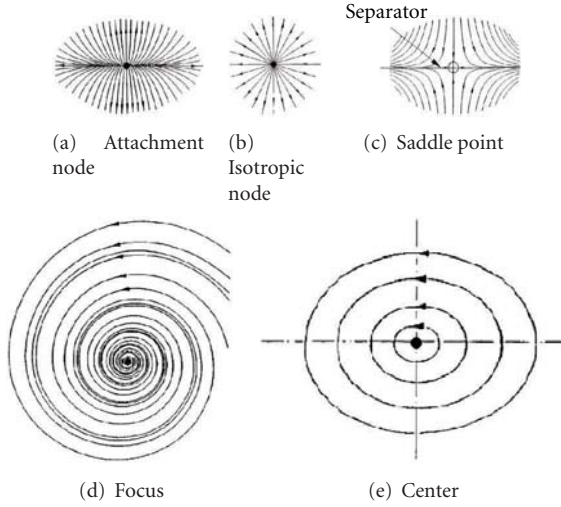


FIGURE 5: Critical points in skin-friction pattern (Délery [12]).

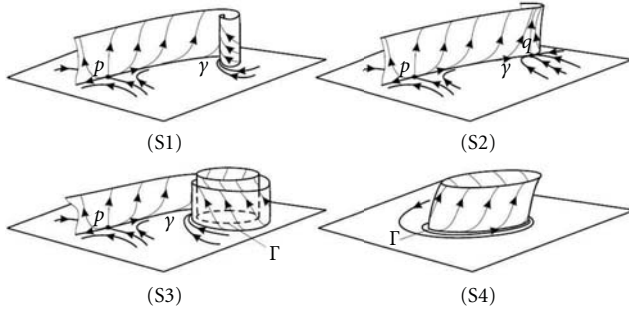


FIGURE 6: The four types of separation lines (Surana et al. [13]).

on a three-dimensional surface [20, 21]. It gives visual results similar to the experimental oil streams visualization and is available in the open source software “Paraview” [22]. For clarity some of the skin-friction lines are enlightened.

## 8. Analysis of the Flow within the Diffuser

**8.1. Steady-State Simulation Results.** Figure 8 shows the topology of the flow on pressure and suction sides of the diffuser vanes for the three operating points labeled A, B, and C in Figure 2.

At the nominal operating point A, a particular flow pattern is located on the pressure side surface near shroud. It is not a separation: the node  $N_{PS,1}$  is the mark of the impact of flow on the pressure surface, of which a part goes upstream toward the saddle  $S_{PS,1}$ . This saddle  $S_{PS,1}$  originates the separation line between the core and the reverse flows and expresses the confrontation between these two parts of flow.

On the vane suction side, two saddles are located in the hub and shroud corner and correspond to the location of the maximal adverse pressure gradient, that is, the diffuser throat. These saddles separate the core flow from the reverse flow in the corners, which may be strengthened by the

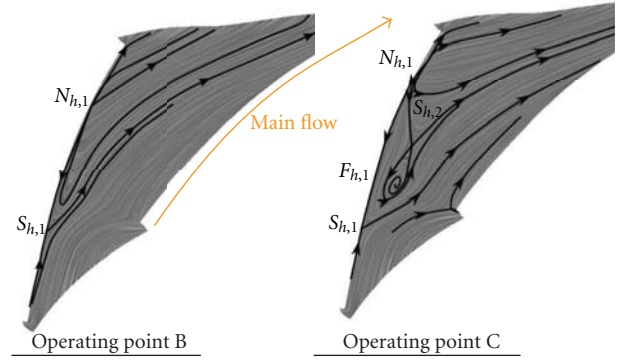


FIGURE 7: Hub skin-friction pattern.

modeling of corners as sharp edges instead of smooth fillets. A further comparison should allow to specify their influence.

At maximal pressure ratio operating point B, the reattachment line  $N_{PS,1}-S_{PS,1}$  on pressure side disappeared. On the other hand, a reverse flow area grows on the suction side and is separated from the core flow by a separation line emanating from a saddle  $S_{SS,1}$ , located at the maximum adverse pressure gradient area, corresponding to the diffuser throat. The skin-friction lines in the bottom quarter of vane height are now captured by a separation focus  $F_{SS,1}$ . Another saddle  $S_{SS,3}$  separates the skin-friction lines captured by  $F_{SS,1}$  from these going toward downstream.

When decreasing more the massflow rate, the focus  $F_{SS,1}$  enlarges and the flow on the half bottom of the diffuser vane is separated. But the main change in the topology of the flow when reaching the stalled configuration concerns the hub surface, represented in Figure 7. The separation line between the core flow and the reverse flow coming from  $N_{h,1}$ , that emanates from the saddle  $S_{h,1}$ , straightens up across the passage, and a reattachment focus  $F_{h,1}$  appears, fed by the vane suction surface detachment focus  $F_{SS,1}$ . Before the stall, the vortex emanating from the focus  $F_{SS,1}$  is convected toward downstream by the core flow, whereas at the stalled operating point, it swoops down on the hub surface. Three-dimensional streamlines that put into evidence this stalled topology are represented in Figure 11.

One should notice that the stalled topology differs from the one widely called as “corner stall,” and described in the work of Lei et al., for example [19]. In the case of a corner stall,  $F_{SS,1}$  and  $F_{h,1}$  would be both detachment focuses, meaning that boundary layers on hub and suction surfaces would both separate at the same location (Figure 9). For the topology studied in this paper, only the suction-side boundary layer separates, and the reversal flow on the hub surface is a consequence of that separation, since flow that escapes from the vane suction side spreads on the hub. In addition, classic hub-corner stall in Figure 9 may be explained by an accumulation of low-momentum fluid in the corner, under the action of the secondary flows.

In the present case, the growth of the corner separation in the hub corner is explained by the cross flow: the overdeviation of the flow near the walls at impeller outlet—see Figure 10—leads to a spanwise distortion of the diffuser

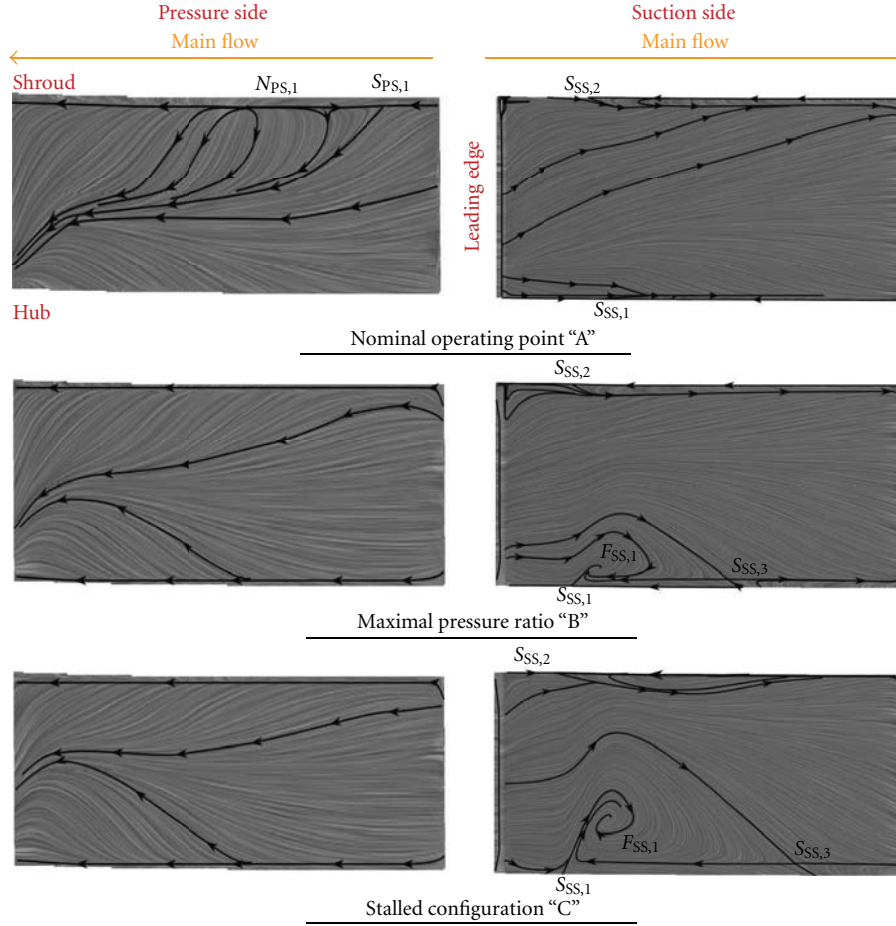


FIGURE 8: Skin-friction patterns on pressure and suction sides of diffuser vanes.

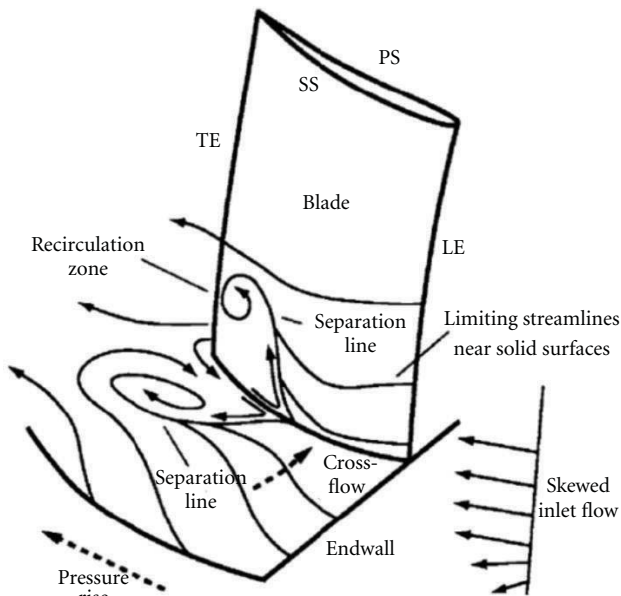


FIGURE 9: Hub-corner stall-limiting streamlines and separation lines (Lei et al. [19]).

flow incidence. The overincidence due to the wake (of the jet-wake flow structure, that is, near the shroud surface) is more pronounced than the overincidence due to the hub boundary layer: that leads to a powerful vortex that carries the flow on the vane suction side from the hub toward the shroud (Figure 12).

**8.2. Time-Averaged Numerical Flow Field.** In order to confirm the existence of the boundary layer separation in the diffuser, the time-averaged flow field coming from the unsteady calculation labeled as D in Figure 2 is considered. The topology of the flow is analyzed and compared to the steady-state one.

Figure 13 exposes skin-friction lines and streamlines for the time-averaged flow field at operating point D. The unsteady model also predicts the boundary layer separation in the diffuser hub-suction side corner. Moreover, the main saddle  $SS_{S,1}$  is located at the same location as in steady-state simulations, that is, at the diffuser throat. But the separated zone is more extended, since the saddle  $SS_{S,3}$ —which is the downstream boundary of the separated zone—is almost on the trailing edge of diffuser vane.

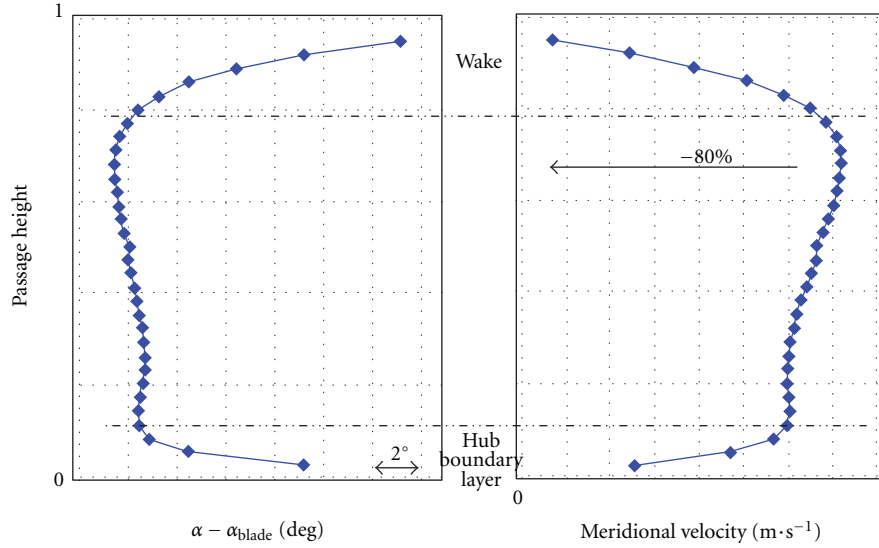


FIGURE 10: Flow conditions at diffuser inlet operating point B.

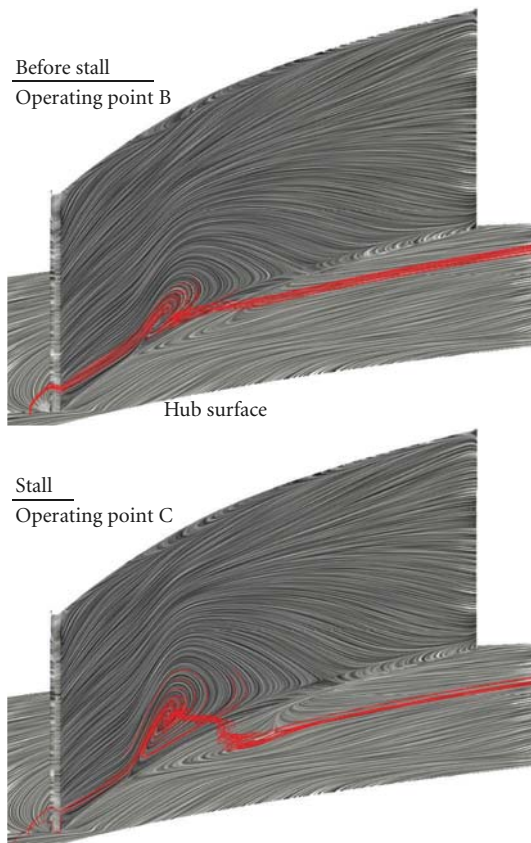


FIGURE 11: Hub-suction side corner separation 3D streamlines.

In addition, a skin-friction pattern including two focuses on both suction and hub surfaces, like the steady stalled one, is periodically observed when looking at the temporal evolution of the skin-friction pattern predicted by the unsteady simulations (Figure 14).

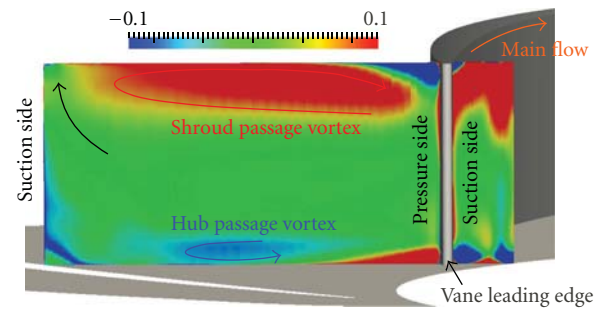


FIGURE 12: Helicity in a section across diffuser passage.

That agreement in flow topology coming from steady and unsteady calculations gives confidence in the boundary layer separation prediction and in the fact that the compressor stable operating range is actually limited by a stall of the radial diffuser vanes.

Then, a control technique aiming at avoiding the diffuser stall and then extending the compressor operating range is developed.

## 9. Aspiration Strategy

**9.1. Location of Suction Device.** In two dimensions, Miller and Chapman [23] have determined that suction should be introduced around the separation point, that can be identified thanks to the zero of the skin-friction coefficient, in order to be the most efficient with the minimum of fluid removal. This zone, schematized in Figure 15, is located at the intersection between the solid surface and the line separating the reverse and the core flow.

In three dimensions, main and reverse flows are separated by a three-dimensional surface, whose intersection with the solid wall is a separation line of one of the four types



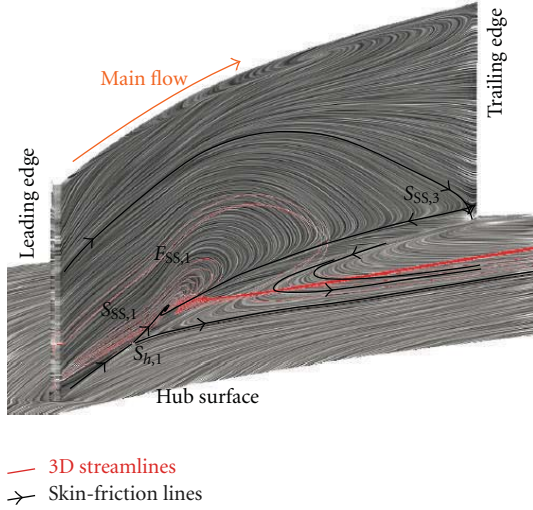


FIGURE 13: Evidence of a boundary-layer separation time-averaged flow field; operating point D.

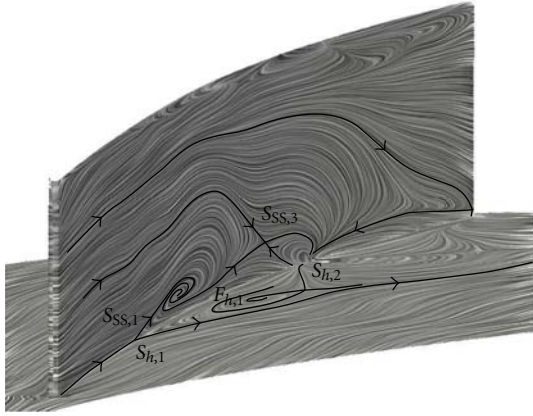


FIGURE 14: Snapshot of the time-varying skin-friction pattern. Existence of a two-focus topology; operating point D.

in Figure 6. This line should be then considered for the development of the aspiration strategy. Considering the stalled skin-friction pattern in Figure 7, the main separation line appears to be the  $S_{SS,1}$ - $F_{SS,1}$  skin-friction line. The suction slot should then be located in the region of the seeds  $S_{SS,1} = S_{h,1}$ , that originates the frontier surface between the core and the reverse flow.

**9.2. Numerical Modeling of Aspiration.** Two ways for modeling the effect of the suction device on the flow have been evaluated.

- (i) The first uses a boundary condition in order to set a surface massflow through the faces of the mesh cells at wall included in the suction slot. This technique is quite easy to use. The precision of the suction slot geometrical description depends on the density of the mesh, that is, the size of the faces describing the hub solid surface.

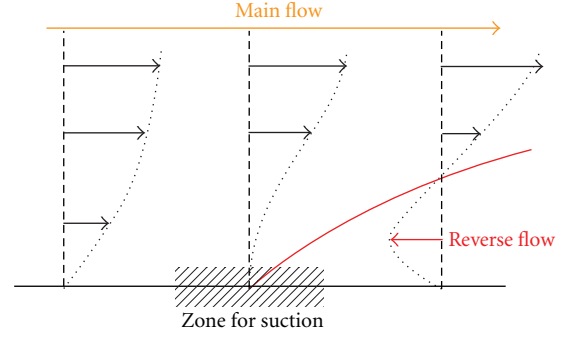


FIGURE 15: Location of suction—2D approach.

- (ii) The second is known as “chimera technique” and is available in the elsA software. This one allows to stack up two or more meshes, in order to model complex geometries using a basic mesh and others more refined describing the solid boundary, back and forth interpolations being done between the stacked meshes. It is now used in a wide range of applications for modeling the technological effects in turbomachinery [24]. The chimera technique involves the meshing of the aspiration slot, whose shape must then be considered.

In this paper, the study of the most efficient shape for suction slot is not a priority. The main aim is to explore the effect of a fluid removal on the performance of the compressor stage and on the flow topology within the diffuser. Then, the first approach for modeling the suction slots is appropriate.

The second modeling was also tested, using a common shape for slot, without fillets, in order to validate the results obtained with the boundary condition technique.

**9.3. Tested Aspiration Device.** Different implementations of suction have been tested:

- (i) a removal of 1 percent of the experimental surge massflow, through the hub surface, along the vane, using boundary limit condition,
- (ii) the same removal of 1 percent of the experimental surge massflow, at the same location, using the chimera technique,
- (iii) a removal of 0,3 percent of the experimental surge massflow rate through the hub surface, with a reduced slot surface compared to the previous case, in order to keep the slot surface massflow constant. The upstream edge of the suction slot is also kept at the same location,
- (iv) a removal of 0,3 percent of the experimental surge massflow, through the vane suction side, keeping again the slot surface massflow constant,
- (v) a removal of 0,1 percent of the experimental surge massflow, through the same suction slot shape as the 0,3% hub-suction case. The slot surface massflow is then reduced,

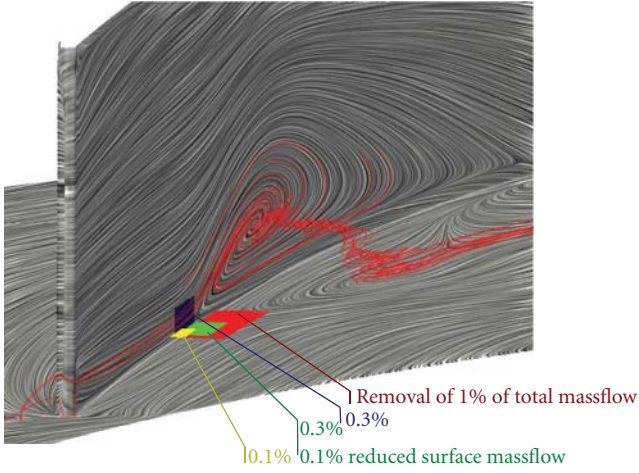


FIGURE 16: Locations of suction slots and percentage of removed massflow; operating point C.

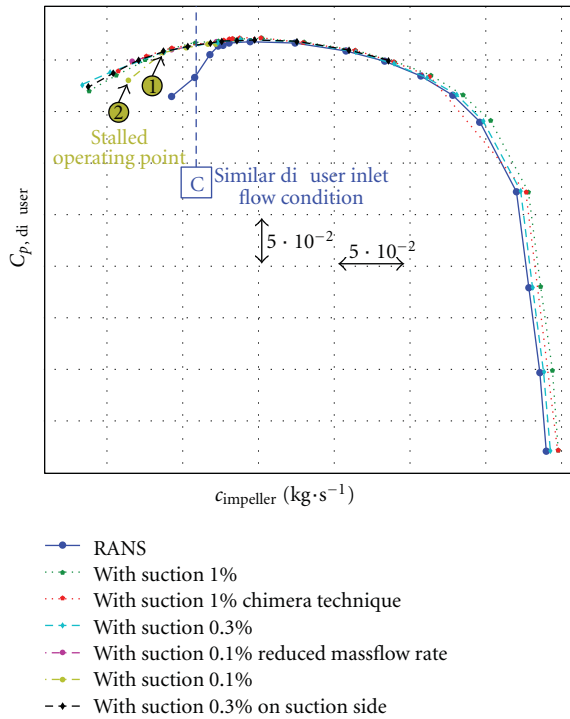


FIGURE 17: Static pressure recovery coefficient of aspirated diffuser.

- (vi) a removal of 0,1 percent of the experimental surge massflow through a smaller suction slot, so that the slot surface massflow is the same as the case of 0,3% hub suction.

Figure 16 summarizes the various tested cases, superimposed on the skin-friction topology of the flow at operating point B.

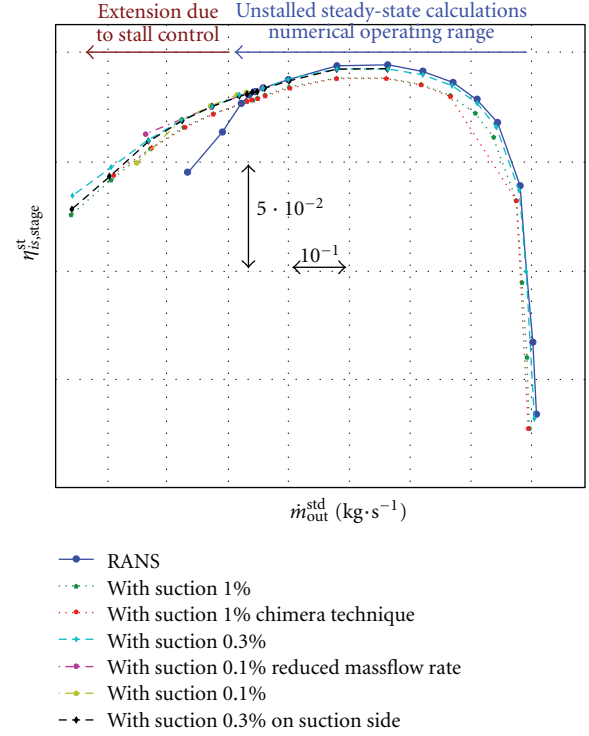


FIGURE 18: Isentropic efficiency of the aspirated compressor stage.

## 10. Aspirated Compressor Stage

**10.1. Global Performance (Steady-State Calculations).** Figure 17 shows the static pressure recovery coefficient of the aspirated diffuser. For comparison, the base case is plotted again.

Figure 18 shows the total-to-static isentropic stage efficiency taking into account the removed massflow defined by (4) as a function of the standard stage outlet massflow defined by (5):

$$\tilde{\eta}_{is, stage}^{st} = \frac{(1 - c_{ms})(\pi_{stage}^{st})^{(\gamma-1)/\gamma} - 1}{T_{t, out}/T_{t, in} - 1}, \quad (4)$$

$$\dot{m}_{out}^{std} = \dot{m}_{out} \times \sqrt{\frac{T_{t, in}}{T_{t, ref}}} \times \frac{P_{t, ref}}{P_{t, in}}. \quad (5)$$

The  $(1 - c_{ms})$  factor in (4) signifies that a perfect isentropic transformation would only compress the amount of flow thrown out at diffuser outlet, without taking the removed massflow into account.

The influences of the aspiration devices on the performance of the stage are predominant for operating points at lowest massflow. The main effect is the withdrawal of the drop of the diffuser static pressure recovery coefficient, the impeller working under the same conditions as without aspiration. Efficiency decrease is moderate and is mainly due to  $(1 - c_{ms})$  factor, that is, to the wasted compressed flow. It obviously becomes negligible for the 0,3% and 0,1% aspirated cases.

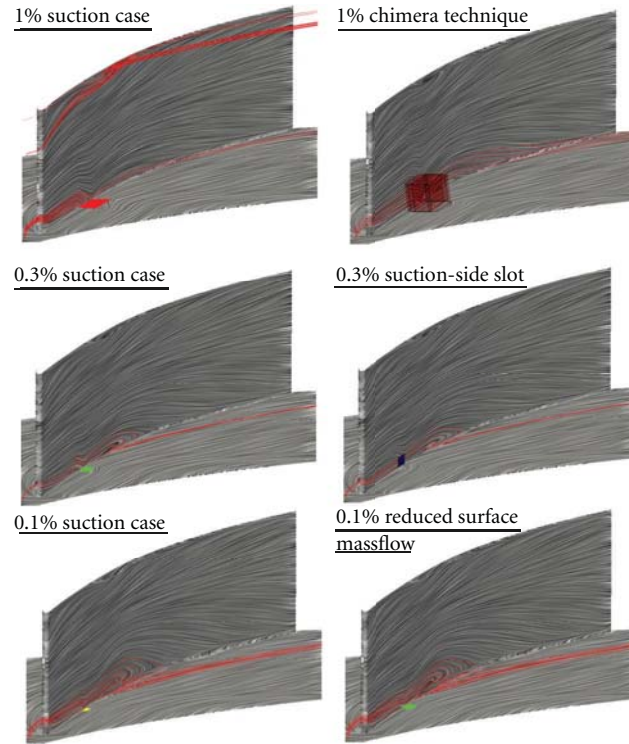


FIGURE 19: Skin-friction patterns for the different aspirated diffusers.

Chimera and boundary limit conditions techniques give both similar results, ensuring the validity of exploring the effect of suction by using the boundary limit condition technique, prior to designing an optimal suction slot.

The vane suction-side suction slot does not improve the performance more than the other configurations and should then be avoided for technical reasons, due to the vane thickness.

In conclusion, the suction technique seems to be a promising way in order to control the stall of the diffuser static pressure recovery. An analysis of the skin-friction pattern within the aspirated diffuser allows to study more precisely the effect of aspiration on flow field.

**10.2. Skin-Friction Patterns with Aspiration.** Figure 19 exposes the skin-friction patterns for the different aspirated cases. In all cases, the inlet diffuser flow conditions are similar to that of operating point C because the ratio (3) is the same (Figure 17).

For the 1% suction cases, the boundary layer separation in the hub-vane suction side corner region is completely removed. Even for the operating point at lowest massflow on Figure 18, no separation occurs. However, a separation focus appears in the shroud-vane suction corner. That observation is in accordance with the absence of any increase in the diffuser static pressure recovery, in spite of the hub-corner boundary layer separation removal. Indeed, the boundary layer separation has switched to another zone, meaning that the fluid is at its maximal diffusion capacity and cannot remain attached on all the walls simultaneously. But

the shroud-corner separation seems to be less critical for the numerical stability. Fully stall-free converged operating points can obtain much lower massflows than the lowest massflow of the base case.

Chimera technique gives similar results, only excepting a small vortex created at the slot downstream edge, which highlights the necessity of an optimization process of the suction slot shape; that is however not a matter of concern for now.

The 0,3% aspirated cases do not achieve a complete control of the hub-corner boundary layer separation and only diminish its extent. Hub and suction-side aspirations have the same effect on the flow field; in particular, the extent of the separation is similarly reduced.

Concerning the 0,1% aspirated cases, the hub-corner boundary layer separation is even less reduced. But the interesting thing is that, at this operating point, the two suction slots lead to a similar effect on the flow, despite the different surface massflows. The total amount of removed fluid is then thought to be the determinant parameter in this case, and not the slot surface massflow.

However, when decreasing more the stage massflow, the degeneration of the separation into a massive stall is not avoided using the smallest suction slot. Figure 20 shows the flow topology for the two operating points marked 1 and 2 in Figure 17. In case 2, the main separating saddle  $S_{SS,1}$  is located just downstream of the suction slot; its inability to delay the stall more is thought to be due to its location, and highlights the sensitivity of the control efficiency to that parameter, especially when the slot is small sized.



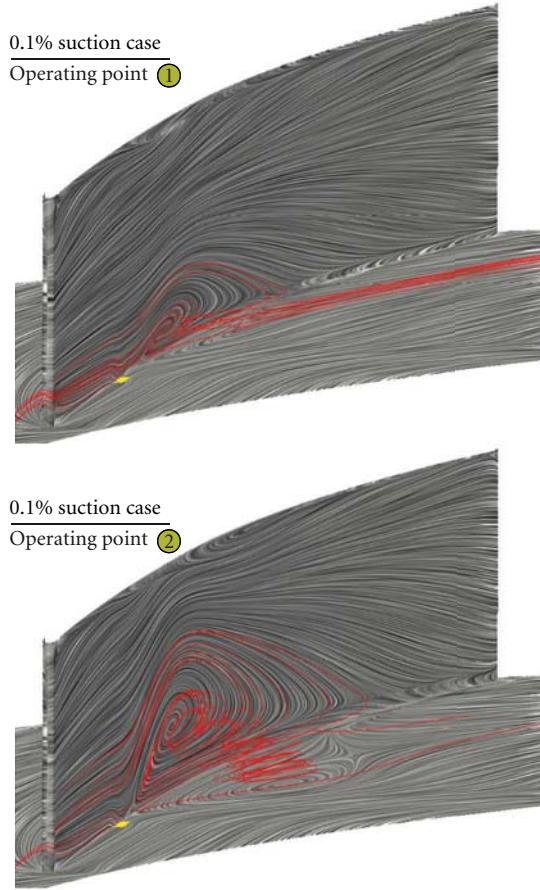


FIGURE 20: Stall of the 0,1% aspirated diffuser.

## 11. Summary and Prospects

A skin-friction pattern investigation within a radial vaned diffuser, aiming to highlight the flow phenomena limiting the stable operating range, has revealed the growth of a boundary layer separation in the diffuser hub-suction side corner. When reaching the numerical stability limit, that boundary layer finally led to a fully stalled flow pattern, causing a dropdown of the diffuser static pressure recovery coefficient and thus of the global compressor stage performances.

The existence of that boundary layer separation was confirmed by phase-lagged models results.

Taking into account the location of the skin-friction pattern critical points, a boundary layer suction technique was developed. The main separation saddle was located, and the suction slot was placed in its vicinity.

Several cases were tested, and an effective control of the diffuser stall has been reached with a removal of only 0,1% of the total stage massflow. From a steady-state point of view, that effective control has led to an increase by 40% of the stall-free diffuser operating range.

Comparison between the various suction configurations has not revealed any significant differences between the results obtained with a hub or a suction-side suction slot.

And the amount of fluid removal was thought to be the determining factor, not the slot surface massflow.

In spite of these encouraging results, it is well known that the unsteadiness plays a leading role in case of transonic centrifugal compressors operating near surge. The aspiration technique—whose development has been based on the results of steady-state model, that stabilizes operating points for massflows lower than the experimental surge massflow—should then be implemented in unsteady calculations in order to ensure its efficiency and the increase of the operating range.

The validity of single-passage calculations should also be examined, since it may have a stabilizing effect on the numerical simulations, maybe as important as the time-dependent effects due to impeller-diffuser interaction.

The influence of the fillets on the flow topology should also be evaluated in future work, since it may modify the adequate location of the suction slot.

The major role played by the vortex created by the overincidence on diffuser vane near the shroud was also pointed out by the present study. It may then be interesting to evaluate other design techniques, that would take that observation into account. In particular, the vane of the studied diffuser is of 2D shape, with a leading edge that is just a line parallel to axis of revolution, and the hub wall is of planar shape. Studies have already shown that potential improvements could be obtained thanks to a redesign of the diffuser leading edge [25, 26]. A passive control strategy of the hub boundary layer separation, based on geometrical modifications of the diffuser vane and hub shapes, without any waste of compressed flow, should then be investigated.

## Nomenclature

PS, SS:	Blade pressure side, suction side
$\dot{m}$ :	Massflow
$\dot{m}^{\text{std}}$ :	Corrected massflow for impeller inlet at standard conditions
$\pi_{\text{impeller}}^{\text{st}}$ :	Impeller static pressure ratio
$C_{p,\text{diffuser}}$ :	Static pressure recovery coefficient of the diffuser
$p_s$ :	Static pressure
$T_t$ :	Total temperature
$P_t$ :	Total pressure
$\omega$ :	Impeller rotational speed
$\alpha$ :	Absolute flow angle
$N_s = \omega \sqrt{\dot{m}} / \Delta H^{3/4}$ :	Compressor specific speed
$[\dots]^{(n)}$ :	Value at the $n$ th calculation step.

## Acknowledgments

The authors would like to thank Turbomeca, Groupe Safran, which supported this research. Thanks also go to the French Aerospace laboratories, Onéra, that provides the numerical code, elsA, and to the *Agence Nationale de la Recherche et de la Technologie* that promotes the collaboration between research laboratories and industrialists.

## References

- [1] J. A. Raw, "Surge margin enhancement by a porous throat diffuser," *Canadian Aeronautics and Space Journal*, vol. 32, no. 1, pp. 54–60, 1986.
- [2] Z. S. Spakovszky, "Backward traveling rotating stall waves in centrifugal compressors," *Journal of Turbomachinery*, vol. 126, no. 1, pp. 1–12, 2004.
- [3] G. J. Skoch, "Experimental investigation of centrifugal compressor stabilization techniques," *Journal of Turbomachinery*, vol. 125, no. 4, pp. 704–713, 2003.
- [4] G. J. Skoch, "Experimental investigation of diffuser hub injection to improve centrifugal compressor stability," *Journal of Turbomachinery*, vol. 127, no. 1, pp. 107–117, 2005.
- [5] J. L. Kerrebrock, A. H. Epstein, A. A. Merchant et al., "Design and test of an aspirated counter-rotating fan," *Journal of Turbomachinery*, vol. 130, no. 2, Article ID 021004, 2008.
- [6] A. Sachdeva, *Study and control of three-dimensional flow separations in a high pressure compressor stator blade row with boundary layer aspiration [Ph.D. thesis]*, Ecole Centrale de Lyon, 2010.
- [7] A. Godard, *Etude numerique et experimentale d'un compresseur aspire [Ph.D. thesis]*, Ecole Centrale de Lyon, 2010.
- [8] J. L. Kerrebrock, "Aspirated compressors = shorter and lighter engines: a boon for supercruising jets," *Aero-Astro*, (2), 2005, <http://aeroastro.mit.edu/news-events/aeroastro-annualreport>.
- [9] N. Rochuon, *Analyse de l'écoulement tridimensionnel et instationnaire dans un compresseur centrifuge à fort taux de pression [Ph.D. thesis]*, Ecole Centrale de Lyon, 2007.
- [10] I. Trébinjac, P. Kulisa, N. Bulot, and N. Rochuon, "Effect of unsteadiness on the performance of a transonic centrifugal compressor stage," *Journal of Turbomachinery*, vol. 131, no. 4, Article ID 041011, 9 pages, 2009.
- [11] R. A. Hill IV, *Simulation of spike stall inception in a radial vaned diffuser [Ph.D. thesis]*, Massachusetts Institute of Technology, 2007.
- [12] J. M. Délery, "Robert legendre and henri werlé: toward the elucidation of three-dimensional separation," *Annual Review of Fluid Mechanics*, vol. 33, pp. 129–154, 2001.
- [13] A. Surana, G. B. Jacobs, O. Grunberg, and G. Haller, "An exact theory of three-dimensional fixed separation in unsteady flows," *Physics of Fluids*, vol. 20, no. 10, Article ID 107101, 2008.
- [14] L. Prandtl, "Flüssigkeit bei sehr kleine Reibung," *Verhandlungen des dritten internationalen mathematischen Kongresses*, Heidelberg, Germany, 1904, <http://webdoc.sub.gwdg.de/univ-erlag/2010/GKSM3.pdf>.
- [15] M. J. Lighthill, *Attachment and Separation in Three-Dimensional Flow*, Laminar Boundary Layers, Oxford University Press, 1963.
- [16] J. M. Délery, "Topologie des écoulements tridimensionnels décollés stationnaires: points singuliers, séparatrices et structures tourbillonnaires," Onéra, Département d'Aérodynamique Fondamentale et Expérimentale, 1999.
- [17] A. Surana, O. Grunberg, and G. Haller, "Exact theory of three-dimensional flow separation. Part 1. Steady separation," *Journal of Fluid Mechanics*, vol. 564, pp. 57–103, 2006.
- [18] A. Surana, G. B. Jacobs, O. Grunberg, and G. Haller, "An exact theory of three-dimensional fixed separation in unsteady flows," *Physics of Fluids*, vol. 20, no. 10, Article ID 107101, 22 pages, 2008.
- [19] V. M. Lei, Z. S. Spakovszky, and E. M. Greitzer, "A criterion for axial compressor hub-corner stall," in *Proceedings of the ASME 51st Turbo Expo*, pp. 475–486, May 2006.
- [20] B. Cabral and L. Leedom, "Imaging vector fields using line integral convolution," in *Proceedings of the 20th annual conference on Computer graphics and interactive techniques (ACM '93)*, pp. 263–270, New York, NY, USA, August 1993.
- [21] A. Sundquist, "Dynamic line integral convolution for visualizing streamline evolution," *IEEE Transactions on Visualization and Computer Graphics*, vol. 9, no. 3, pp. 273–282, 2003.
- [22] Paraview UsersGuide 3.14, Kitware, 2012, <http://www.paraview.org/paraview/resources/software.php>.
- [23] M. L. Miller and D. C. Chapman, "Single-stage experimental evaluation of boundary layer bleed techniques for high lift stator blades," NASA, CR-54569, 1968, [http://www.archive.org/details/nasa\\_techdoc\\_19680019149](http://www.archive.org/details/nasa_techdoc_19680019149).
- [24] L. Castillon, G. Billonnet, S. Péron, and C. Benoit, "Numerical simulations of technological effects encountered on turbomachinery configurations with the chimera technique," in *Proceedings of 27th International Congress of the Aeronautical Sciences*, Nice, France, 2010.
- [25] E. Casartelli, A. P. Saxer, and G. Gyarmathy, "Numerical flow analysis in a subsonic vaned radial diffuser with leading edge redesign," *Journal of Turbomachinery*, vol. 121, no. 1, pp. 119–126, 1999.
- [26] Z. Palat, "Design Optimization and Test of Advanced Small Scale Compressor," NEWAC Workshop 2010, Munich, Germany, 2010, <http://www.newac.eu/88.0.html>.

## Research Article

# Leakage Characteristic of Helical Groove Seal Designed in Reactor Coolant Pump

Meng Zhang,<sup>1</sup> Xiao-fang Wang,<sup>1</sup> Sheng-li Xu,<sup>1</sup> and Shuo Yin<sup>1,2</sup>

<sup>1</sup> School of Energy and Power Engineering, Dalian University of Technology, No. 2, Linggong Road, Liaoning, Dalian 116024, China

<sup>2</sup> Laboratoire d'Etudes et de Recherches sur les Matériaux, les Procédés et les Surfaces (LERMPS), Université de Technologie de Belfort-Montbéliard, Site de Sévenans, 90010 Belfort Cedex, France

Correspondence should be addressed to Meng Zhang, zmdlut@qq.com

Received 30 August 2012; Revised 13 November 2012; Accepted 14 November 2012

Academic Editor: Seyed G. Saddoughi

Copyright © 2012 Meng Zhang et al. This is an open access article distributed under the Creative Commons Attribution License, which permits unrestricted use, distribution, and reproduction in any medium, provided the original work is properly cited.

Helical groove seal is designed in reactor coolant pump to control the leakage along the front surface of the impeller face due to its higher resistance than the circumferentially grooved seal. The flow and the friction factors in helical groove seals are predicted by employing a commercial CFD code, FLUENT. The friction factors of the helical groove seals with helix angles varying from 20 deg to 50 deg, at a range of rotational speed and axial Reynolds number, were, respectively, calculated. For the helically grooved stator with the helix angle greater than 20 deg, the leakage shows an upward trend with the helix angle. The circumferentially grooved stator has a lower resistance to leakage than the 20 deg and 30 deg stators. It can be predicated that, for a bigger helix angle, the friction factor increases slightly with an increase in high axial Reynolds number, which arises from the high-pressure operation condition, and the friction factor is generally sensitive to changes in the helix angle in this operation condition. The study lays the theoretical foundation for liquid seal design of reactor coolant pump and future experimental study to account for the high-pressure condition affecting the leakage characteristic.

## 1. Introduction

Recently, it has been recognized that the leakage flow of highly effective seal is the key point of nuclear plant safety. Leakage flow characteristics of the seal in the nuclear equipment were investigated by several researchers.

In high temperature gas-cooled reactor (HTGR) core, the prevention of leakage flows of coolant gas is important for a thermal hydraulic design; the seal mechanism for the core was researched by Kaburaki and Takizuka [1, 2]. The leakage flows through the gaps between core support blocks were restricted because the gap between the core support blocks was still kept wide during the reactor operation to prevent the interaction of the blocks.

The improvements in the leakage along the front surface of the impeller face are the key point of reactor coolant pump (RCP) reliability. Leakage control in the clearance is the most important problem to be solved, which can increase the reliability and efficiency of RCP and, thus, assure the satisfactory operation. If the leakage is out of control,

the leakage flow will disturb the main flow at the inlet of the impeller, and then the circulation area will decrease. It will lead to a decrease of the hydraulic efficiency of RCP. Once the pump operates on a low head due to the larger leakage, there will be a serious danger of water coolant undersupply, which leads to excess reactor core temperature.

To gain a better leakage control, circumferentially grooved seal is commonly used in the pump. But its performance in the high-pressure condition is unsatisfied. To fit in the extreme condition, helical groove seal is designed in reactor coolant pump to obtain a higher resistance to leakage than the circumferentially grooved seal. High rotational speed yields backflow along the groove-forward inlet and reduction in the average axial and circumferential fluid velocity. Beyond that, the helically grooved stator application is to remove any impurities through the groove path.

However, helically grooved seals have not been investigated thoroughly because of their complex characteristics. Bootsma [3] investigated the spiral-groove bearings by employing a turbulence model, which was similar to Hirs [4].

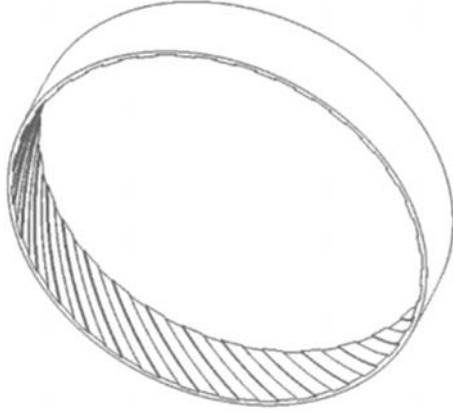


FIGURE 1: Helically grooved stator.

Kim and Childs' [5] model evaluated a bulk-flow analysis for helical groove seals with grooved rotors and grooved stators. The analysis also incorporated both Hirs [4] turbulent lubrication theory and "fine-groove" theory. The governing equations were expanded in the eccentricity ratio to yield zeroth and first-order perturbation solutions. Additionally, Walowit [6] developed a fine-groove-based analysis for laminar helical groove seals; however, it was not suitable for the highly turbulent flow.

Kim and Childs [5] predicted that the helically grooved stator is more stable than the helically grooved rotor. But the helically grooved stator configuration had higher leakage rate than the helically grooved rotor configuration due to its significantly lower power consumption. Besides, Iwatsubo et al. [7] reported that the formation of the negative cross-coupled stiffness coefficients was the reason why helically grooved stator was more stable.

Some studies were presented to determine the leakage characteristics of helical groove seals, which were just operated in the low-pressure condition. Kanki and Kawakami [8] reported that the leakage flow of the helical groove seal was less than that of the plain seal. The effect of the helical groove was predominant in the high-speed region. Iwatsubo et al. [9] performed a systematic analysis on turbulent annular seals with a helically grooved rotor. As the journal rotating frequency increased, the leakage flow decreased. Zero net leakage flow was possible at a particular rotating frequency. The leakage data and friction factors were presented for helical groove seals by Childs et al. [10]. The test results supported the conclusion that the number of grooves and the leakage rates increased steadily with increasing the helix angles in the low pressure.

Gowda and Prabhu [11] present theoretical investigations of high-pressure annular seal that deal with the steady-state mass flow rate, labyrinth seal-influence coefficients, and unbalance response of a high-pressure fuel turbo pump.

Before this paper, the leakage characteristic of the helical groove seal in the pressure higher than 17 MPa condition has not been researched. To fit in the extreme condition, helical groove seal is designed to control the leakage in reactor

coolant pump. To obtain helical groove seal with high-resistance, this paper is initiated to predict a high friction factor for a proper choice of the helix angle  $\alpha$  in the high pressure condition.

## 2. Computational Descriptions

**2.1. Model.** A three-dimensional CFD model is used in this study to calculate the steady incompressible flow within the seal. Water is employed as the sealing medium, and the temperature is treated as a constant value. The leakage characteristics are determined by employing the standard  $\kappa$ - $\epsilon$  turbulence model, and CFD analysis of the seal is performed by ANSYS FLUENT.

The turbulence kinetic energy,  $k$ , and its rate of dissipation,  $\epsilon$ , are obtained from the following transport equations:

$$\begin{aligned} \frac{\partial}{\partial t}(\rho k) + \frac{\partial}{\partial x_i}(\rho k u_i) &= \frac{\partial}{\partial x_j} \left[ \left( \mu + \frac{\mu_t}{\sigma_k} \right) \frac{\partial k}{\partial x_j} \right] \\ &+ G_k + G_b - \rho \epsilon - Y_M + S_k, \\ \frac{\partial}{\partial t}(\rho \epsilon) + \frac{\partial}{\partial x_i}(\rho \epsilon u_i) &= \frac{\partial}{\partial x_j} \left[ \left( \mu + \frac{\mu_t}{\sigma_\epsilon} \right) \frac{\partial \epsilon}{\partial x_j} \right] \\ &+ C_{1\epsilon} \frac{\epsilon}{k} (G_k + C_{3\epsilon} G_b) - C_{2\epsilon} \rho \frac{\epsilon^2}{k} + S_\epsilon, \end{aligned} \quad (1)$$

where

$$\mu_t = \rho C_\mu \frac{k^2}{\epsilon}. \quad (2)$$

In these equations,  $G_k$  represents the generation of turbulence kinetic energy due to the mean velocity gradients;  $G_b$  is the generation of turbulence kinetic energy due to buoyancy;  $Y_M$  represents the contribution of the fluctuating dilatation in compressible turbulence to the overall dissipation rate. The model constants  $C_{1\epsilon} = 1.44$ ,  $C_{2\epsilon} = 1.92$ ,  $C_\mu = 0.09$ , and  $\sigma_k = 1.0$ ,  $\sigma_\epsilon = 1.3$  are the turbulent Prandtl numbers for  $k$  and  $\epsilon$ , respectively.  $S_k$  and  $S_\epsilon$  are user-defined source terms [12]. The capability of the  $\kappa$ - $\epsilon$  turbulence model for the grooved liquid annular seal has been validated by comparison between the computed results and the three-dimensional laser Doppler anemometer measurements [13].

A second order discretization scheme is used for the pressure, density, and momentum terms. First-order upwind scheme is used for turbulent dissipation rate terms. Resolving boundary layers, standard wall function is used to model the viscous effects in the near-wall regions. The convergence criterion for continuity, velocity,  $\kappa$ , and  $\epsilon$  equations is below  $10^{-5}$ . Parametric study is conducted over a wide range of Reynolds number (90000–245000). Pressure outlet boundary is maintained at constant value, and the inlet pressure is changed to achieve different Reynolds number.

**2.2. Dimensions and Conditions.** A typical helically grooved stator annular seal is illustrated in Figure 1. The seals used in this paper provide smooth rotor and helically grooved stator.



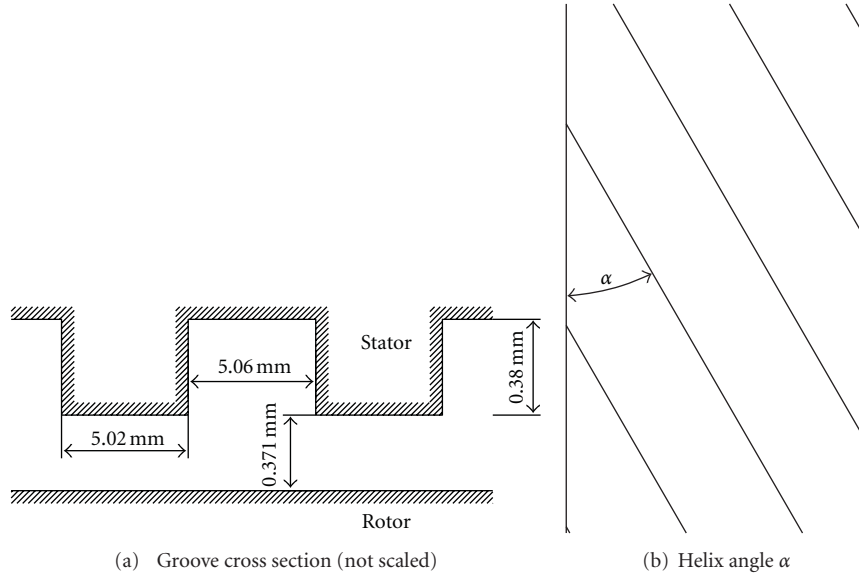


FIGURE 2: Groove dimension.

The helical groove results in fluid rotation in a direction opposite to the shaft rotation.

The helix angle  $\alpha$  is set to oppose the fluid rotation and yields a reduction in the average axial and circumferential fluid velocity. The angle  $\alpha$  can vary from zero (circumferential grooving) to 90 deg (axial grooving).

The five seal configurations were computed to evaluate the influence of helix angle  $\alpha$  on the leakage characteristics. Figure 2 provides the seal nominal dimensions. Five helix angles, namely, 0, 20, 30, 40, and 50 deg, were computed. These seals maintain the same cross section as the inlet as shown in Figure 2(a). The seal length is 50 mm, and the rotor diameter is 100 mm. Computational results are presented for an outlet pressure of 17.1 MPa.

**2.3. Mesh Generation.** The 3D mesh applying the structured hexagonal cells for the land and groove is created using the commercial mesh generator Gambit. The 2D view for the inlet section of the helical groove seal mesh is defined as shown in Figure 3. A mesh independent density study is performed to investigate the effect of mesh density and to determine how fine a mesh is required to capture the important pressure physics. The mesh is refined in the radial direction and circumferential direction dependently. Figure 4 shows the effect of refining the mesh in the cross section on the inlet average pressure. The pressure varies less than 0.002% with increasing mesh density and is mesh independent. To obtain a better pressure prediction, maximum density mesh will be used in subsequent calculations.

Starting with the one node away from the wall, the mesh points are redistributed as the double-sided ratio 1.15 in the radial direction and 1.2 in the circumferential direction of the groove width. The near-wall mesh points are disturbed so as to maintain a smaller value  $y^+$ , resulting in improved wall shear stress and pressure prediction.



FIGURE 3: 2D view for the inlet section mesh.

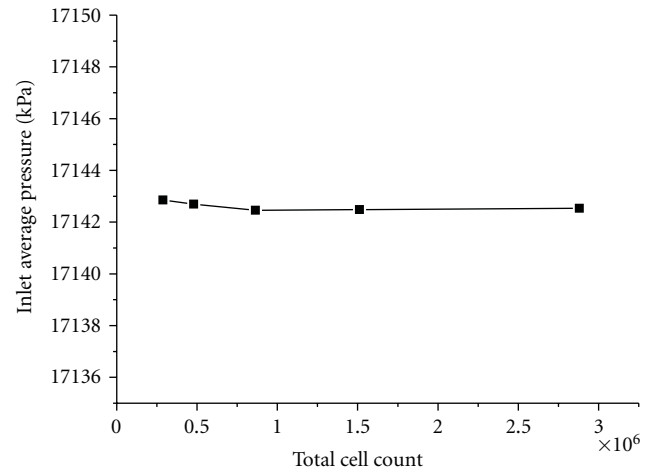


FIGURE 4: Mesh density study.

Law-of-the-wall formulations model the sharp pressure gradients near the wall and are used with standard  $\kappa$ - $\epsilon$  turbulence model as follows:

$$U^* = y^* \quad \text{for } y^* < 11.225, \quad (3)$$

$$U^* = \frac{1}{\kappa} \ln(Ey^*) \quad \text{for } y^* > 11.225,$$

where

$$U^* \equiv \frac{U_P C_\mu^{1/4} k_P^{1/2}}{\tau_w / \rho} \quad (4)$$

is the dimensionless velocity.



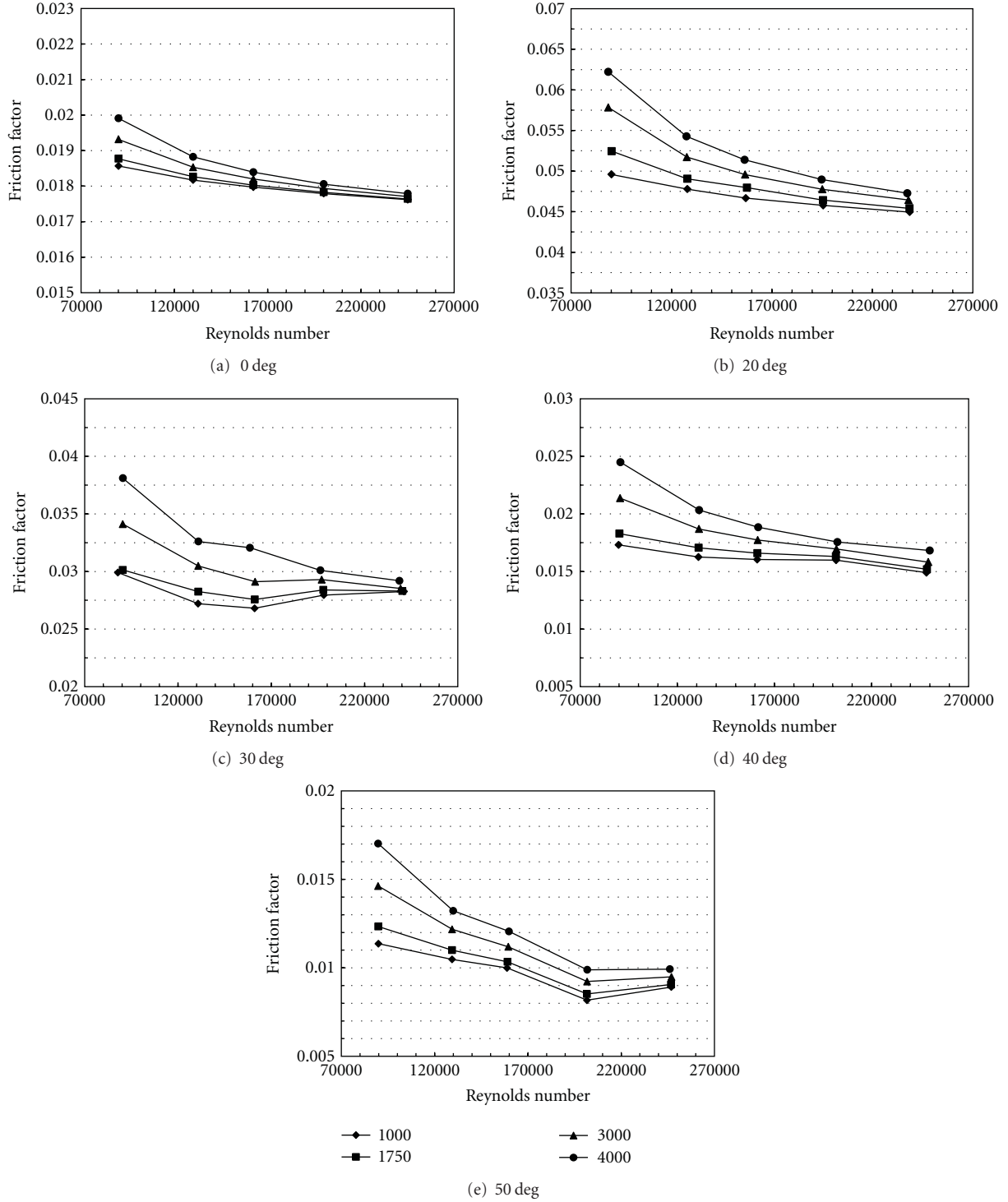


FIGURE 5: Friction factor for five helix angles.

Consider that

$$y^* \equiv \frac{\rho C_\mu^{1/4} k_P^{1/2} y_P}{\mu} \quad (5)$$

is the dimensionless distance from the wall,  $C_\mu$  = turbulent viscosity constant ( $= 0.09$ ),  $\kappa$  = von Kármán constant

( $= 0.4187$ ),  $E$  = empirical constant ( $= 9.793$ ),  $U_P$  = mean velocity of the fluid at the near-wall node  $P$ ,  $k_P$  = turbulence kinetic energy at the near-wall node  $P$ ,  $y_P$  = distance from point  $P$  to the wall, and  $\mu$  = dynamic viscosity of the fluid.

The laws of the wall for mean velocity and pressure are based on the wall unit,  $y^*$ , rather than  $y^+$  ( $\equiv \rho u_\tau y / \mu$ ).

These quantities are approximately equal in equilibrium turbulent boundary layers [12].

### 3. Results and Discussion

Two faces are located about the midplane of the seal at 0.23 and 0.5 of the seal length. The pressure differential is defined as the pressure computed upstream and immediately inside the seal. The axial pressure gradient is defined by the two average pressure faces at 0.23 $L$  and 0.5 $L$ . The seal length,  $L$ , is 50 mm.

The friction factor definition reference of Childs et al. [10] is modified. The minimum clearance is replaced by the hydraulic diameter, because that is a better representation for the frictional head loss coefficient. The following definition is used for the friction factor developed in the seals:

$$\lambda = -\frac{dP}{dZ} \cdot \frac{D}{2\rho v^2}, \quad (6)$$

where  $P$  is the static pressure,  $Z$  is the axial seal coordinate,  $D$  is the hydraulic diameter,  $\rho$  is the density, and  $v$  is the average axial velocity. Figure 5 illustrates the friction factor versus the axial Reynolds number,  $Re = \nu D \rho / \mu$ , and the rotational speed for stators with the helix angle of 0, 20, 30, 40, and 50 deg.

**3.1. Helix Angle.** There are comparable representative resistance characteristics among the five models. As can be observed from Figure 5, for all helically grooved stators, the friction factor shows an upward trend with the helix angle reduction, because the seal with a smaller helix angle has less axial component flow and longer groove in favour of energy dissipation. And it becomes more sensitive to the rotational speed when the helix angle decreases. For the helically grooved stators, the friction factor generally decreases with the increasing axial Reynolds number. At the condition of low axial Reynolds number, it obviously drops monotonically with axial Reynolds number. At comparatively high axial Reynolds number, for  $\alpha = 30, 40$ , and 50 deg, the friction factor tends to converge to the same value with axial Reynolds number, and the friction factor even increases slightly with axial Reynolds number at the low rotational speed condition. The curve tends to get in self-simulated domain with axial Reynolds number higher than 250000.

**3.2. Rotational Speed.** As can be observed from Figure 5, for all helically grooved stator, the friction factor generally increases with increasing the running speed. Figure 6 shows the variation of the friction factor with the axial Reynolds number for all the stators at 1750 rpm. 20 deg stator has higher resistance to leakage than the remaining stator. For the helix angle greater than 20 deg, the helically grooved stators leak increasingly more as the helix angle increases, because the leakage flow in the groove with greater helix angle has more axial component flow and shorter groove at the lack of energy dissipation. The circumferentially grooved stator has lower friction factor than the 20 and 30 deg stators because it cannot yield backflow along the groove-forward inlet.

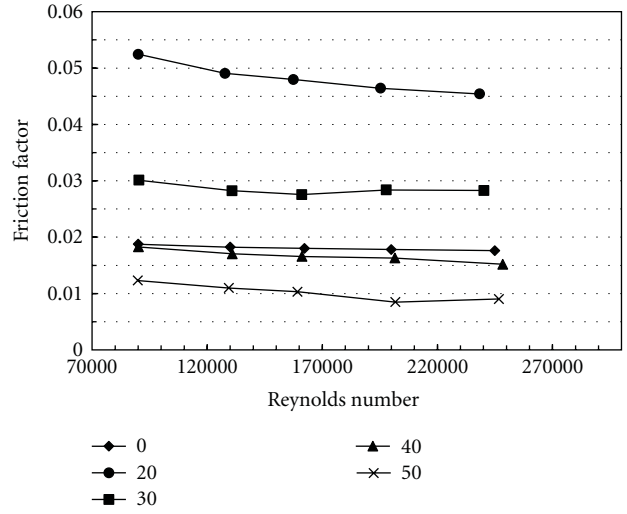


FIGURE 6: Friction factor for helically grooved stators at 1750 rpm versus  $Re$ .

Figure 7 illustrates the friction factor for helically grooved stators at 4000 rpm versus axial Reynolds number. It is clear that the 20 and 30 deg stators have higher resistance to leakage than the circumferentially grooved stator. At low axial Reynolds number, 40 deg stator surpasses the circumferentially grooved stator in friction value due to the increment in the rotational speed. Increasing rotational speed yields more backflow along the groove forward inlet and reduction in the average axial and circumferential fluid velocity.

**3.3. Flow Field.** Figure 8 shows the pressure contour of the circumferentially grooved stator. It is clear that the pressure contour gradient vector of circumferentially grooved stator is parallel to the rotor axis. Comparatively, in Figure 9, which shows the pressure contour of 20 deg stator, it can be found that the stagnation area exists along the upwind surface of the groove due to the impingement of rotational fluid. Fluid rotation opposes the helix angle  $\alpha$ , and it yields a reduction in the average circumferential fluid velocity that ensures the seal stability. Figure 10 shows the pressure contour of 0.2 $L$  cross section for four helix angles. The value range of the pressure becomes narrower, and the peak value declines as the helix angle increases. The stagnation region shrinks in area and moves to leeward as the helix angle increases. This fact influences the distribution of the turbulent kinetic energy, which can be found in Figure 11 showing the turbulent kinetic energy contour of 0.2 $L$  cross section for four helix angles.

The turbulent kinetic energy value is related to the energy dissipation. It is seen that the turbulent kinetic energy of 20 deg stator is higher than any other stator, and the highly turbulent kinetic energy region existing on the left of the groove is the largest, which is in favour of energy dissipation. The highly turbulent kinetic energy region shrinks in area and moves to leeward as the helix angle increases. The highly turbulent kinetic energy region of the

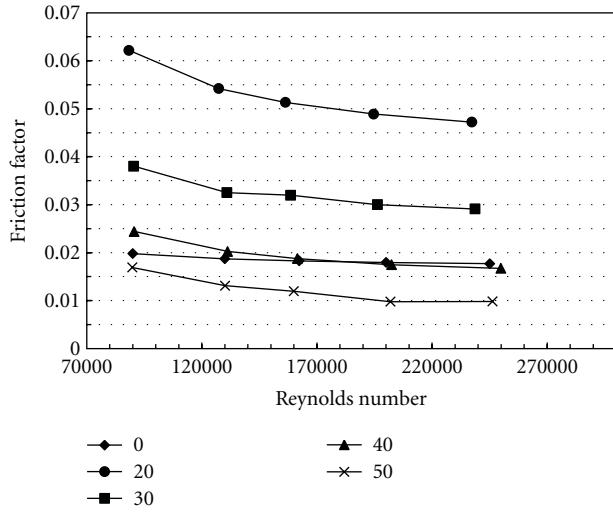


FIGURE 7: Friction factor for helically grooved stators at 4000 rpm versus Re.

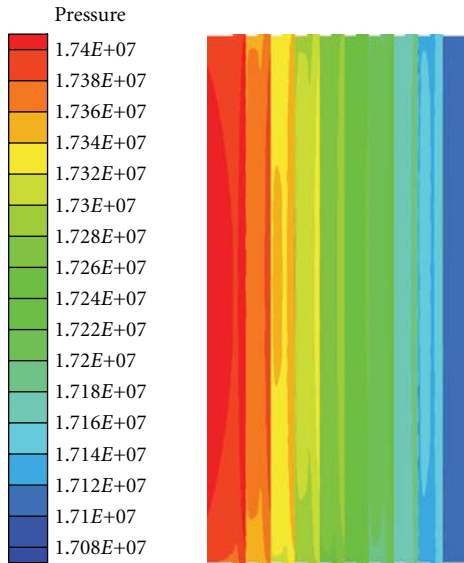


FIGURE 8: Pressure contour of circumferential grooved stator.

50 deg stator is the smallest, and the peak value is the lowest. It is speculated that the difference in friction factor among helically grooved stators is related to the relative location of the highly turbulent kinetic energy region in the groove and the turbulent kinetic energy value range.

#### 4. Conclusions

- (a) The friction factor shows an upward trend with the helix angle reduction, because the seal with a smaller helix angle has less axial component flow and longer groove in favour of energy dissipation. Helically grooved stators with helix angles greater than 20 deg leak increasingly more as the helix angle increases. The circumferentially grooved stator has a lower resistance to leakage than the 20 deg and 30 deg

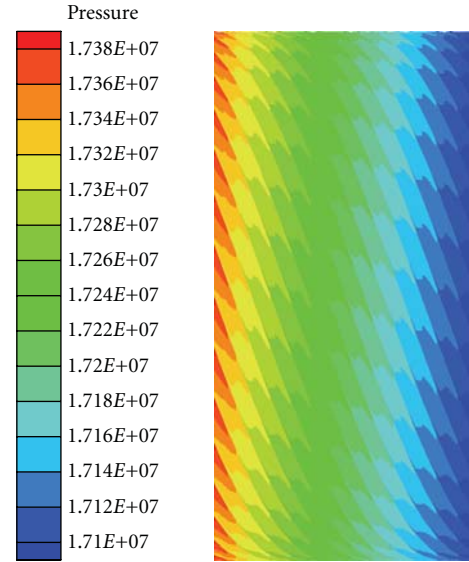


FIGURE 9: Pressure contour of 20 deg stator.

stators, thereby helical groove seal is designed better than the circumferentially grooved seal in reactor coolant pump.

- (b) For all helically grooved stators, the friction factor generally increases with increasing the running speed. The friction factor is more sensitive to the rotational speed especially for the smaller helix angle stator.
- (c) The friction factor generally decreases with axial Reynolds number. At Re lower than 160000, the friction factor drops monotonically with axial Reynolds number. At high Re, for  $\alpha = 30, 40$ , and 50 deg, the friction factor tends to converge to the same value with axial Reynolds number, especially for low rotational speed, and the friction factor increases slightly with axial Reynolds number. The curve tends to get in self-simulated domain with axial Reynolds number higher than 250000.
- (d) At 1750 rpm, 20 deg stator has much higher resistance to leakage than the circumferentially grooved stator; therefore, in reactor coolant pump, the helically-grooved stator with significantly higher power consumption can be used as the axial seal to control backflow leakage along the front surface of the impeller face and reduce the leakage flow rate, while keeping the clearance comparable to that of a plain seal. Because a helical groove yields a backflow along the groove forward inlet, the other object of the application is to remove impurities through the groove path.

Besides, numerical studies are conducted to determine the basic characteristics of the helically grooved stator in high-pressure condition. The conclusions will be summarized for effective application in helical groove seals

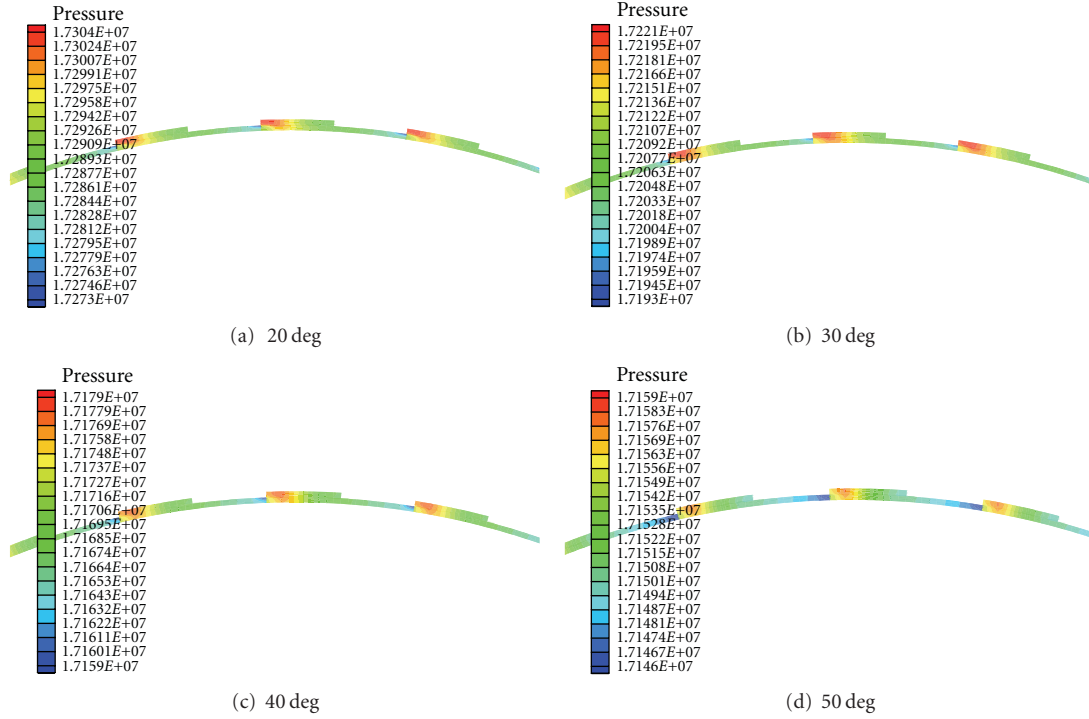


FIGURE 10: Pressure contour of 0.2L cross section for four helix angles.

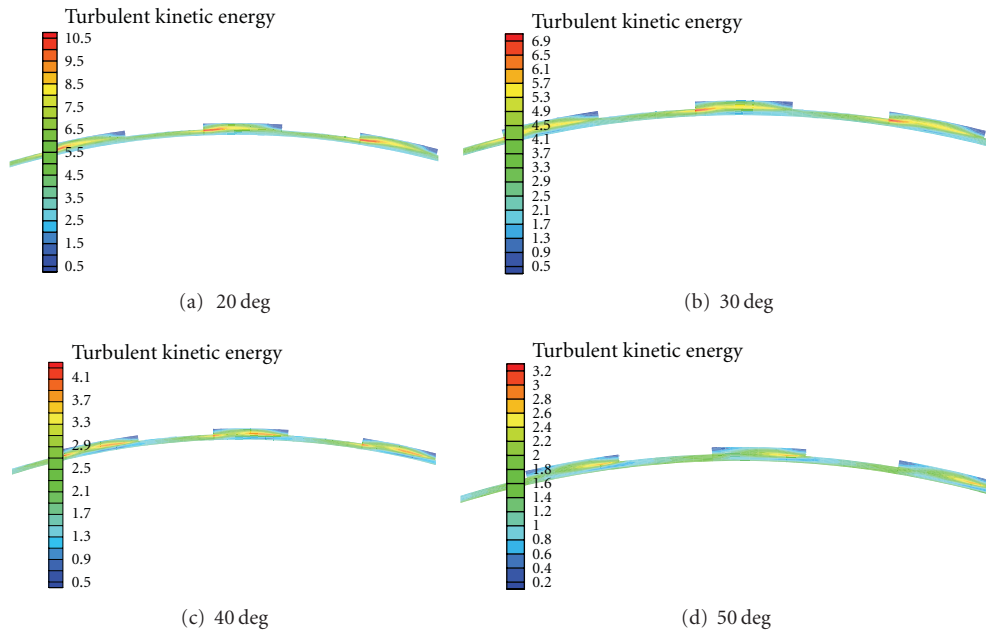


FIGURE 11: Contours of turbulent kinetic energy of 0.2L cross section for four helix angles.

of RCP and contribute future experimental studies on this type of seal.

## Nomenclatures

Re: Axial Reynolds number  
 $\alpha$ : Helix angle (deg)

$\lambda$ : Friction factor  
 $P$ : Static pressure (Pa)  
 $L$ : Seal length (m)  
 $Z$ : Axial seal coordinate (m)  
 $D$ : Hydraulic diameter (m)  
 $\rho$ : Density ( $\text{kg/m}^3$ )  
 $v$ : Average axial velocity (m/s)

$\mu$ :	Dynamic viscosity (Pa·s)
$\kappa$ :	Turbulent kinetic energy ( $\text{m}^2/\text{s}^2$ )
$\varepsilon$ :	Turbulent dissipation rate ( $\text{m}^2/\text{s}^3$ )
$C_\mu$ :	Turbulent viscosity constant
$\kappa$ :	Von Kármán constant
$E$ :	Empirical constant
$U_P$ :	Mean velocity of the fluid at the near-wall node $P$ (m/s)
$k_P$ :	Turbulence kinetic energy at the near-wall node $P$ ( $\text{m}^2/\text{s}^2$ )
$y_P$ :	Distance from point $P$ to the wall (m)
$G_k$ :	Generation of turbulence kinetic energy due to the mean velocity gradients
$G_b$ :	Generation of turbulence kinetic energy due to buoyancy
$Y_M$ :	Contribution of the fluctuating dilatation in compressible turbulence to the overall dissipation rate
$C_{1\varepsilon}, C_{2\varepsilon}, C_{3\varepsilon}$ :	Model constants for $\varepsilon$ equations
$\sigma_k$ :	Turbulent Prandtl number for $k$
$\sigma_\varepsilon$ :	Turbulent Prandtl number for $\varepsilon$
$S_k$ :	User-defined source term for $k$
$S_\varepsilon$ :	User-defined source term for $\varepsilon$ .

## Acknowledgment

The authors appreciate the financial support from the National Basic Research Program of China (973 Program).

## References

- [1] H. Kaburaki and T. Takizuka, "Leakage flow characteristics of highly effective graphite seal mechanism for HTGR core support blocks," *Journal of Nuclear Science and Technology*, vol. 25, no. 1, pp. 92–99, 1988.
- [2] H. Kaburaki and T. Takizuka, "Leakage flow characteristics of seal mechanism for HTGR core support blocks," *Journal of Nuclear Science and Technology*, no. 9, pp. 742–747, 1987.
- [3] J. Bootsma, *Liquid-lubricated spiral-groove bearings [Ph.D. thesis]*, Technological University, Delft, The Netherlands, 1975.
- [4] G. G. Hirs, "A bulk-flow theory for turbulence in lubricant films," *ASME Journal of Lubrication Technology*, vol. 95, no. 2, pp. 137–146, 1973.
- [5] C.-H. Kim and D. W. Childs, "Analysis for rotordynamic coefficients of Helically-Grooved turbulent annular seals," *ASME Journal of Tribology*, vol. 109, no. 1, pp. 136–143, 1987.
- [6] J. A. Walowit, "User's manual for computer code SPIRALG gas lubricated spiral grooved cylindrical and face seals," Tech. Rep. NAS3-25644, 1992.
- [7] T. Iwatsubo, B. C. Sheng, and M. Ono, "Experiment of static and dynamic characteristics of spiral grooved seals, rotordynamic instability problems in high-performance turbomachinery," in *Proceedings of a Workshop NASA CP No. 3122*, pp. 223–234, A&M University, Texas, Tex, USA, 1990.
- [8] K. Kanki and T. Kawakami, "Experimental study on the static and dynamic characteristics of screw Grooved seals," *Rotating Machinery Dynamics*, vol. 1, pp. 273–278, 1987.
- [9] T. Iwatsubo and B. S. Yang R Ibaraki, "Theoretical approach to obtaining dynamic characteristics of noncontacting spiral-Grooved seals, Rotor-dynamic instability problems in high performance turbomachinery," in *Proceedings of a Workshop NASA CP, 2443*, pp. 155–188, A&M University, Texas, Tex, USA, June 1986.
- [10] D. W. Childs, S. A. Nolan, and J. J. Kilgore, "Test results for turbulent annular seals, using smooth rotors and helically grooved stators," *Journal of Tribology*, vol. 112, no. 2, pp. 254–258, 1990.
- [11] D. R. Gowda and B. S. Prabhu, "High-pressure annular seal leakage and rotordynamics with application to turbomachinery," *International Journal of Rotating Machinery*, vol. 8, no. 6, pp. 403–411, 2002.
- [12] ANSYS Inc., *ANSYS FLUENT 12.0 Theory Guide*, ANSYS Inc., Canonsburg, Pa, USA, 2009.
- [13] J. J. Moore and A. B. Palazzolo, "CFD comparison to 3D laser anemometer and rotordynamic force measurements for grooved liquid annular seals," *Journal of Tribology*, vol. 121, no. 2, pp. 306–314, 1999.



## Research Article

# Control of Surge in Centrifugal Compressor by Using a Nozzle Injection System: Universality in Optimal Position of Injection Nozzle

Toshiyuki Hirano,<sup>1</sup> Takanori Uchida,<sup>2</sup> and Hoshio Tsujita<sup>3</sup>

<sup>1</sup> Production Systems Engineering Course, Tokyo Metropolitan College of Industrial Technology, 1-10-40 Higashiohi, Shinagawa-ku, Tokyo 140-0011, Japan

<sup>2</sup> Graduate School of Engineering, Hosei University, 3-7-2 Kajinocho, Koganei-shi, Tokyo 184-8584, Japan

<sup>3</sup> Department of Mechanical Engineering, Faculty of Science and Engineering, Hosei University, Tokyo, Japan

Correspondence should be addressed to Toshiyuki Hirano, hirano@s.metro-cit.ac.jp

Received 20 July 2012; Revised 28 September 2012; Accepted 9 October 2012

Academic Editor: N. Sitaram

Copyright © 2012 Toshiyuki Hirano et al. This is an open access article distributed under the Creative Commons Attribution License, which permits unrestricted use, distribution, and reproduction in any medium, provided the original work is properly cited.

The passive control method for surge and rotating stall in centrifugal compressors by using a nozzle injection system was proposed to extend the stable operating range to the low flow rate. A part of the flow at the scroll outlet of a compressor was recirculated to an injection nozzle installed on the inner wall of the suction pipe of the compressor through the bypass pipe and injected to the impeller inlet. Two types of compressors were tested at the rotational speeds of 50,000 rpm and 60,000 rpm with the parameter of the circumferential position of the injection nozzle. The present experimental results revealed that the optimum circumferential position, which most effectively reduced the flow rate for the surge inception, existed at the opposite side of the tongue of the scroll against the rotational axis and did not depend on the compressor system and the rotational speeds.

## 1. Introduction

In recent years, the global approach to environmental protection has progressed and the measures against the problems such as the exhaust gas of cars and the fossil fuels depletion are urgent tasks. A turbocharger, as a part of the technology dealing with environmental problems, is expected to clean the exhaust gas from automobile engines by improving combustion efficiency, and to contribute to the reduction of fuel consumption through downsizing of engine leading to the weight reduction. Therefore, the application of a turbocharger to various types of vehicle is developing rapidly. Moreover, since the centrifugal compressor, which is a main component of turbocharger, possesses higher pressure ratio in a single stage and consequently contributes to the reduction in size and weight, it is widely used for many kinds of industrial machines as well as turbochargers. Therefore, the extension of the stable operation range and

the improvement of the supercharging characteristics of a centrifugal compressor are required dramatically.

The operation of a centrifugal compressor of turbocharger at a lower flow rate close to the maximum pressure ratio induces instability phenomena such as rotating stall and surge. Especially, the surge may generate enough intense vibration and noise to destroy the whole pipeline system including a compressor. Moreover, it strongly influences the performance characteristics of the compressor. As a result, the stable operation range is inevitably restricted. Therefore, several investigations [1–6] have been carried out to control the inception of instability phenomena for the purpose of the extension of stable operation range of a centrifugal compressor to the lower flow rate.

In the previous studies on the control of surge in a centrifugal compressor, the injection nozzle system was employed, in which a part of the flow in the discharge duct was recirculated to the inlet of the impeller, and controlled

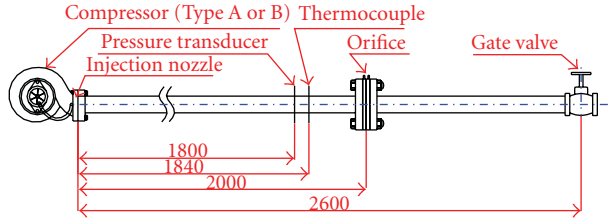


FIGURE 1: Experimental apparatus (unit: mm).

the inceptions of rotating stall and surge [7]. Moreover, optimization of the parameters affecting on the performance of the injection nozzle system such as a position of injection has been performed [8]. Furthermore, the dependency of the optimum injection position on the rotational speed of the impeller has been investigated [9]. However, since these studies have been performed for the same turbocharger system, the universality in the characteristics of the injection nozzle has not been clarified yet.

In this study, the optimum circumferential position of injection nozzle, which most effectively reduced the flow rate for the surge inception, was investigated for two types of compressors at rotational speeds of 50,000 rpm and 60,000 rpm to examine the universality of the optimum circumferential position of injection nozzle. In addition, the influences of the injection on the fluctuating property of the flow field before and after the surge inception were investigated by examining the frequency of static pressure fluctuation on the wall surface.

## 2. Experimental Apparatus

The experimental apparatus used in this study is shown in Figure 1. The configurations and the specifications of centrifugal impellers for two types of centrifugal compressors Type A and Type B are shown in Figure 2 and Table 1, respectively. The outlet blade angle is measured from a radial direction. The compressed air supplied from the screw compressor was used to drive the turbine impeller which revolved the compressor impeller through the corotating axis. A part of the air at the exit of the compressor scroll, which was compressed by the centrifugal impeller and the vaneless diffuser, was recirculated into the injection nozzle installed at the impeller inlet through the bypass pipe. Then, the remaining air was discharged through the delivery duct. The inner diameter of the injection nozzle used in this study is 4 mm. The injection nozzle is installed on the inner wall of the suction pipe of compressor, which is movable in the circumferential direction as shown in Figure 3.

## 3. Experimental Method

The origin of a circumferential position of the injection nozzle indicated by TT(0) is located at the corresponding position to the scroll tongue portion as shown in Figure 4. The circumferential position of the injection nozzle TT has the positive value in the rotational direction of the centrifugal



(a) Type A



(b) Type B

FIGURE 2: Tested impeller (unit: mm).

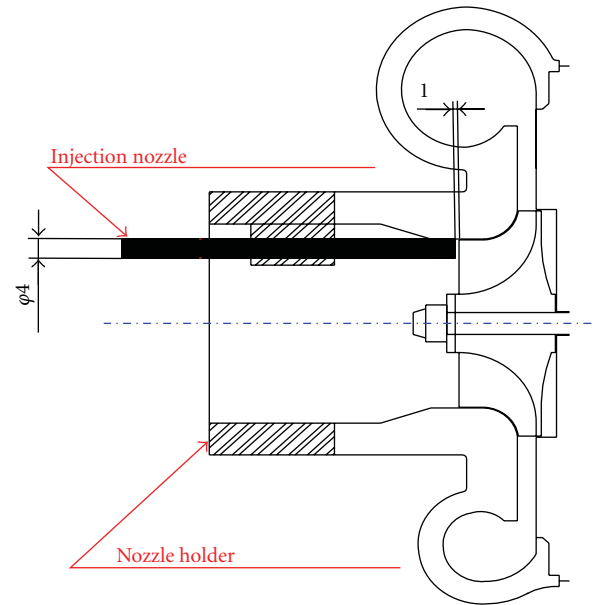
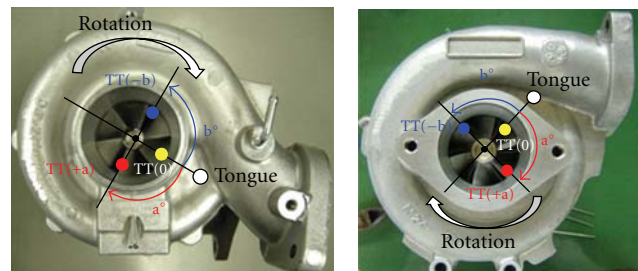


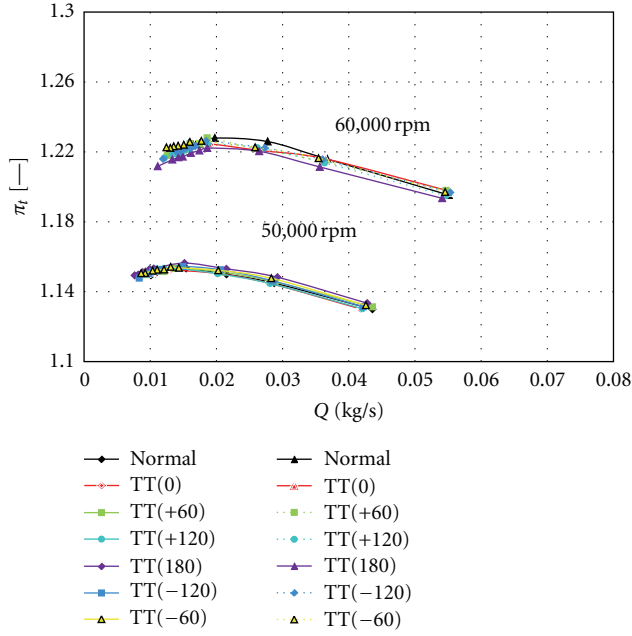
FIGURE 3: Injection nozzle (unit: mm).



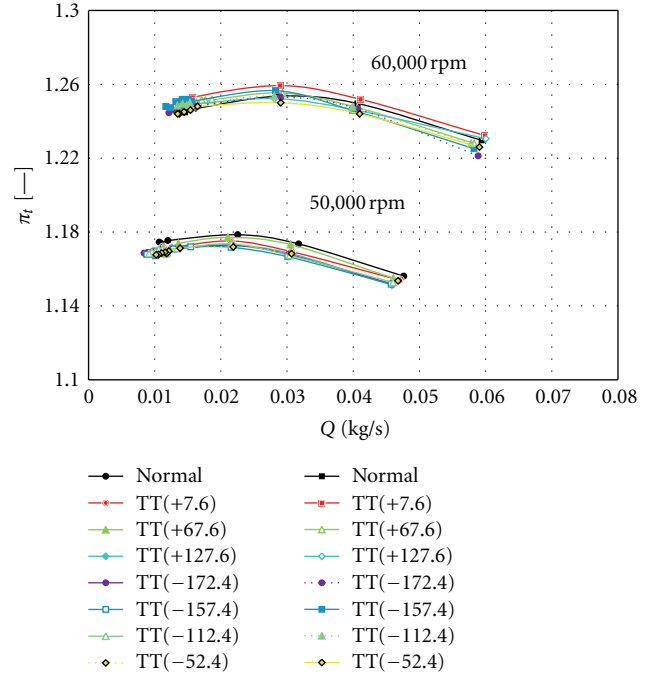
(a) Type A

(b) Type B

FIGURE 4: Definition for position of injection nozzle.



(a) Type A



(b) Type B

FIGURE 5: Performance characteristics.

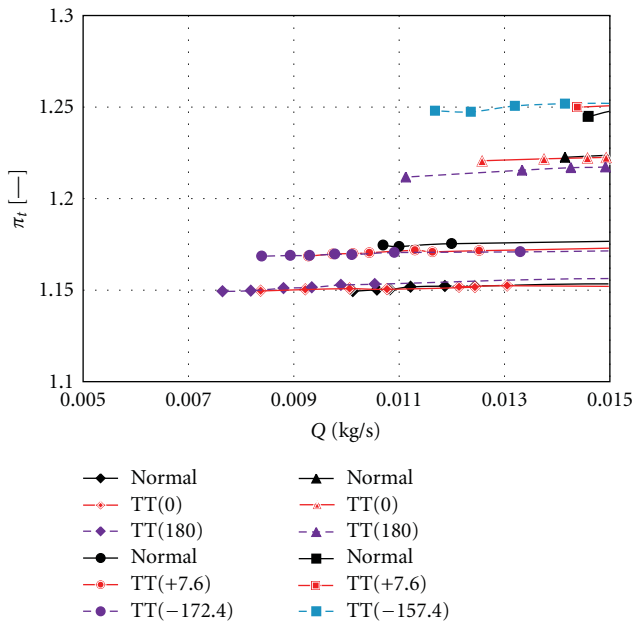


FIGURE 6: Performance characteristics at low flow rate.

impeller. In the following, the case with the injection nozzle is named “Injection,” and that without the injection nozzle is named “Normal.” The performance tests of compressors were performed at the corrected rotational speed of 50,000 rpm and 60,000 rpm. In each experiment, the flow rate was decreased gradually from the full opening condition

by closing the gate valve installed at the downstream side of the delivery duct, until the surge inception. In this study, the preexperiments were performed to relate the degree of the gate valve opening to the flow rate. The limiting flow rate for the surge inception is defined as the flow rate at the degree of valve opening opened by its minimum revolution from that at which a sudden increase of the pressure fluctuation caused by the surge is observed. In this study, the surge inception was detected by the observation of the pressure fluctuation caused by the surge, which was suddenly increased by gradually closing the valve by its minimum revolution. In the experiments for Injection, the experiments were carried out at every 30 degrees of TT from TT(0). Moreover, the experiments for Type B were made at 15-degree intervals around the optimum TT which remarkably reduced the limiting flow rate for surge inception. The exit of the injection nozzle was located at 1 mm upstream of the inlet of the impeller for every experimental condition of Injection. The thermocouples were used to measure the temperature at both the inlet and outlet of the compressor. The static pressure at delivery duct and the pressure difference across the orifice were measured by the pressure transducer. The uncertainty for the measured pressure data is  $\pm 5$  kPa. The corrected flow rate  $Q$  and the pressure ratio  $\pi_t$  were defined by the following equations:

$$Q = Q_0 \frac{P_{a0}}{P_a} \sqrt{\frac{T_1}{T_0}} \text{ [kg/s]}, \quad (1)$$

$$\pi_t = \frac{P_t}{P_a} \text{ [-]}, \quad (2)$$

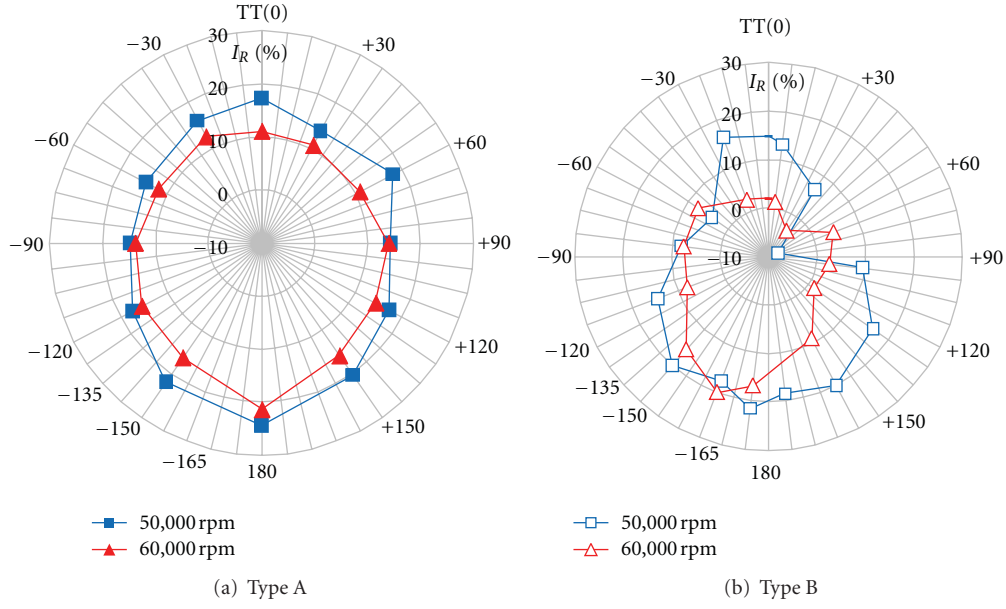


FIGURE 7: Improvement rate of surge margin.

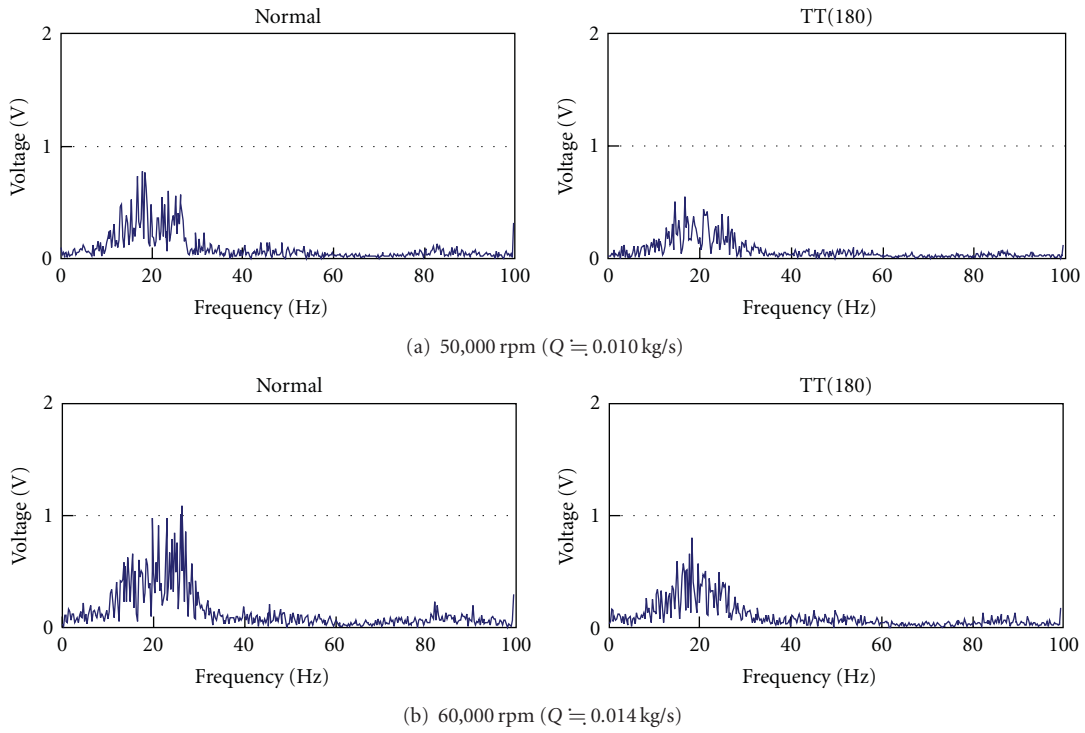


FIGURE 8: Spectrum of pressure fluctuation at delivery duct.

where  $Q_0$  is the measured flow rate,  $P_{a0}$  is the standard atmospheric pressure,  $P_a$  is the measured atmospheric pressure,  $T_1$  is the measured temperature,  $T_0$  is the standard temperature, and  $P_t$  is the measured total pressure at the compressor outlet. In order to investigate the unstable phenomena, the wall static pressure fluctuation was measured at 1800 mm downstream of the compressor exit. The frequency characteristics of the wall static pressure fluctuation were

analyzed by performing FFT. Flow sensor was installed at the bypass pipe to measure the flow rate ejected from the injection nozzle.

#### 4. Results and Discussion

**4.1. Performance Characteristics.** Figure 5 shows the performance characteristics for Normal and Injection of Type

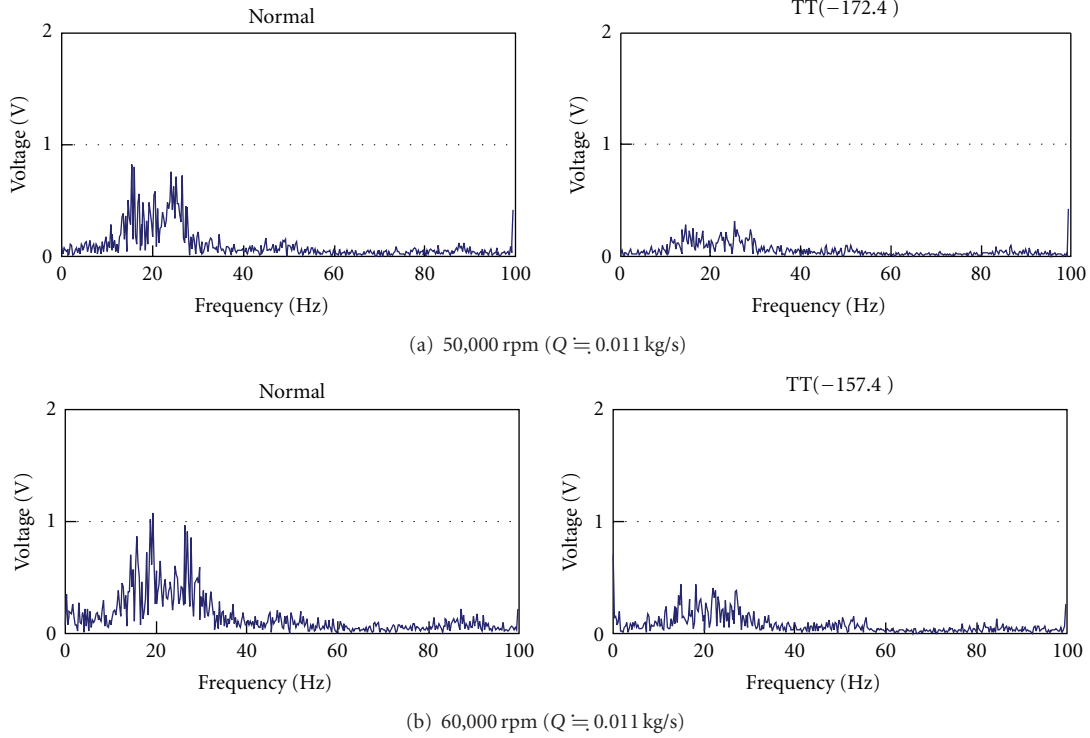


FIGURE 9: Spectrum of pressure fluctuation at delivery duct for Type B.

TABLE 1: Specifications of impeller.

Type of compressor	A	B
Inlet diameter (mm)	43.38	45
Outlet diameter (mm)	56	60
Number of blades	12	12
Outlet blade angle (deg.)	40	60
Inlet blade height (mm)	15.4	14
Outlet blade height (mm)	4.08	5.6
Blade thickness (mm)	0.4	0.675

A and Type B at rotational speeds of 50,000 rpm and 60,000 rpm. Figure 6 shows the performance characteristics at the low flow rate region for TT(0) and TT(180) of Injection, which remarkably reduced the limiting flow rate for surge inception as shown later, with that for Normal.

The performance curves for Injection almost coincide with those for Normal in both Type A and Type B for every rotational speed (Figure 5). Therefore, it is apparent that the influence of the injection system on the performance characteristics of the compressor is negligible. Moreover, the limiting flow rate for surge inception is reduced by using the nozzle injection system as shown in Figure 6. Therefore, the nozzle injection system is recognized to have ability to extend the stable operating range to the lower flow rate region. It is considered that the injection on the inner wall of the suction pipe of the impeller would reduce the reversed flow region distributed on the shroud side wall from the diffuser exit up to the impeller inlet which appeared before the surge

inception and consequently extend the limiting flow rate for surge inception to the lower flow rate region.

**4.2. Optimal Injection Position.** In order to evaluate the effect of injection on the reduction of limiting flow rate for surge inception, the improvement rate of surge margin  $I_R$  was defined by the following equation:

$$I_R = \frac{Q_N - Q_I}{Q_N} \times 100 [\%], \quad (3)$$

where  $Q_N$  and  $Q_I$  mean the limiting flow rate for surge inception in Normal and Injection, respectively. Figure 7 gives the relationship between the injection position TT and the improvement rate  $I_R$ .

The improvement rates  $I_R$  at 50,000 rpm are relatively higher than those at 60,000 rpm in both Type A and Type B. The  $I_R$  in Type A exhibits the improvement rate more than 10% for every TT, and the maximum  $I_R$  more than 20% is achieved especially for TT(180) at each rotational speed (Figure 7(a)). Similar tendency is also observed in Type B (Figure 7(b)), and the maximum improvement rate more than 20% is located around TT(180) at both 50,000 rpm and 60,000 rpm. These results suggest that the optimum circumferential position of the injection nozzle, which produces the maximum improvement ratio, is located around TT(180), which is the opposite side of the tongue of the scroll against the rotational axis, without the dependencies on the compressor type and the rotational speed. In general, the number of stall cell in the diffuser under the rotating stall condition varies from one to two according to the decrease



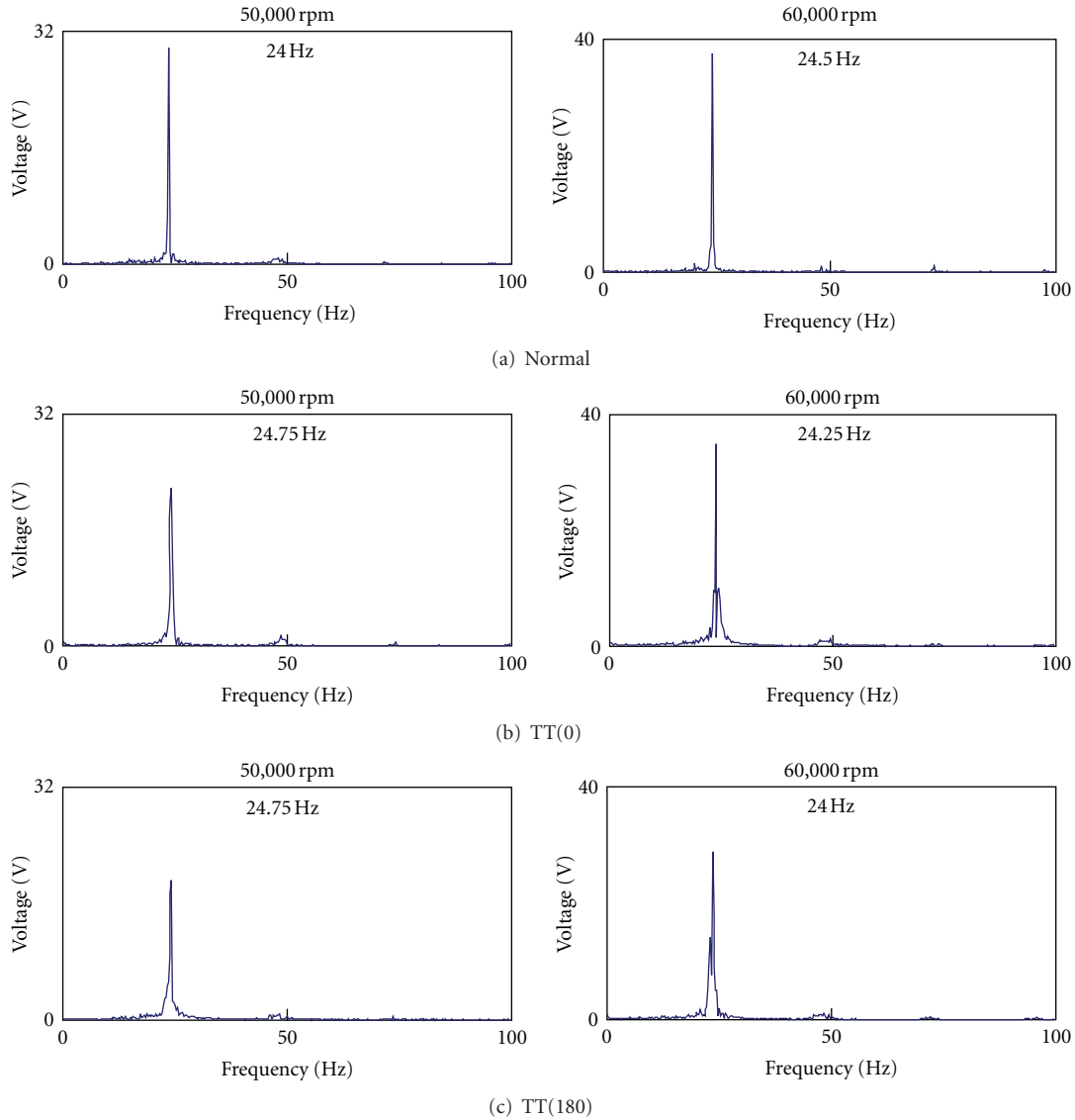


FIGURE 10: Spectrum of pressure fluctuation at delivery duct during surge for Type A.

of the flow rate. Moreover, in the case of the compressor with a scroll, the circumferential distribution of the static pressure on the diffuser endwall becomes nonaxisymmetric and is strongly distorted by the decrease of the flow rate. This distortion of the pressure distribution in the diffuser influences the flow field in the impeller, and consequently on the flow rate for surge inception. Therefore, it is considered that the optimum circumferential position of the injection nozzle has a strong relation with the behavior of the stall cell and the formation of circumferential distribution of the static pressure in the diffuser.

#### 4.3. Frequency Characteristic

(a) *Before Surge Inception.* Figures 8 and 9 show the frequency characteristics of the static pressure fluctuation on the inner wall of the delivery duct at 1800 mm downstream

of the compressor exit for Normal and the optimum TT of Injection in Type A and Type B, respectively. The flow rate in the results shown in Figures 8 and 9 is the nearest one to the limiting flow rate for surge inception for Normal. The peaks of the spectrum of pressure fluctuation for Normal at each rotational speed in Type A and Type B are observed around 15 to 30 Hz. The peaks for the optimum TT of Injection are lower than those in Normal. The surge frequencies in Type A and Type B are about 24.5 Hz and 23.5 Hz, respectively, irrespective of the rotational speed, which are different from the frequencies for the peaks observed in Figures 8 and 9. So, the peaks in Figures 8 and 9 are considered to be associated with the unstable phenomenon such as the rotating stall which appears before the surge inception. Therefore, it is considered that the optimum TT of Injection enhances the improvement rate of surge margin by suppressing the unstable phenomenon appearing before the surge inception.

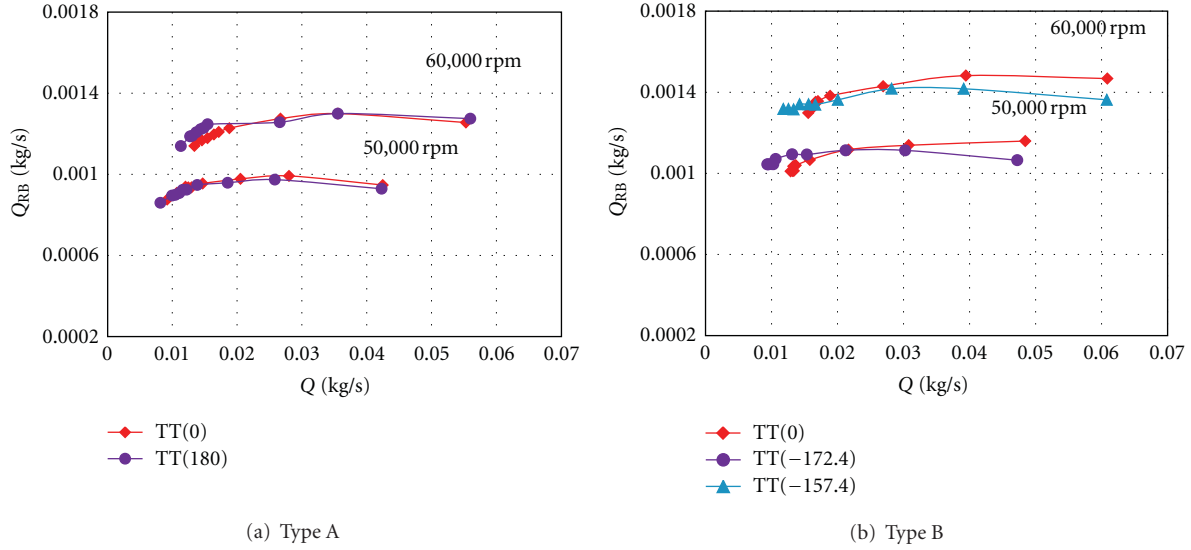


FIGURE 11: Injection mass flow rate.

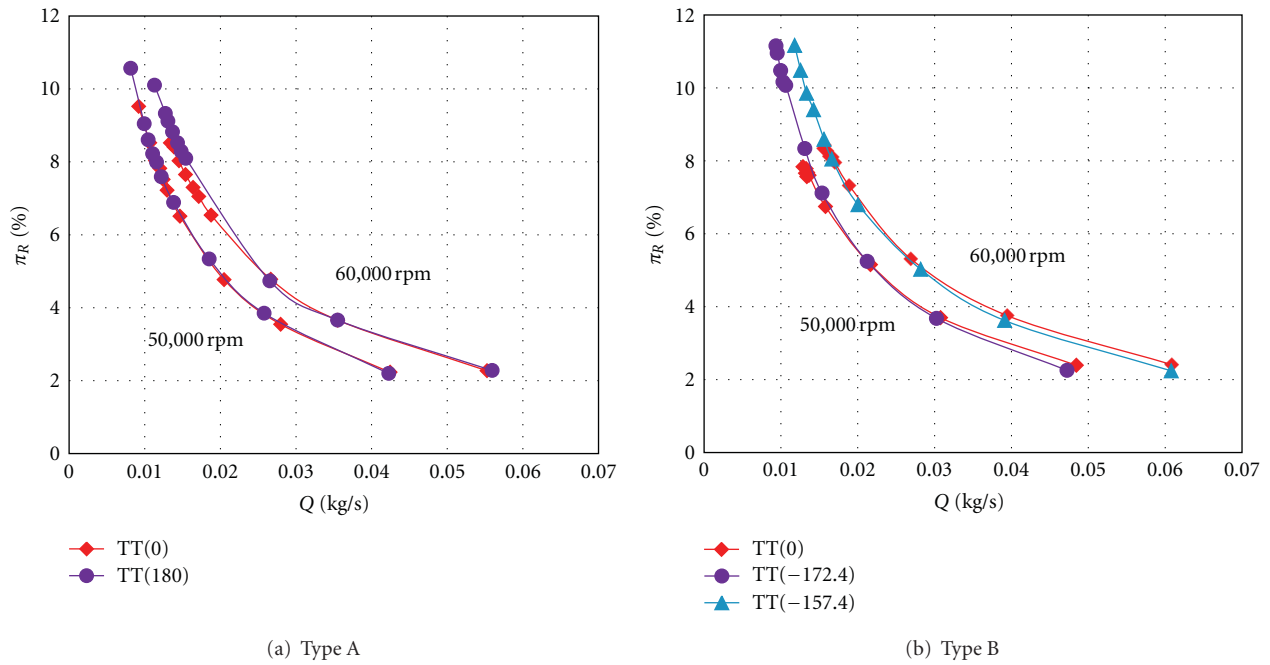


FIGURE 12: Recirculation ratio.

(b) *After Surge Inception.* In order to examine the effects of the injection on the flow field under the surge condition, the frequency characteristics for Normal, TT(0), and the optimum TT(180) of Injection in Type A at  $Q = 0.000$  kg/s after the surge inception are given in Figure 10. “ $Q = 0.000$  kg/s” means the fully closed vane condition.

It is recognized that the peak of spectrum for the surge frequency of Injection becomes less than that of Normal after the surge inception. Moreover, the optimum TT(180) more reduces the peak of spectrum than TT(0). This means that Injection also reduces the strength of the surge, and the optimum circumferential position of

injection for the surge reduction coincides with that for the reduction of the limiting flow rate for the surge inception.

**4.4. Injection Flow Rate.** Figure 11 shows the injection mass flow rate  $Q_{RB}$  for TT(0) and the optimum TT(180) of Injection at 50,000 rpm and 60,000 rpm in Type A and Type B. The injection flow rate in each condition is almost constant over the full operating range, but increased by the increase of the rotational speed. This is caused by the increase of pressure ratio due to the increase of the rotational speed. On the other hand, the injection flow rate is almost

unaffected by the circumferential position of injection TT at each rotational speed.

In order to evaluate the ratio of the injection mass flow rate to the mass flow rate discharged from the delivery duct, the recirculation ratio  $\pi_R$  was defined by the following equation:

$$\pi_R = \frac{Q_{RB}}{Q_N} \times 100 [\%]. \quad (4)$$

Figure 12 shows the recirculation ratio  $\pi_R$  for TT(0) and the optimum TT(180) of Injection at 50,000 rpm and 60,000 rpm in Type A and Type B. The influence of the circumferential position of injection TT on the recirculation ratio  $\pi_R$  is very small. The recirculation ratio is increased by the decrease of the flow rate in every experimental condition. Moreover, the comparison between the rotational speeds indicates that the recirculation ratio  $\pi_R$  is increased by the increase of the rotational speed corresponding to the tendency observed for the injection mass flow rate (Figure 11).

## 5. Conclusion

The following conclusions were obtained by the present study.

- (1) With the nozzle injection system the stable operating range of the compressor improves and that is a direct effect on the performance characteristic.
- (2) The optimum circumferential position of the injection nozzle, which produces the maximum improvement rate, is located around the opposite side of the tongue of the scroll against the rotational axis irrespective of the compressor type and the rotational speed.
- (3) The optimum circumferential position of Injection enhances the improvement rate of surge margin by suppressing the unstable phenomenon appearing before the surge inception.
- (4) The injection flow rate is almost constant over the full operating range, but increased by the increase of the rotational speed.
- (5) The nozzle injection system has also the ability to reduce the strength of the surge.
- (6) The optimum circumferential position of Injection for the surge reduction coincides with that for the reduction of the limiting flow rate for the surge inception.

## References

- [1] A. Suzuki, H. Tsujita, and S. Mizuki, "Passive control of surge for centrifugal compressor by using resonator," in *Proceedings of the 4th International Symposium on Experimental and Computational Aerothermodynamics of Internal Flows*, vol. 2, pp. 226–233, 1999.
- [2] H. Tamaki, X. Zheng, and Y. Zhang, "Experimental investigation of high pressure ratio centrifugal compressor with axisymmetric and non-axisymmetric recirculation device," in *Proceedings of the ASME International Gas Turbine Institute (IGTI '12)*, 2012.
- [3] S. Mizuki, H. Tsujita, and Y. Hishinuma, "Control of surge for centrifugal compression system by using a bouncing ball," ASME Paper 2000-GT-429, 2000.
- [4] F. Willemas and B. De Jager, "One-sided control of surge in a centrifugal compressor system," ASME Paper 2000-GT-527, 2000.
- [5] G. J. Koch, "Experimental investigation of diffuser hub injection to improve centrifugal compressor stability," NASA/TM 2004-213182, 2004.
- [6] H. Chen and V. Lei, "Casing treatment & inlet swirl of centrifugal compressors," in *Proceedings of the ASME International Gas Turbine Institute (IGTI '12)*, 2012.
- [7] R. Gu and M. Yashiro, "Surge control for centrifugal compressor of turbocharger," *JSAE Paper*, vol. 36, no. 2, pp. 83–88, 2005.
- [8] R. Gu, H. Ikeda, A. Yoshida, H. Tsujita, and S. Mizuki, "Effect of air injection on performance characteristics of small centrifugal compressor," in *Proceedings of the Turbomachinery Society of Japan*, May 2007.
- [9] R. Gu, S. Mizuki, and H. Tsujita, "Surge control of centrifugal compressor by inducer tip injection," in *Proceedings of the International Gas Turbine Congress (IGTC '07)*, Tokyo, Japan, 2007.

## Research Article

# Encounters with Vortices in a Turbine Nozzle Passage

J. P. Gostelow,<sup>1</sup> A. Mahallati,<sup>2</sup> W. E. Carscallen,<sup>2</sup> and A. Rona<sup>1</sup>

<sup>1</sup> Department of Engineering, University of Leicester, University Road, Leicester LE1 7RH, UK

<sup>2</sup> National Research Council of Canada, Ottawa, ON, Canada K1A 0R6

Correspondence should be addressed to J. P. Gostelow, jpg7@le.ac.uk

Received 16 July 2012; Accepted 25 September 2012

Academic Editor: Seyed G. Saddoughi

Copyright © 2012 J. P. Gostelow et al. This is an open access article distributed under the Creative Commons Attribution License, which permits unrestricted use, distribution, and reproduction in any medium, provided the original work is properly cited.

Experiments were conducted on the flow through a transonic turbine cascade. Secondary flows and a wide range of vortex types were encountered, including horseshoe vortices, shock-induced passage vortices, and streamwise vortices on the suction surface. In the separation region on the suction surface, a large rollup of passage vorticity occurred. The blunt leading edge gave rise to strong horseshoe vortices and secondary flows. The suction surface had a strong convex curvature over the forward portion and was quite flat further downstream. Surface flow visualization was performed and this convex surface displayed coherent streamwise vorticity. At subsonic speeds, strong von Kármán vortex shedding resulted in a substantial base pressure deficit. For these conditions, time-resolved measurements were made of the Eckert-Weise energy separation in the blade wake. At transonic speeds, exotic shedding modes were observed. These phenomena all occurred in experiments on the flow around one particular turbine nozzle vane in a linear cascade.

## 1. Introduction

Leonardo da Vinci (1452–1519) was a notable early observer of vortices produced by a solid object placed in a stream of flow (Figure 1). When the object has thickness and produces a flow turning of 70° or more, the generation of strong vorticity is to be expected and the subject turbine nozzle blading is no exception. The different vortical phenomena arising in the flow passage are described in this paper. The variety of the vortical forms and occurrences is surprising.

The encounters with vortices involve the flows outlined in the paper, starting at the leading edge. These are horseshoe vortices, passage vortices with attendant secondary flows, and on the suction surface, streamwise vortices. At the trailing edge, vortex shedding, energy separation, base pressures, and exotic shedding modes are observed. This is all in experiments on the flow around one particular turbine nozzle vane in a linear cascade. This diversity of vortex phenomena illustrates the challenge of describing the fundamental internal aerodynamics of turbomachinery blading. Greater physical understanding is required of these phenomena, including vortex structures on surfaces, vortex shedding, the base region, the vortex wake, and its interaction with the shock waves.

Surface flow visualization was performed on the suction surface of the turbine blade at subsonic and transonic speeds. This was effective in providing a time-average mapping of streamwise vortical structures within the blade passage. Under the influence of the strong favorable pressure gradients on the suction surface, the vortices were remarkably persistent, lasting to the trailing edge.

Previous investigators have observed streamwise vortices and “streaky structures” on flat plates and on the suction surface of compressor blades. Turbine blade designers are quite familiar with the phenomenon of Görtler vorticity; this is commonly thought to occur predominantly on the concave pressure surfaces of turbine blades. An organized streamwise vortex system tends to increase heat transfer to the blade surface and also makes flow and heat transfer difficult to predict. Designers generally assume that streamwise vorticity of this kind is confined to the concave pressure surfaces. Examples will be given which should result in a questioning of the assumption that the organized streamwise vorticity is confined to the pressure surface of a turbine blade.

Although it appears to be unusual, this behavior had been predicted and observed previously with attendant theories for wavelength. For a predominantly convex surface, the behavior is consistent with the later predictions of



FIGURE 1: Observations of vortices by Leonardo da Vinci.

Görtler [1], who postulated instability on a convex surface from the concave streamlines ahead of the leading edge stagnation region. Measurements of spanwise wavelength of the periodic array of vortices are found to be compatible with the subsequent predictions of Kestin and Wood [2].

In the mid nineteen-seventies, a National Research Council/Pratt and Whitney, Canada collaborative program was established to produce a gas generator with a turbine stage of aggressive design. The turbine was highly loaded, giving a low wheel speed. This was supported by a highly loaded turbine test facility that was of three times PT6 engine size and matched the engine Mach and Reynolds' numbers. The turbine nozzle had a thick trailing edge to allow for cooling passages [3].

The stage employed a high turning transonic nozzle and was tested over a range of exit Mach numbers between 0.67 and 1.2. During testing, this turbine stage gave some inexplicable results that showed a redistribution of the downstream total temperature field. In this ostensibly adiabatic arrangement, the central regions of the vane wakes exhibited a significant decrease in total temperature and their edges showed an unexpected increase.

To resolve these anomalies and obtain detailed information over the Mach number range, the midspan section of the nozzle was tested in a large scale, low aspect ratio, and transonic planar cascade [4]. Some details of the blading are given in Figure 2. At high subsonic speeds, acoustically coupled vortex shedding created energy redistribution in the wake. This was measured using wide bandwidth temperature probes. In the first time-resolved measurements of wake temperature redistribution, by Carscallen et al. [5], the vortex shedding was shown to give rise to an effect first noted

- 6 airfoils (5 passages)
- Midspan of an HPT vane
- 4.3 times engine size
- Correct engine  $Re$  of  $2.13 \times 10^5$
- Correct engine  $Ma$  of 1.16 at a PR of 2.3
- Stagger angle  $64^\circ$
- Solidity 1.19



FIGURE 2: Some features of the blading.

by Eckert and Weise [6]. This had led to problems in the development of an advanced turbine stage.

Base pressures are also associated with vortex shedding and result in increased drag for bluff bodies and turbine blades. Time-resolved pressure distributions gave information on fluctuations and corresponding base drag coefficients.

The most common shedding mode is not the only mode. Not all vortex shedding takes the form of the classical vortex street described by von Kármán; a wide range of "exotic" modes also exists. The discovery of these anomalous patterns behind transonic turbine blades was first reported to ISROMAC-5 by Carscallen and Gostelow [7] and resulted in an investigation of when they might occur. Two other applications were found, in the vortex-induced vibration of bluff bodies and research on oscillating airfoils. Findings from the vortex-induced vibration work of Williamson and Roshko [8] have clarified the shedding modes.

## 2. Vortices in the Blade Passage

The inlet wall boundary layer occupies 10% of the span and the leading edge was thick and blunt, giving rise to strong horseshoe vortices and secondary flows. The secondary flow creates a large displacement which affects the streamlines well outside the secondary flow zones. When applied to the flow in a cascade, the term "secondary flow" is restricted to the differential deflection imparted by the cascade, to a sheared free stream. In this case, the principal source of shear at inlet is the wall boundary layer.

At the midspan, the surface streamlines are all parallel and the flow appears to be two dimensional. At Mach 1.16 the shock impingement and separation region is associated with a strong vortex rollup where the shock impingement meets the side-wall boundary layer. This is associated with the passage vortex.

Two other vortex types should be mentioned. These are the relatively small contrarotating corner vortex and the rather larger wall vortex that is induced by the passage vortex.

A narrow, but vigorous, "corner vortex" exists beneath the larger multivortex structure [9]. Its induced sense of rotation is contrary to that of the passage vortex. This thin



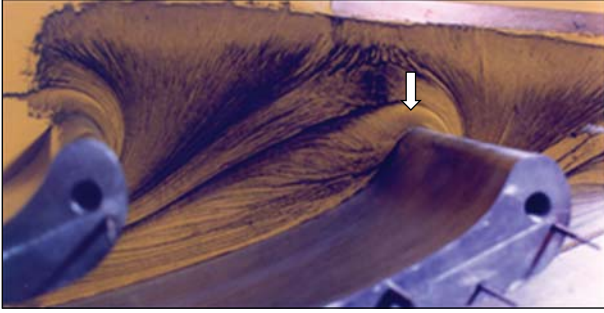


FIGURE 3: Endwall visualization of horseshoe vortex.

vortex occupies the corners between endwalls and blade surfaces and can be seen adjoining the concave blade surface in Figure 3. A rather larger contrarotating vortex, adjoining the endwall, is induced by the impingement of the main passage vortex on the blade's suction surface. This "wall vortex" tends to scrub the endwall in the downstream mid-passage region. It moves away from the suction surface toward the mid-passage region, between the suction and the pressure surfaces.

**2.1. Horseshoe Vortices.** Surface flow visualization was applied, with the aim of establishing the strength of the leading edge horseshoe vortex. This demonstrated that, on the endwalls, the influence of the horseshoe vortex was very strong, as shown in Figure 3. The principal horseshoe vortex around the leading edge had both pressure surface and suction surface components. The pressure surface leg was swept over toward the suction surface, eventually to become the main passage vortex. The static pressure gradient acting on this vortex leg is the same at the endwall as that in the free stream, but the velocity is lower in the end region. The radius of curvature of the streamlines in the end-wall region must also be lower to preserve radial equilibrium. The path the vortex takes in the end-wall region therefore has high curvature and this accounts for its rapid movement across the passage.

**2.2. Passage Vortices.** A qualitative measure of vortex structure, on a time-averaged basis, was obtained using surface oil flow visualization [10]. The blade was covered with a sheet of self-adhesive white vinyl. A mixture of artist-grade linseed oil and powdered lampblack-shaded pigment was applied in a very thin and uniform layer over the suction surface. After letting the tunnel run for about five minutes, the blade was removed and photographed.

Inside the primary passage vortex, the mean pressure fluctuations and the resolved kinetic energy levels are large. The maximum shear levels are observed beneath the main passage vortex and close to the small corner vortices. The visualization of the suction surface flow at  $M_e = 1.16$  is shown in Figure 4. The large numbers on the scale represent percentage axial chord and the small numbers mark static tap locations. The shock impingement and separation region is around the 70% axial chord location.

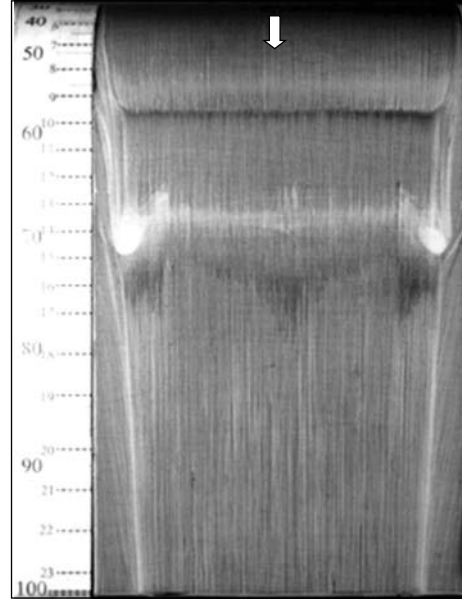
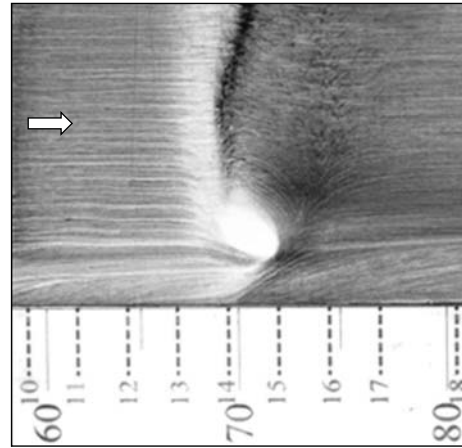
FIGURE 4: Visualization of suction surface at  $M_e = 1.16$ .

FIGURE 5: Enlarged view of the vortex on the suction surface.

There was a strong vortex rollup where the impinging shock met the end-wall boundary layer. The sense of rotation and the direction of the backflow into the separated region following the shock can be deduced. Rotation was counter-clockwise on the left-hand side and clockwise on the right-hand side of the vane.

A close-up view of the vortex formed in the vicinity of the impinging shock and of the resulting separation region is given in Figure 5. The sense of rotation and of the resulting backflow into the separated region following the shock is shown clearly. Fine scale streamwise vortices also show up in Figure 5. For a predominantly convex surface, this behavior was unexpected. At the leading edge, the suction surface is virtually circular; subsequently, much of the suction surface retains a strong convex curvature over the forward portion and is quite flat further downstream. Surface flow visualization was performed at subsonic and transonic speeds, and

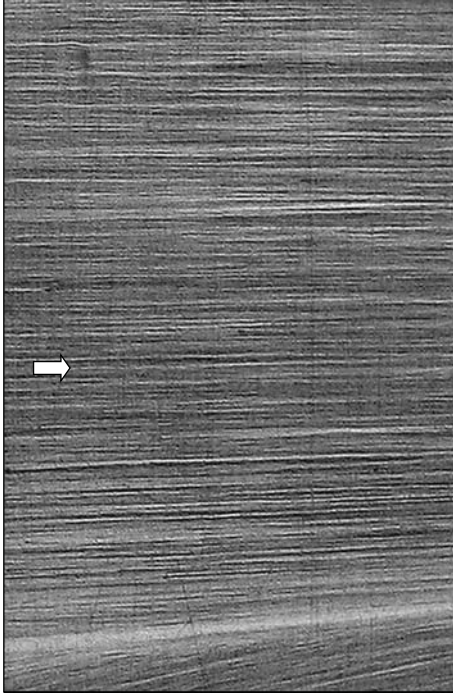


FIGURE 6: Close-up visualization of streamwise vortices.

the surface displayed coherent streamwise vorticity covering the entire surface to the trailing edge.

**2.3. Streamwise Vortices.** Surface flow visualization was performed at subsonic and transonic speeds, and the suction surface displayed coherent streamwise vorticity extending to the trailing edge. A close-up view of the visualization from a discharge Mach number of 1.16 is given in Figure 6. A region between about 80% and 95% axial chord is presented. Fine scale streamwise vortices show up clearly in the figure. For a predominantly convex surface, this behavior is unexpected but is in agreement with the later predictions of Görtler [1], who postulated instability on a convex surface from the concave streamlines ahead of the leading edge stagnation region.

The measurements of the spanwise wavelength of the array of vortices may be compared with the predictions of Kestin and Wood [2]. They predicted a theoretical value of spanwise wavelength between pairs,  $\lambda$ , for a cylinder of diameter,  $D$ , given by

$$\lambda = 1.79\pi D Re^{-0.5}. \quad (1)$$

This is represented by the straight line for  $Tu = 0\%$  in Figure 7. It is difficult to locate the turbine blade on the Kestin and Wood graph as (1) represents flow past a circular cylinder. The leading edge of the turbine blade is relatively blunt but nevertheless has a high surface curvature which decreases rapidly to near zero further back.

The rapid changes in curvature of the convex surface raise the question of what effective diameter should be applied if comparing with the Kestin and Wood model.

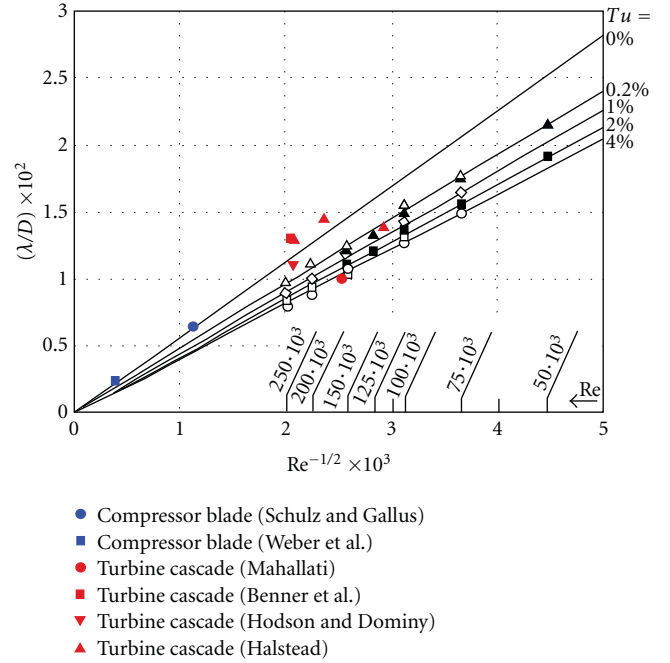


FIGURE 7: Measurements of lateral spacing and comparison with Kestin and Wood's predictions.

According to the Kestin and Wood theory, the measured wavelength, of 0.55 mm, is compatible with the curvature of the suction surface at approximately the 10% true chord location (Figure 7). Because the geometry is quite different from that of a circular cylinder, only qualitative agreement with the predictions can be expected and that is what was achieved. However, surface flow visualization photographs have been analyzed from the work of a number of published experiments. When examined in the same way as the results of Figure 6, two results from compressor blading [11, 12] and three from turbine blading [13–15] are available and also give reasonable agreement with the theory and experiments of Kestin and Wood (Figure 7). The free-stream turbulence levels for the above cases were all in the range  $0.2\% \leq Tu \leq 1.2\%$ . The black symbols are the results from the original experiments of Kestin and Wood over a turbulence level range  $0.2\% \leq Tu \leq 4.0\%$ .

For the subject blading, the acceleration through the passage is strong. The mass-averaged inlet Mach number at the design condition is 0.118 whilst the discharge Mach number is 1.16, giving an order of magnitude difference. It is the flow in the vicinity of the leading edge that determines the susceptibility of the flow to organized streamwise vorticity, and at a local Mach number of 0.118, the flow dynamics should not be very different from previous observations that were undertaken in low speed flows.

In assessing the results, it should be borne in mind that the Mach number regime and the model geometry differ from others considered in the published literature. The blades have a very blunt leading edge and are therefore likely candidates to experience flow instability upstream of the stagnation point and the consequent streamwise

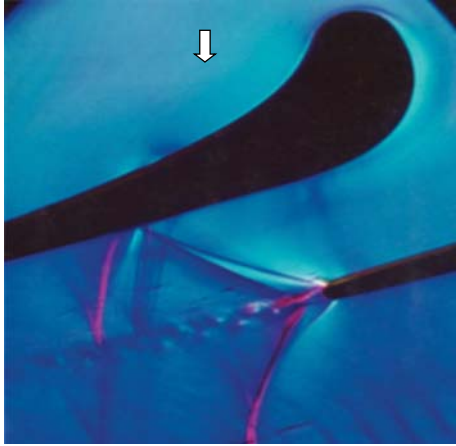


FIGURE 8: Schlieren view of vortex shedding at  $M_e = 1.16$ .

vorticity. Crossflow instabilities have been observed experimentally on the stagnation streamline and are the subject of ongoing computational investigation. Streamline curvature instabilities provide a competing source; the streamlines appear to impact at around 10% chord. An outcome of these investigations is to establish that organized streamwise vorticity may occur more frequently on convex surfaces, such as turbine blade suction surfaces, than was previously appreciated. Investigations and predictions of flow behavior should be extended to encompass this possibility. If this behavior is at all common, it could have implications for turbine aerodynamic and blade cooling design.

### 3. Vortex Shedding

Turbomachinery blades with thick trailing edges, such as those investigated by Carscallen et al. [16], are associated with a high loss penalty. This loss penalty is greater than would be expected from a simple backwards-facing step and remained unexplained until high speed schlieren photography was applied to cascades [17].

Vortex shedding is present in the wakes of blades with thick trailing edges (Figure 8), and the unexplained losses are clearly associated with the shedding process. Among other problems, this drastically increases the base drag at subsonic speeds. In addition to the loss penalty, vortex shedding may cause adverse effects including high frequency sound propagation, vibration effects, locally high heat transfer to or from the blade surface, and energy separation into hot and cold regions. The vortex street, often with closely coupled oscillating shock waves, jeopardizes RANS flow field computations.

With modern CFD approaches these difficulties can be overcome. Two-dimensional time-accurate numerical simulations of the midspan flow were performed by Mahallati over the speed range, using a commercial CFD code. The Roe flux difference-splitting scheme was used for discretization of spatial derivatives. Temporal terms were treated with the second-order implicit method. The  $k-\omega$  turbulence model was used for closure. Convergence was accelerated using multigrid techniques and the mesh was refined such that

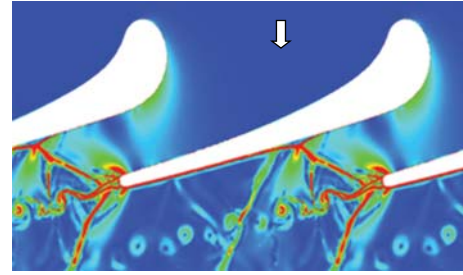


FIGURE 9: Instantaneous CFD view of vortex shedding/shock wave interaction at  $M_e = 1.16$ .

the minimum value of  $y^+$  was less than unity. No wall functions were therefore needed and the turbulence model was integrated all the way to the wall. An instantaneous view from an unsteady RANS calculation for the cascade investigated is given in Figure 9. The interactions between shed vortices and oscillating shock waves are quite complex but have been handled well by the code. Time-averaged experimental results for the blade Mach number distribution and computational predictions are given, with the blade layout, in Figure 10. The agreement between computation and experiment is seen to be reasonable.

**3.1. Base Pressures.** Another detrimental flow phenomenon affected by vortex shedding in turbomachinery is base pressure. It has long been realized that turbomachinery blades with thick trailing edges have an area of reduced static pressure around the trailing edge that creates a considerable increase in base drag at subsonic speeds and reduces the stage efficiency. Cicatelli and Sieverding [18] conducted an investigation on the effect of vortex shedding on the base region flow. They found that the pressure in this region fluctuated by as much as 8% of the downstream dynamic head near separation and by 4.8% in the base region.

It is clear that the instantaneous base pressure could be significantly different from the time-averaged value. Computations for blading designed using steady-state methods will be erroneous for much of the vortex shedding cycle.

At subsonic speeds strong suction at the trailing edge is an essential facet of the vortex shedding process that results in increased drag for bluff bodies and turbine blades. The pressure distribution around a cylinder depends strongly on the Mach number. Time-resolved pressure distributions give information on fluctuations and corresponding drag coefficients. Base pressures were measured at the extreme trailing edge of the blades.

The values obtained are plotted in Figure 11 and the base pressure deficit is seen to reach a maximum at a discharge Mach number of 0.9. The results are supplemented by earlier results obtained by Carscallen et al. [16]. The results exhibit scatter due to unsteadiness but are basically quite similar.

Base pressure is an important contributor to the turbine stage total loss. Work by Denton [19] and by Mee et al. [20] showed the base pressure contributing a significant proportion of the total loss at high speeds. Carscallen et al. [16] found that the lowest base pressure was accompanied

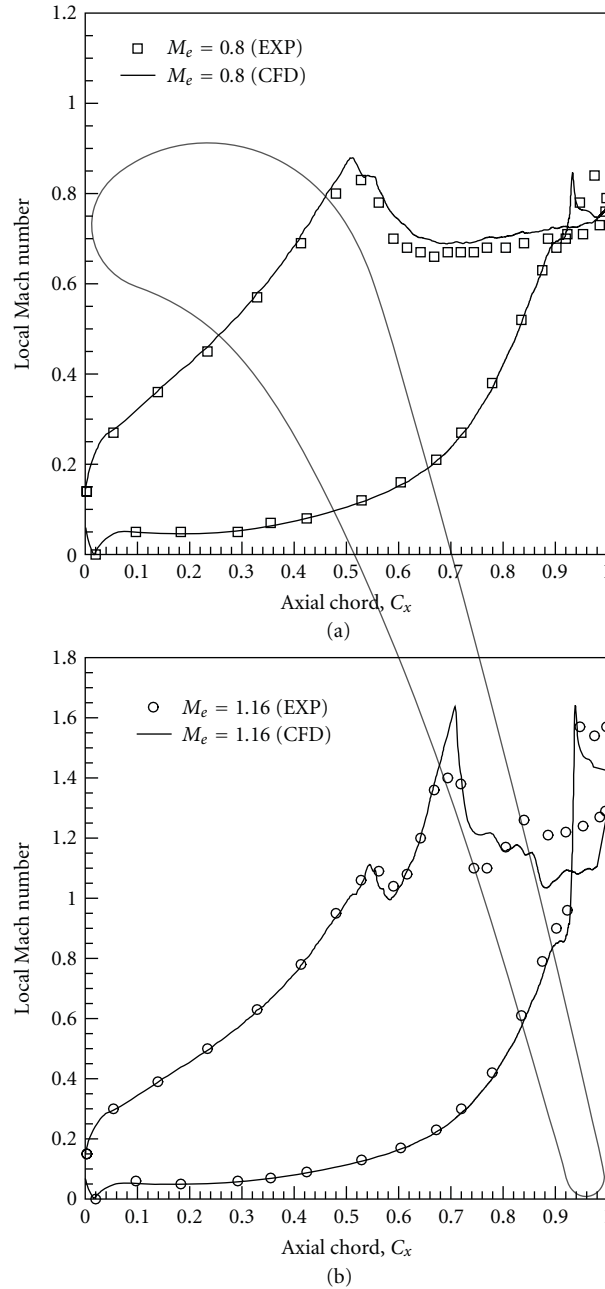


FIGURE 10: Experimental and inviscid CFD isentropic Mach number distribution for exit Mach 0.8 and 1.16.

by the strongest vortex shedding. The most comprehensive base pressure correlation is that of Sieverding et al. [21]. The present results are compared with that correlation in Gostelow et al. [10]. As indicated in Figure 12, the base pressure deficit is underpredicted by the Sieverding correlation. This may result from differing blade trailing edge geometries.

**3.2. Energy Separation.** Associated with the vortex shedding was a thermoacoustic effect that was particularly strong at high subsonic speeds. On a time-averaged basis, the stagnation temperature on the wake center line was found to

be  $12^{\circ}\text{C}$  lower than that for the incoming fluid. Meanwhile the stagnation temperature at the edges of the wake was  $5^{\circ}\text{C}$  higher than that of the incoming fluid. This effect had created a major impediment to the development of a new highly loaded turbine design. Carscallen et al. [5] had demonstrated that this was a manifestation of the Eckert-Weise effect. In this thermoacoustic phenomenon, the vortex cores emerge colder than the surrounding fluid and are associated with hot spots at the edge of the wake.

On a time-averaged basis, this results in substantial total temperature redistribution. Investigation of this phenomenon involved measuring time-resolved temperature variations within the fluctuating wake and relating these



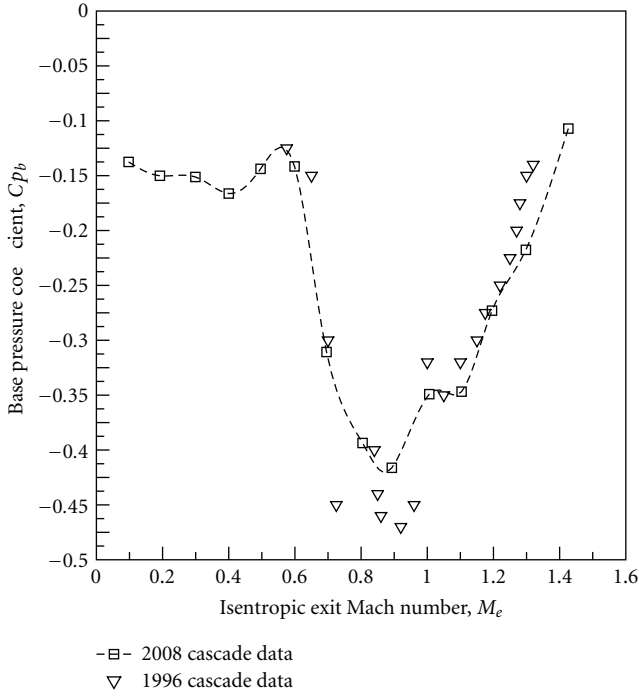


FIGURE 11: Base pressure as a function of discharge Mach number from two test series.

to the previously observed time-averaged stagnation temperature variations. Hitherto attempts to obtain such time-resolved measurements had been frustrated by the inadequate bandwidth of the available temperature measurement instrumentation. Using innovative wide bandwidth temperature probes from Oxford University [22], the anticipated temperature fluctuations were detected and were of the order of 30 K. This is what had been making it difficult to accurately establish the performance of the vane row. In the light of possible turbine efficiency implications of a few percent, it is important to be able to measure, average, and model such flows accurately.

The frequency of vortex shedding from the blades was of the order of 10 kHz and there was a requirement to make total temperature measurements with a bandwidth approaching 100 kHz for energy separation to be resolved and identified. This was achieved using the quartz rod mounted thin film gages supplied by Oxford University. A Kulite pressure transducer was mounted alongside the quartz rods, enabling total pressure to be measured simultaneously. It was therefore possible, using phase averaging, to construct contours of total pressure, total temperature, and entropy increase at the measurement location in the vortex wake. As an example, the total temperature contours are shown in Figure 13 and the entropy contours in Figure 14. The relatively cool vortex structures on the wake center line are seen, as are the hot spots on the edge of the vortex wake. When time averaging is performed, the total temperatures are consistent with those measured using a slow response thermocouple, as shown in Figure 15. These wide-bandwidth measurements represent

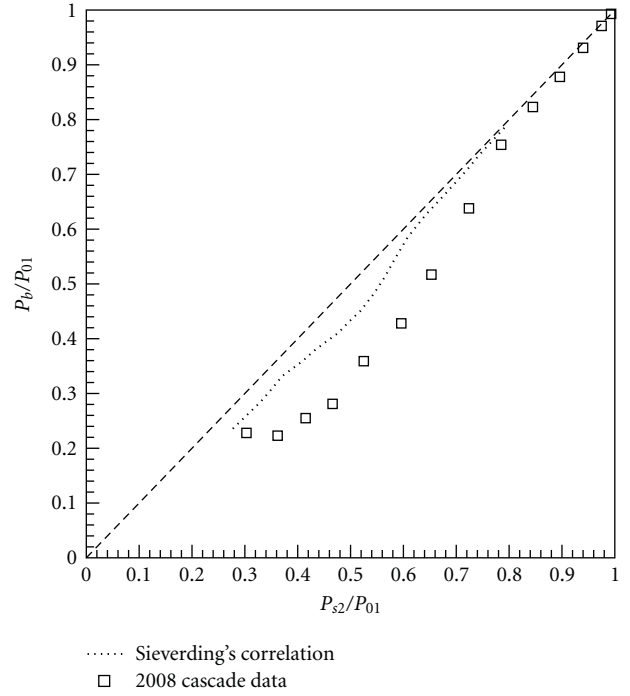


FIGURE 12: Measured base pressure coefficients compared with the Sieverding correlation.

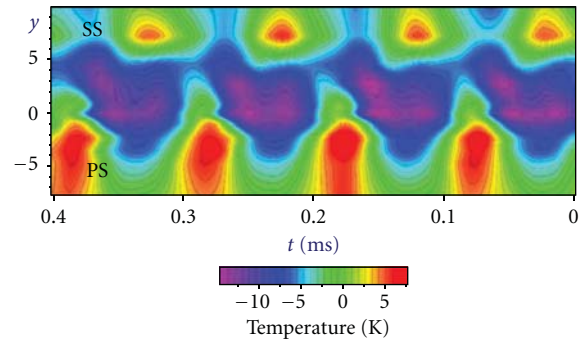


FIGURE 13: Time-resolved total temperature measurements in wake.

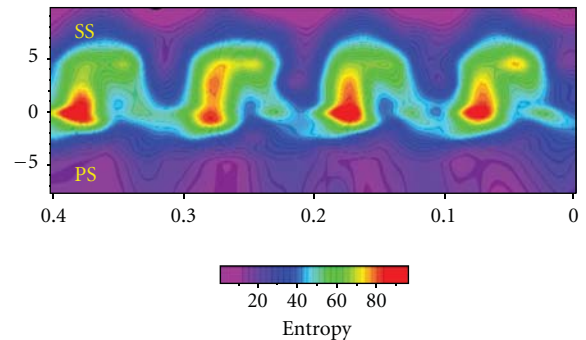


FIGURE 14: Time-resolved measurements of entropy increase.



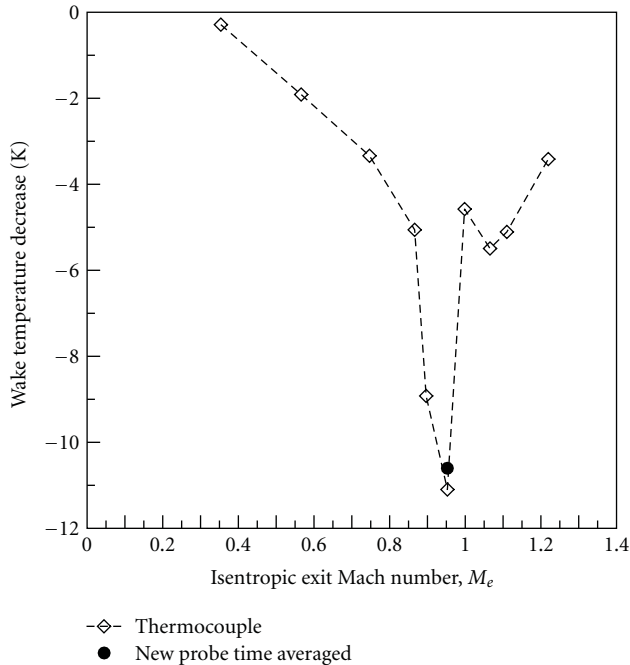


FIGURE 15: Comparison of original thermocouple measurements and time-average of new probe.

the first time-resolved confirmation of the energy separation phenomenon.

A wide range of energy separation phenomena had been reviewed by Eckert, who concluded that energy separation was primarily caused by pressure forces acting on the fluctuating curved streamlines with only a minor contribution from viscous forces. Acoustic effects tend to be a significant ingredient of energy separation.

Because similar temperature redistributions were observed in planar and annular cascades, the vortex shedding effects described in this paper are equally applicable to annular cascades. The effects described are also likely to be present in rotating machines.

**3.3. Exotic Shedding Modes.** The most common vortex shedding mode, predicted by von Kármán, is not the only shedding mode. Not all vortex shedding takes the form of a classical vortex street; a wide range of “exotic” shedding modes exists. Carscallen and Gostelow [7] discovered these anomalous patterns in the wakes of the NRC turbine cascade, prompting an investigation of when they might occur. Two other applications were found, in the vortex-induced vibrations of bluff bodies and in research on oscillating airfoils. Findings from the vortex-induced vibration work of Williamson and Roshko [8] and others clarified the shedding modes. Broadly corresponding designations from the field of vortex-induced vibration were identified in terms of the 2S, 2P, 2P\*, and P + S definitions.

The notation adopted in studies of vortex-induced vibration is that the S mode consists of single vortices shedding each cycle and P indicates that vortices are shed in pairs. P + S means a pattern in which a vortex pair

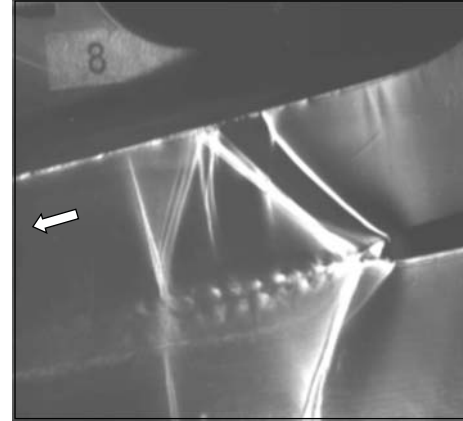


FIGURE 16: Schlieren view of vortex couples.

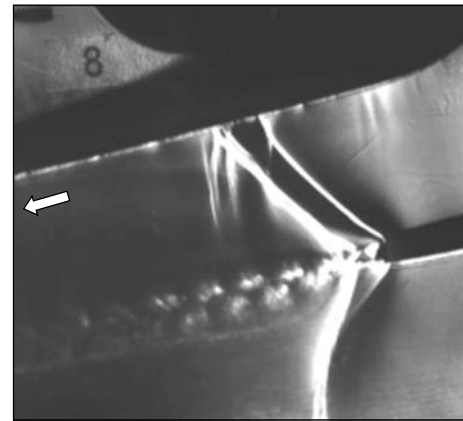


FIGURE 17: Schlieren view of vortex doublets.

and a single vortex are shed each cycle. The conventional von Kármán vortex street is represented by 2S. 2P implies the formation of vortex pairs and the P + S mode is an asymmetric version of the 2P mode in which a pair and a single vortex are shed each cycle. Regions marked P and 2P\* refer to vortex modes described as “single pair” and “double pair”, respectively. Mode P is a wake comprising a set of vortex pairs convecting downstream but also laterally to one side, taking on the appearance of a jet rather than a wake. Mode 2P\* is similar to 2P except that the vortex pairs in one of the half cycles convect away from the front of the body. In this case the convection of each pair is in the downstream direction, creating a jet.

In the experiments on the turbine blades, for some of the time, vortices were shed simultaneously from the two sides of the wake, rather than alternately. This behavior can be observed in Figure 16 for the discharge Mach number of 1.09. Other modes were observed, in which vortex pairing appeared to be taking place on one side only, as in Figure 17. Since the passage shock behavior is determined by the vortex shedding mode, this anomalous behavior could have consequences for predicting shock position blade loading and dynamics. None of these additional transonic speed modes are explained by the conventional stability theory.

However, Ponta and Aref [23] have performed an analysis that appears to predict the observed data well and extend them to a wider range of Reynolds' numbers.

As the discharge Mach number becomes supersonic, the trailing edge shocks become oblique and the origin of the vortex street migrates from the trailing edge to the confluence of the two trailing edge shear layers. Previously available evidence had suggested that only free-stream disturbances are effective in provoking the vortex-shedding instability. In the present example, the visible existence and the fixed location of acoustic waves preclude such a path for antisymmetric upstream-traveling pressure waves. This has the effect of reducing the lateral distance between incipient vortices to the relatively short wake width at the downstream shock location. Nevertheless, significant free shear layer instabilities are thought to be propagated downstream through a Kelvin-Helmholtz mechanism. These phenomena, caused by vortex shedding, also play an important role in loss generation. This is due to low base pressures behind blades with thick trailing edges. The base pressure recovered significantly in transonic flows, where the vortex street changed its character. The anomalous vortex shedding patterns were therefore associated with a reduction in loss. They can also have a role in vortex-induced vibration of the resulting airfoil, which is effectively a bluff body.

The turbine blade and its mounting were extremely stiff, and in this case vortex-induced vibration could be ruled out. The exotic shedding patterns in the blade wakes only occurred when shock waves were present; static pressure differences across the wake appeared to be the driving agent. Schlieren photographs from transonic cascades showed that the interaction between the base flow shear layers and the shock waves are the likely mechanism causing the changes in observed vortex-shedding patterns. There was a strong interaction between the downstream shock waves and the vortex shedding process, but the coupling mechanism was not understood. In a novel use of the hydraulic analogy, the fluctuating water surface was observed by high speed schlieren. This helped clarify the dynamics of the interaction between the shock waves and the shed vortices. The above considerations suggest that the observed changes in vortex shedding from the blunt trailing edges of the transonic cascade in the Mach number range between 0.97 and 1.2 are caused by a similar self-induced oscillation mechanism.

As shown in Figures 16 and 17, shocks are generated at the confluence of the shear layers; the shocks interact with the shear layers. Findings, from schlieren visualization, computational work, and a separate hydraulic analogy experiment, have shown that the shock wave/wake interaction structure at the confluence of the shear layers is particularly dynamic and mobile. This results in the oscillatory flow causing the observed changes in vortex shedding.

#### 4. Conclusions

A wide range of vortex formation and shedding processes was identified in a transonic turbine nozzle cascade. Vortex

formations included the expected horseshoe vortices and secondary flow-related passage vortices and the surprising organized streamwise vorticity on the suction surface. Observations of the streamwise streaks have generally been by surface flow visualization. Further work is needed to characterize the vorticity distribution away from the surface.

Cascade tests established that strong von Kármán vortex shedding occurred over the entire subsonic range of discharge Mach numbers. This resulted in strong base pressure deficits, causing high wake losses and energy separation in the wake. Time-resolved measurements of the Eckert-Weise energy separation phenomenon were made for the first time, explaining anomalies in the wake temperature variations.

At Mach numbers above unity, the von Kármán vortex street was found to be but one of a number of transient, yet distinct, shedding patterns. These corresponded to similar patterns observed in the field of vortex-induced vibration. The occurrence of similar changes in vortex shedding from transonic cascades suggests that the existence of an oscillating body is not a fundamental requirement. The wake instability can be caused by an oscillating pressure field. Shock-induced transonic flow oscillations could also change the modes of vortex shedding. The transonic cascade schlieren photographs showed that the interaction between the base flow shear layers and the shock waves, which form at the Mach numbers between 0.97 and 1.2, is the likely mechanism causing the changes in observed vortex-shedding patterns.

In these investigations on one high-turning nozzle vane cascade, several distinct modes of vortex formation and shedding have been identified. The impact of some of these on turbine performance is potentially harmful. The presence of these disparate vortical structures clearly makes the fluid flow and heat transfer properties of the turbine blading challenging to interpret and predict. For example, it would be useful to introduce a cooling flow in the region of the thick trailing edge and assess its impact on wake behavior and losses.

#### Nomenclature

$C_p$ : Static pressure coefficient  
 $D$ : Diameter of cylinder  
 $M_e$ : Exit isentropic Mach number  
 $P$ : Pressure  
 $PR$ : Pressure ratio  
 $Re$ : Reynolds' number  
 $Tu$ : Free-stream turbulence level, %  
 $t$ : Time  
 $y$ : Normal direction  
 $\lambda$ : Spanwise wavelength.

#### Subscripts

$b$ : Base value  
 $s$ : Static condition  
 $0$ : Stagnation condition.

## Acknowledgments

Appreciation is expressed to Paul Hunt and to the M-10 team of NRC for running the facility and providing excellent support.

## References

- [1] J. Görtler, "Three-dimensional instability of the stagnation point flow with respect to vortical disturbances," in *50 Years of Boundary Layer Research*, H. Görtler and W. Tollmien, Eds., vol. 14, 17, pp. 304–314, Vieweg, Braunschweig, Germany, 1955.
- [2] J. Kestin and R. T. Wood, "On the stability of two-dimensional stagnation flow," *The Journal of Fluid Mechanics*, vol. 44, pp. 461–479, 1970.
- [3] R. G. Williamson and S. H. Moustapha, "Annular cascade testing of turbine nozzle at high exit Mach numbers," *Journal of Fluids Engineering*, vol. 108, pp. 313–320, 1986.
- [4] W. E. Carscallen and P. H. Oosthuizen, "The effect of secondary flow on the redistribution of the total temperature field downstream of a stationary turbine cascade," AGARD CP-469, 1988.
- [5] W. E. Carscallen, T. C. Currie, S. I. Hogg, and J. P. Gostelow, "Measurement and computation of energy separation in the vortical wake flow of a turbine nozzle cascade," *Journal of Turbomachinery*, vol. 121, no. 4, pp. 703–708, 1999.
- [6] E. Eckert and W. Weise, "Messungen der Temperaturverteilung auf der Oberfläche schnell angeströmter unbeheizter Körper," *Forschung auf dem Gebiete des Ingenieurwesens*, vol. 13, no. 6, pp. 246–254, 1942.
- [7] W. E. Carscallen and J. P. Gostelow, "Observations of vortex shedding in the wake from transonic turbine nozzle vanes," in *Proceedings of the 5th International Symposium on Transport Phenomena and Dynamics of Rotating Machinery*, Kaanapali, Hawaii, 1994.
- [8] C. H. K. Williamson and A. Roshko, "Vortex formation in the wake of an oscillating cylinder," *Journal of Fluids and Structures*, vol. 2, no. 4, pp. 355–381, 1988.
- [9] H. P. Wang, S. J. Olson, R. J. Goldstein, and E. R. G. Eckert, "Flow visualization in a linear turbine cascade of high performance turbine blades," *Journal of Turbomachinery*, vol. 119, no. 1, pp. 1–8, 1997.
- [10] J. P. Gostelow, A. Mahallati, S. A. Andrews, and W. E. Carscallen, "Measurement and computation of flowfield in transonic turbine nozzle blading with blunt trailing edges," ASME Paper GT2009-59686, 2009.
- [11] H. D. Schulz and H. D. Gallus, "Experimental investigation of the three-dimensional flow in an annular compressor cascade," *Journal of Turbomachinery*, vol. 110, no. 4, pp. 467–478, 1988.
- [12] A. Weber, H. A. Schreiber, R. Fuchs, and W. Steinert, "3-D transonic flow in a compressor cascade with shock-induced corner stall," *Journal of Turbomachinery*, vol. 124, no. 3, pp. 358–366, 2002.
- [13] M. W. Benner, S. A. Sjolander, and S. H. Moustapha, "Measurements of secondary flows in a turbine cascade at off-design incidence," ASME Paper 97-GT-382, 1997.
- [14] H. P. Hodson and R. G. Dominy, "Off-design performance of a low-pressure turbine cascade," *Journal of Turbomachinery*, vol. 109, no. 2, pp. 201–209, 1987.
- [15] D. E. Halstead, *The use of surface-mounted hot-film sensors to detect turbine-blade boundary-layer transition and separation [M.S. thesis]*, Iowa State University, 1989.
- [16] W. E. Carscallen, H. U. Fleige, and J. P. Gostelow, "Transonic turbine vane wake flows," ASME Paper 96-GT-419, 1996.
- [17] O. Lawaczeck and H. J. Heinemann, "Von Kármán streets in the wakes of subsonic and transonic cascades," AGARD CP-177, 1976.
- [18] G. Cicatelli and C. H. Sieverding, "The effect of vortex shedding on the unsteady pressure distribution around the trailing edge of a turbine blade," ASME Paper 96-GT-359, 1996.
- [19] J. D. Denton, "Loss mechanisms in turbo-machines," *Journal of Turbomachinery*, vol. 115, pp. 621–656, 1993.
- [20] D. J. Mee, N. C. Baines, M. L. G. Oldfield, and T. F. Dickens, "Examination of the contributions to loss on a transonic turbine blade in cascade," *Journal of Turbomachinery*, vol. 114, no. 1, pp. 155–162, 1992.
- [21] C. H. Sieverding, M. Stanislas, and J. Snoeck, "The base pressure problem in transonic turbine cascades," *Journal of Engineering for Power*, vol. 102, no. 3, pp. 711–718, 1980.
- [22] D. R. Buttsworth and T. V. Jones, "A fast-response total temperature probe for unsteady compressible flows," *Journal of Engineering for Gas Turbines and Power*, vol. 120, no. 4, pp. 694–701, 1998.
- [23] F. L. Ponta and H. Aref, "Numerical experiments on vortex shedding from an oscillating cylinder," *Journal of Fluids and Structures*, vol. 22, no. 3, pp. 327–344, 2006.

## Research Article

# Aerothermal Analysis of a Turbine Casing Impingement Cooling System

**Riccardo Da Soghe, Bruno Facchini, Mirko Micio, and Antonio Andreini**

*Energy Engineering Department "S. Stecco", University of Florence, Street S. Marta 3, 50139 Florence, Italy*

Correspondence should be addressed to Riccardo Da Soghe, [dasoghe@brun.de.unifi.it](mailto:dasoghe@brun.de.unifi.it)

Received 19 July 2012; Revised 28 September 2012; Accepted 30 September 2012

Academic Editor: N. Sitaram

Copyright © 2012 Riccardo Da Soghe et al. This is an open access article distributed under the Creative Commons Attribution License, which permits unrestricted use, distribution, and reproduction in any medium, provided the original work is properly cited.

Heat transfer and pressure drop for a representative part of a turbine active cooling system were numerically investigated by means of an in-house code. This code has been developed in the framework of an internal research program and has been validated by experiments and CFD. The analysed system represents the classical open bird cage arrangement that consists of an air supply pipe with a control valve and the present system with a collector box and pipes, which distribute cooling air in circumferential direction of the casing. The cooling air leaves the ACC system through small holes at the bottom of the tubes. These tubes extend at about 180° around the casing and may involve a huge number of impinging holes; as a consequence, the impinging jets mass flow rate may vary considerably along the feeding manifold with a direct impact on the achievable heat transfer levels. This study focuses on the performance, in terms of heat transfer coefficient and pressure drop, of several impinging tube geometries. As a result of this analysis, several design solutions have been compared and discussed.

## 1. Introduction

Impingement with high velocity jets has become an established method for surface cooling or heating in a wide variety of processes and thermal control applications. The use of impingement jets for the cooling of modern aero-engine components is widespread, especially within the hot stationary parts. Since the cooling performance of impinging jets is very high, this method provides an efficient way to manage a component heat load when a sufficient pressure head and geometrical characteristics are available for its implementation. The cooling jets are usually arranged as arrays [1].

Aero-engine casing temperature control is a very effective way to reduce aerodynamic losses and specific fuel consumption due to blade tip clearance. Because of the significant variations of centrifugal and thermal loads which occur at different engine operating conditions, the tip clearance can be extremely variable; such dimensional variation may worsen engine performance and reduce the components' life span [2]. To overcome these issues, the Active thermal Clearance Control (ACC), generally based

on impingement cooling, has been successfully introduced in several applications as described in Halila et al. [3], Beck and Fasching [4], and more recently by Justak and Doux [2]. In such systems, impinging jets are directed towards the external turbine casing by means of a series of circumferential feeding pipes with the final aim of keeping the clearance between blade tip and casing as constant as possible under different engine operating conditions (Figures 1 and 2). Depending on the engine architecture, the cooling air could be bled from the compressor or extracted from the fan flow. The impinging system pressure ratio is then a consequence of the ACC configuration: lower than 1.1 in case of cooling air extracted from the fan flow, while higher  $\beta$  when the coolant comes from the compressor.

The correct evaluation of both the impinging jet mass flow rate (i.e., the characterization of the holes discharge coefficient) and the related heat transfer coefficient is a fundamental activity.

The discharge coefficient ( $C_d$ ) is defined as the ratio of the actual mass flow rate through a hole and the isentropic flow rate. It summarizes all the losses that limit the actual



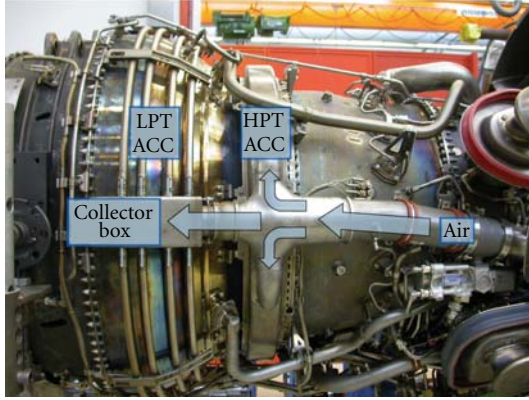


FIGURE 1: ACC system, Ahmed et al. [5].

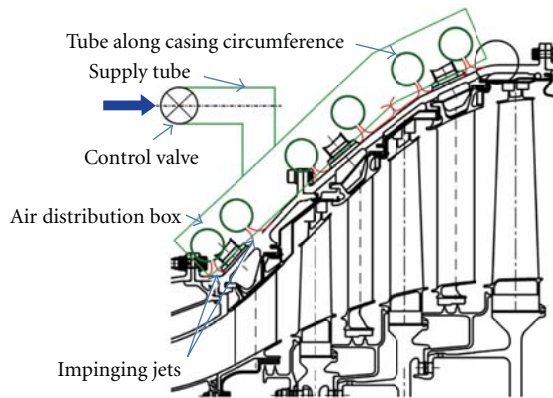


FIGURE 2: Scheme of a LPT ACC system, Ahmed et al. [6].

mass flow rate through a hole: entry pressure losses, internal losses due to friction, and exit losses.

Many parameters may influence the discharge coefficient [7]: geometrical, such as hole shape, hole angle, space between holes, and length to diameter ratio, and fluid-dynamical, such as pressure ratio across the hole and Reynolds and Mach number of the two cross-flows and inside the hole. For this reason, several studies have been carried out on different geometries of holes subjected to a wide range of fluid-dynamics conditions; extensive reviews can be found in Hay and Lampard [8] and in Andreini and DaSoghe [9]. Gritsch et al. [10] have investigated the behaviour of a single hole of large diameter (10 mm); they proposed a method for correlating the discharge coefficients, assuming that pressure losses inside the hole and those related to the hole entry and exit are independent. Internal losses are found to be dependent on the pressure ratio across the hole, while the entry and exit losses depend on the jet to cross-flow momentum ratio. With these hypotheses in mind, Gritsch et al. [11] have studied the influence of the internal cross-flow on shaped holes, while Rowbury et al. [12] proposed a method to quantify the influence of the external cross-flow on the  $C_d$ . More recently, Schulz et al. [13] have performed several experiments, analysing the behaviour of the  $C_d$  under varying internal

and external cross-flow conditions and geometrical angles and using the jet-to-cross-flow momentum ratio to reduce data.

Referring to the heat transfer, measurements of multiple jet impingement arrays can be found in a relevant number of existing publications. Comprehensive reviews on this field have been provided by Martin [15] and Han et al. [16]. Some recent and very interesting contributions have been made by Ahmed and coworkers [5, 6] who have performed some numerical simulations of the flow in a short tube section of an ACC system for a low pressure turbine. The length-to-diameter ratio of the sharp-edged cylindrical nozzles, ranging from 0.25 to 2, was also accounted for. The authors reveal that increasing the Mach number by simultaneously reducing the orifice diameters led to slightly decreasing Nusselt numbers, with average deviations of the order of 14%. The predicted discharge coefficients increased significantly by augmenting the Mach number. The main limiting aspect of these two interesting contributions consists in the fact that the authors do not evaluate the effects of the undercowl flow on the impingement jets.

As mentioned above, many published works deal with heat transfer coefficient due to impinging jets; most of them analyse, by means of experiments or numerical simulations, the behaviour of several hole geometries and arrangements, but it also appears a complete deficiency of studies conducted on a real-engine ACC geometry. Similar conclusions could be pointed out referring to impinging holes discharge coefficient prediction. Indeed, there seems to be a lack of general studies, and therefore of useful design correlations concerning the effects on the discharge coefficient due to the interaction among adjacent holes drilled in cylindrical feeding pipes [9].

Hence, the University of Florence has promoted an internal research project aimed at the characterization of the holes discharge coefficient and heat transfer phenomena of a real-engine ACC geometry. The main goals of this project are to provide a general understanding of the fluid flow and heat transfer characteristics, to develop useful correlations for both the  $C_d$  and the HTC coefficient and, finally, to validate CFD with high quality experimental data. In the framework of the project two test rigs have been developed. The first one, aims to evaluate the discharge coefficient of several jet holes drilled into a circular duct. The tested geometries replicate the final part of a feeding manifold impingement tube used in active clearance control systems. By using the provided experimental data (see [17]) and validated CFD calculations, Andreini and DaSoghe [9] have developed an empirical correlation for the prediction of the impinging holes discharge coefficient: it expresses the  $C_d$  of each hole as a function of the ratio between the hole and the manifold mass velocity and the local value of the pressure ratio. Recently, the authors have revised this correlation to make it sensible to the nozzle length-to-diameter ratio [18]. The second test rig, aims to evaluate the heat transfer coefficient and the adiabatic effectiveness of a multijet impingement array (for which the undercowl flow is considered) which reproduces an active clearance control system of a commercial aircraft. The test rig has



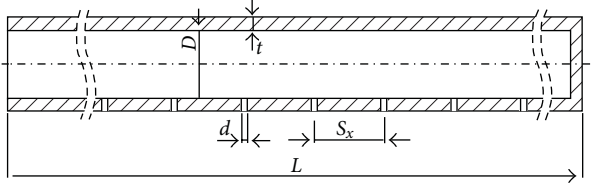


FIGURE 3: Multiple jet section geometry.

provided detailed experimental data that are, nowadays, partially available in the open literature (see [14]).

This paper deals with a simplified 1D code, developed at the University of Florence, aimed at the design of the multiple jet section of an ACC cooling tube. The main purpose of this work is to validate the in-house design tool and, by using its predictions, to point out design practices for such kind of cooling systems.

## 2. Description of the Code

As stressed above, the simplified code deals with the multiple jet section of an ACC cooling tube. Such kind of geometries are depicted in Figure 3.

The aim of the 1D program is to evaluate the mass flow rate through each nozzle of the array and then to calculate the related heat transfer coefficient HTC achieved on the target surface. To do that the code, that is based on a correlative approach, implements two correlations: the first one for the nozzle  $C_d$  and the other one for the HTC evaluation. The implemented correlations are presented in the next section. Within the manifold, the total pressure losses due to friction are neglected. Then, the static pressure profile is determined by the mass flow rate bleeding operated by the holes.

## 3. Discharge Coefficient Correlation

The correlation for the  $C_d$  parameter considered in this study has been recently developed by DaSoghe and Andreini [9, 18]. The expression is the result of an extensive CFD analysis: it expresses the  $C_d$  of each impingement hole as a function of the ratio between the hole and the manifold mass velocity (MVR), the nozzle length-to-diameter ratio ( $t/d$ ) and the local value of the  $\beta_L$  ratio. The discharge coefficient is evaluated using the following expression:

$$C_d = C_1 \cdot \beta_L^{\alpha(t/d)} \cdot g\left(\frac{t}{d}\right) \cdot \left(1 + C_2 \cdot C_3^{C_4 \cdot \text{MVR}^{C_5}}\right), \quad (1)$$

where  $\alpha(t/d)$  and  $g(t/d)$  are second-order polynomial functions of the length-to-diameter ratio and the other coefficients are suitable constants.

Even developed referring to circular cross-section manifold geometries, DaSoghe and Andreini [18] proved the correlation reliability also in case of squared manifold geometries.

The ranges of applicability of the correlation are the following  $\beta = 1.0$  to  $1.65$ ,  $\text{Re}_{\text{channel}} = 0$  to  $6 \cdot 10^4$ , and  $t/d = 0.25$  to  $3$ . With respect to the CFD data, the correlation

TABLE 1: Geometric parameter.

Manifold diameter “ $D$ ”	m
Nozzle diameter “ $d$ ”	m
Manifold thickness “ $t$ ”	m
Holes number “ $n$ ”	—
Holes spacing “ $S_x$ ”	m
Nozzle to wall distance “ $h$ ”	m

TABLE 2: Thermodynamic parameter.

Cooling temperature	K
Wall temperature	K
Overall pressure ratio	—
Discharge pressure	Pa

shows a mean relative error of 1.6% and a maximum error of 4.5%, with a standard deviation of 1.2% (i.e., 95% of the  $C_d$  predicted when using the correlation leads to an error lower than 3% with respect to the CFD data set).

Finally, the correlation has been validated against the experimental data provided by Schulz and co-workers [13].

For further details about the presented correlation and the related validation study, refer to Andreini and DaSoghe papers [9, 18].

## 4. Heat Transfer Coefficient Correlation

The method used to calculate the HTC consists in a procedure that considers two correlations: one to evaluate the HTC peak value on the jet stagnation point, and the other to calculate the HTC value far away from the stagnation region.

The HTC peak value is evaluated using of the following expression:

$$\text{Nu0} = C_6 \text{Re}_d^{C_7} \text{Pr}^{C_8} \left(\frac{S_x}{d}\right)^{C_9} \left(\frac{h}{d}\right)^{C_{10}}, \quad (2)$$

in which the Nu0 represents the Nusselt number peak value (i.e., the Nu at the jet stagnation point). This expression has been derived from Florschuetz and co-workers [19]. The ranges of applicability of the correlation are the following:  $\text{Re}_d = 2500$  to  $80000$ ,  $S_x/d = 5.9$  to  $31.4$ , and  $h/d = 2.9$  to  $17.8$ . Far away from the stagnation region, the local Nusselt number is evaluated as follow:

$$\text{Nul} = \text{Nu0} \left[ 1 - C_{11} \left(\frac{x}{d}\right)^{C_{12}} \right] \exp \left[ C_{13} \left(\frac{x}{d}\right)^{C_{14}} \right], \quad (3)$$

where Nu0 is the Nusselt number evaluated by (2) and  $x$  represents the distance between the considered point and the stagnation point.

## 5. 1D Procedure

The in-house code is composed of two different modules. The first one consists in a performance code: for a given ACC tube geometry and operating condition (see Tables 1 and 2),

TABLE 3: Design code: Geometric parameter.

Manifold diameter “ $D$ ”	m
Manifold thickness “ $t$ ”	m
Holes number “ $n$ ”	—
Holes spacing “ $Sx$ ”	m
Nozzle to wall distance “ $h$ ”	m

TABLE 4: Validation of the 1D code: Analyzed geometries.

	$D$	$d$	$n$	$t/d$	$Sx/d$	$h/d$
Geom 1	12 (mm)	1 (mm)	17	2	12	7
Geom 2	12 (mm)	1 (mm)	133	2	1.5	7

the code evaluates the system performance in terms of heat transfer coefficient distribution and HTC mean value on the target surface.

By means of an iterative procedure, the code first evaluates the isentropic mass flow rate through the generic impingement hole, using the St. Venant equation:

$$\dot{m}_{\text{ideal}} = \frac{P \cdot A}{\sqrt{R \cdot T}} \cdot \sqrt{\frac{2\gamma}{\gamma-1} \left[ \left( \frac{1}{\beta_L} \right)^{1/\gamma} - \left( \frac{1}{\beta_L} \right)^{\gamma+1/\gamma} \right]}. \quad (4)$$

The actual mass flow rate through a generic hole of the array is then calculated using the following expression:

$$\dot{m}_{\text{actual}} = \dot{m}_{\text{ideal}} \cdot C_d, \quad (5)$$

where the  $C_d$  is given in (1). Once the  $\dot{m}_{\text{actual}}$  is evaluated, the code calculates the jet heat transfer coefficient distribution.

The second code's module, consists in a design procedure: starting from some geometrical data and operating conditions (i.e., overall pressure ratio), the code determines the nozzles' diameter in order to obtain a desired level of heat transfer coefficient. In this case the requested geometrical parameters are reported in Table 3.

The procedure starts from the last hole of the array (the hole closest to the manifold endcap) for which the MVR is  $\infty$ . In that case the hole  $C_d$  is function of both the pressure ratio and the  $t/d$  ratio thus it can be easily estimated. Once the  $C_d$  and the isentropic mass flow rate are calculated, the code estimates the hole impinging mass flow rate and then the related mean HTC. If the calculated HTC does not match the imposed one, the code assumes a new hole diameter and then recalculates the  $C_d$ , the isentropic mass flow rate and the jet mean HTC. These steps are repeated until the calculated mean HTC matches the desired value. Once the procedure is converged for the last hole of the array, the code starts to analyse the second last hole of the array and so on.

## 6. Validation of the Code

In order to evaluate the accuracy and reliability of the code, the predictions of the 1-D procedure are compared with the experimental and numerical data provided by Facchini et al. [14] and Andreini and DaSoghe [9]. Two geometries have been considered (Table 4).

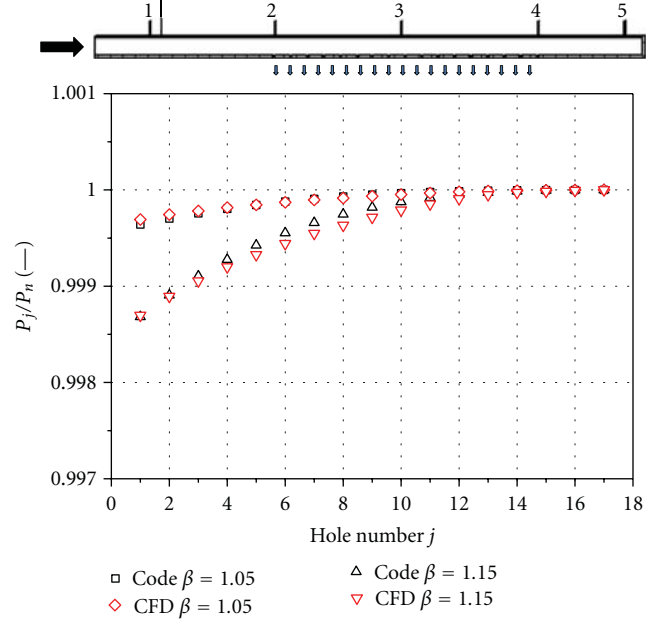


FIGURE 4: Pressure distribution for Geom 1.

The comparisons made for two operating conditions ( $\beta = 1.05$  and  $\beta = 1.15$ ), are provided in terms of pressure distribution (expressed as the ratio of the value in correspondence of the generic hole and value at the end of the feeding pipe  $P_j/P_n$ ), mass flow rate split along the manifold (expressed as the ratio of the generic hole's mass flow rate and the mass flow rate at the inlet of the feeding pipe  $\dot{m}_j/\dot{m}_{\text{tot}}$ ) and HTC profiles.

Figures 4 and 5 show the pressure distribution and the mass flow rate split across the manifold for the geometry labelled “Geom 1”.

The code predictions are compared with the CFD data provided by Andreini and DaSoghe [9]. As shown by the figures, the 1-D code well agrees with the CFD for all the tested operating conditions meaning that a reliable pressure and hole mass flow rates evaluation is provided.

The HTC profiles calculated by the in-house program for the central nozzle of the array are compared with the related experimental data of Facchini et al. [14]. The mentioned test rig consists in a real engine geometry that counts several ACC manifolds. The presence of the undercowl flow is also accounted for during the experiments. The results compared here consist in the spanwise HTC profiles (Figure 6). In the experiments, heat transfer coefficients were determined by means of a steady state technique, measuring wall temperatures on an heated surface, using TLC (thermo liquid crystal) paint. Maximum relative error referred to the heat transfer measurement is under  $\pm 12\%$ . For further details about the experimental procedure and results, please refer to Facchini et al. [14].

In Figure 7, the HTC profile predicted by the simplified procedure in case of Geometry 1 is compared with Facchini et al.'s [14] experimental data.

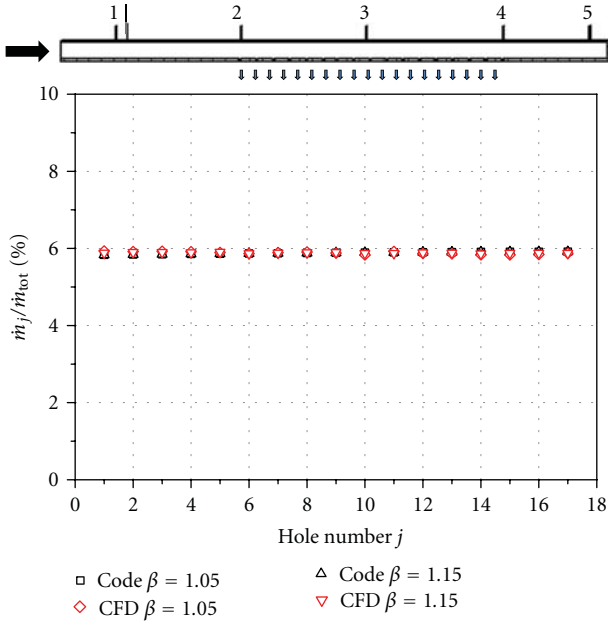


FIGURE 5: Mass flow split distribution for Geom 1 (percent).

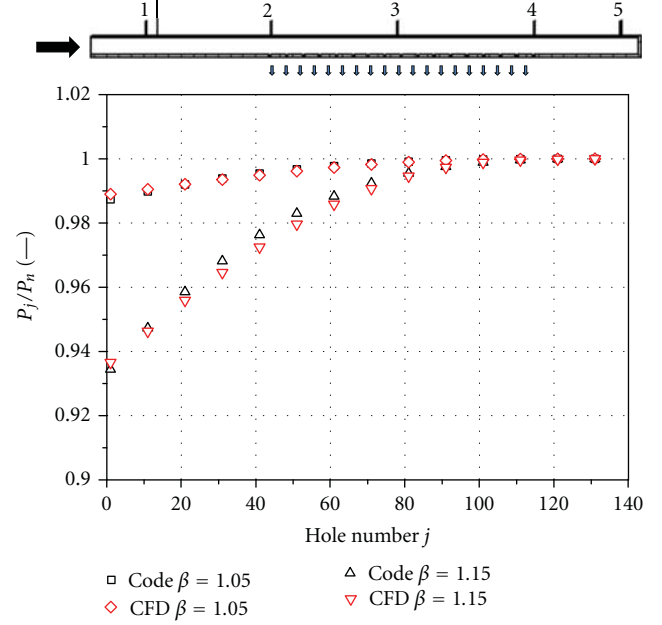


FIGURE 8: Pressure distribution for Geom 2.

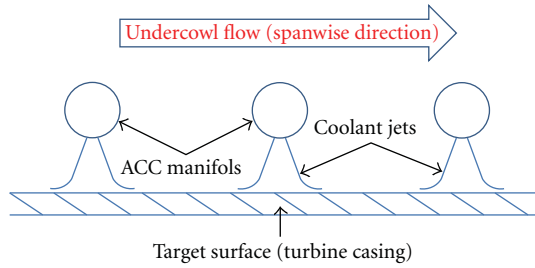
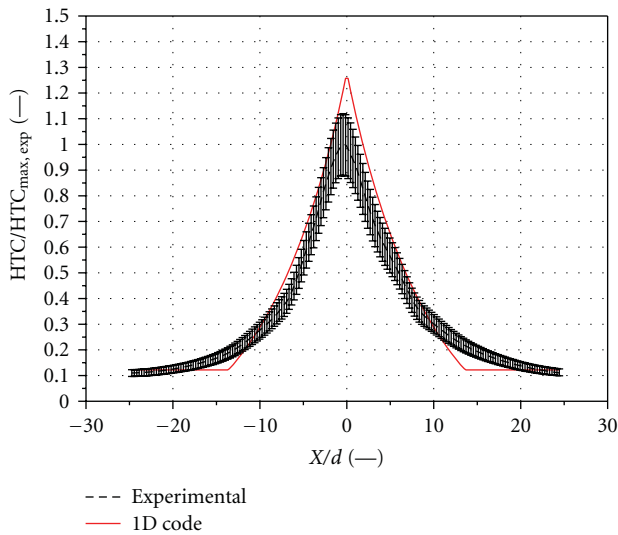


FIGURE 6: Spanwise direction.

FIGURE 7: Heat transfer coefficient distribution, central hole of the array, Geom 1  $\beta = 1.15$  (experimental data from Facchini et al. [14]).

It emerges from the figures that the code is in fairly good agreement with the experiments in term of HTC profiles. The agreement becomes better when considering HTC mean values (that are the key parameter we are looking at). Similar conclusions can be drawn also for the geometry labelled “Geom 2” (Figures 8, 9, and 10).

The 1-D code can be assumed as a reliable tool for the prediction of the HTC related to the multiple jet section of an ACC cooling tube.

## 7. Performance Analysis of Different ACC Cooling Tube Geometries

The developed code has been used to evaluate the performance, in terms of the jet’s mean HTC profile, of different ACC tube geometries.

**7.1. Impact of the  $A_r$  on the Jet Mean HTC Profile.** It emerges from Figure 9 that the mass flow rate split across an ACC cooling tube can be largely variable. Andreini and DaSoghe [9] point out that the mass flow rate split across a given impingement system (i.e., the local MVR) is only related to the pipe area ratio  $A_r$  defined as the ratio of the manifold inlet area and the holes cumulative exit area,

$$A_r = \frac{A_c}{n_{holes} \cdot A_j}. \quad (6)$$

Expression 1 demonstrates that, for each operating condition (i.e., for each  $\beta$  ratio), the discharge coefficient is roughly constant when the MVR is higher than 5. As the MVR is a function of the  $A_r$  parameter, it is possible to design the impingement system in order to assure that the mass flow rate through each hole is roughly the same. Indeed, assuming

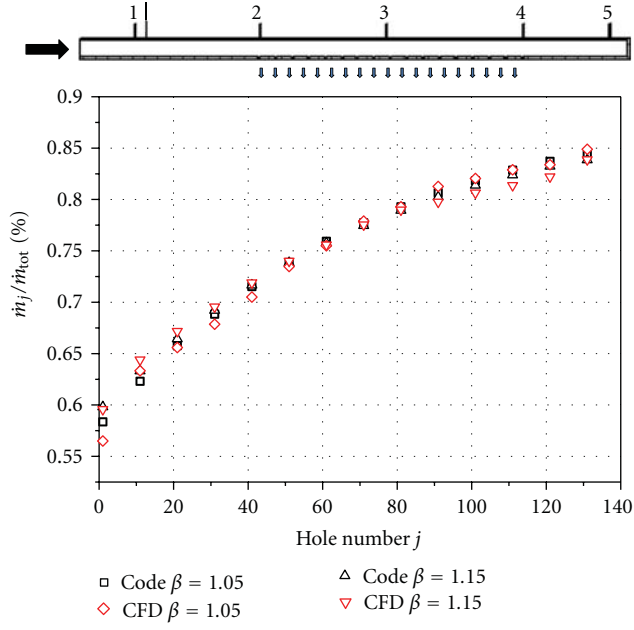


FIGURE 9: Mass flow split distribution for Geom 2 (percent).

that the manifold inlet mass flow rate is equally distributed among the impingement holes, it follows that

$$A_c \cdot (\rho \cdot v)_c = n_{\text{holes}} \cdot A_j \cdot (\rho \cdot v)_j, \quad (7)$$

$$\text{MVR} = \frac{A_c}{n_{\text{holes}} \cdot A_j}. \quad (8)$$

The relations above are satisfied when the  $C_d$  is constant across the impingement system that is, when the MVR is higher than 5 approx. So it can be assumed that the condition:

$$\frac{A_c}{n_{\text{holes}} \cdot A_j} = A_r > 5, \quad (9)$$

defines a design rule for manifolds with equally distributed impinging mass flow rate jets.

Geometries for which the  $A_r$  is greater than 5 lead to a roughly constant impingement jet mass flow rate distribution, while, in case of geometries characterized by a low  $A_r$ , relevant differences in jet mass flow rates across the feeding pipe are expected. This last statement justifies the trends shown in Figures 5 and 9. Geom 1 is characterized by  $A_r = 8.4$  so the mass flow split across the manifold is uniform. In case of Geom 2, for which  $A_r = 1.08$ , the impinging jet mass flow rate varies significantly from the first to the last hole of the array. It is also expected that in case of a low  $A_r$ , the impinging jet HTC could be nonuniform. Figure 11 shows the jet's mean HTC distribution obtained for Geom 2 when  $\beta = 1.05$ . The parameter  $\text{HTC}_{\text{ref}}$  represents the mean heat transfer coefficient evaluated for the last hole of the array of Geom 2 when  $\beta = 1.05$ . The figure reveals that the mean HTC varies from the inlet to the outlet of the manifold by about 25%. This variation might be higher when considering high by-pass ratio turbofans.

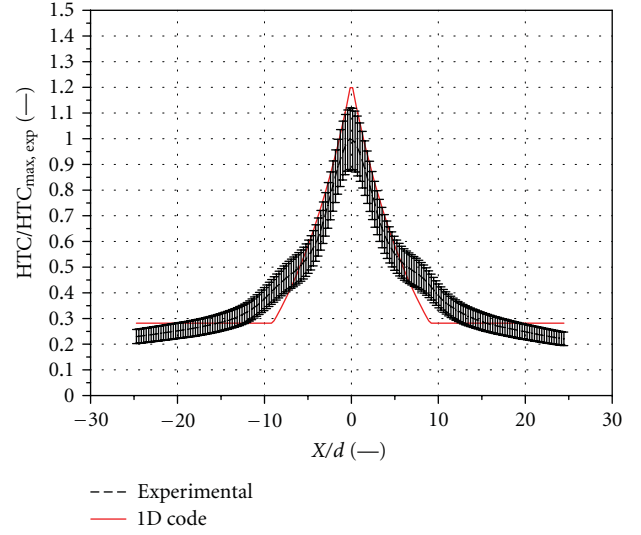


FIGURE 10: Heat transfer coefficient distribution, central hole of the array, Geom 1  $\beta = 1.05$  (experimental data from Facchini et al. [14]).

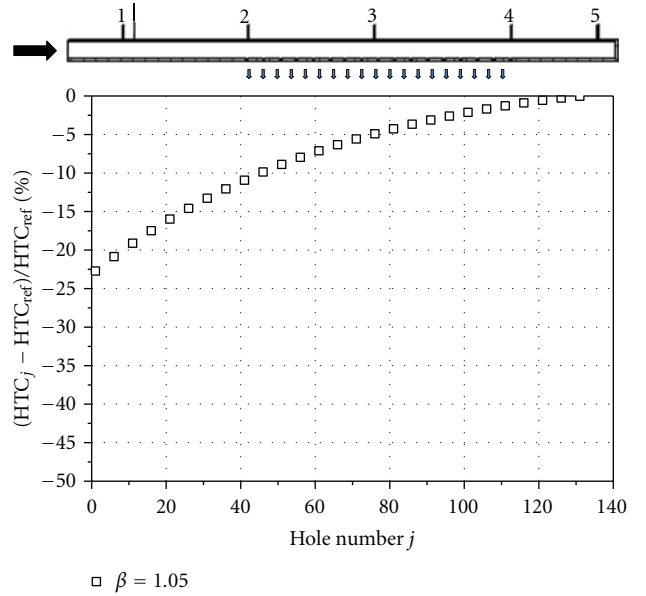


FIGURE 11: Mean heat transfer coefficient distribution for Geom 2 ( $A_r = 1.08$ )  $\beta = 1.05$ .

**7.2. Impact of the Manifold Cross Section on the Jet Mean HTC Profile.** Figure 12 shows the jet mean HTC distribution along the manifold for different values of the  $A_r$  parameter. The profiles are obtained assuming the same overall  $\beta$  ratio ( $\beta = 1.05$ ), the same nozzle length-to-diameter ratio ( $t/d = 2$ ), the same impinging holes diameter  $d = 1$  mm, and the same nozzles number (i.e., the only parameter that changes is the manifold diameter “ $D$ ”).

As discussed above, the mean HTC profiles are flatter as the  $A_r$  increases. More in detail, the HTC profile's variations lie below 5% when the  $A_r$  is higher than 3. The better

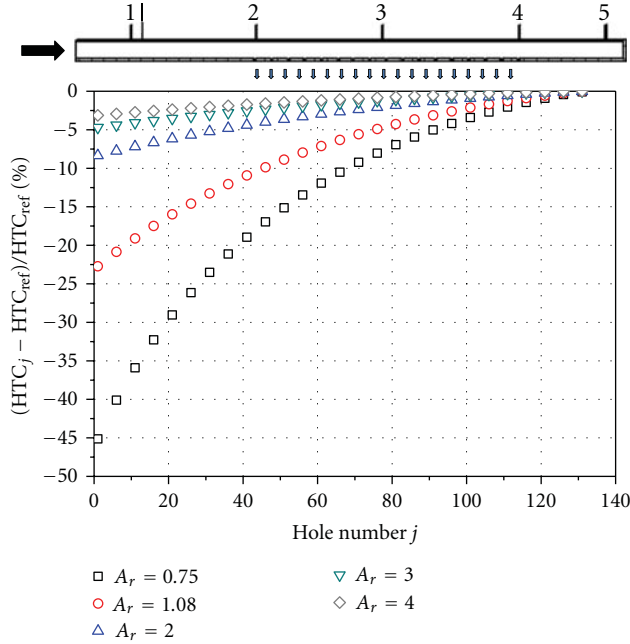


FIGURE 12: Mean heat transfer coefficient distribution varying the  $A_r$  parameter,  $\beta = 1.05$ .

performance obtained with the high  $A_r$  is due to a more uniform mass flow rate split along the manifold. As the mass flow through last hole of the array remains roughly the same, the total mass flow at the manifold inlet increases when the  $A_r$  is higher. Figure 13 shows the mass flow rate at the inlet of the feeding pipe for different  $A_r$  values. The parameter  $\dot{m}_{ref}$  represents the total mass flow at the manifold inlet evaluated for Geom 2 when  $\beta = 1.05$ .

When the  $A_r$  is equal to 3 (i.e., when the changes in the HTC values along the manifold are below 5%) the mass flow rate at the manifold inlet increases, with respect to the nominal case with  $A_r = 1.08$ , by 9%.

The increase of the  $A_r$  by means of the manifold diameter “ $D$ ” augmentation, has a beneficial effect on the jet’s HTC profile uniformity. However, it has to be remarked that as the feeding pipe diameter increases, both the cooling system size and weight increase. Furthermore, the total coolant mass flow rate is higher as well. The last evidence may have a marginal effect in case of cooling air extracted from the fan flow but represents a penalty if the coolant is bled from the compressor.

**7.3. Impact of the  $\beta$  Ratio on the Jet Mean HTC Profile.** In present section, the effects of the overall  $\beta$  ratio are analysed. The impact of the  $\beta$  ratio on the jet’s mean HTC profile is reported in Figure 14. To be consistent with the sensibility analysis previously conducted, the nozzles’ diameter “ $d$ ” have been changed in order to assure, for each case, the same mean HTC value at the last hole of the array. The manifold diameter “ $D$ ” is fixed ( $D = 12$  mm) and the  $t/d$  is equal to 2. Thus, as the  $\beta$  changes, the system  $A_r$  consequently varies.

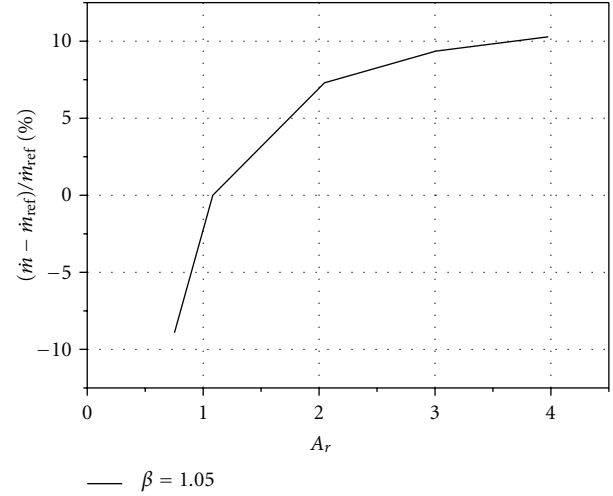


FIGURE 13: Total coolant mass flow rate varying the  $A_r$  parameter,  $\beta = 1.05$ .

Figure 14 shows that the increase of the system’s overall pressure ratio has a beneficial effect on the HTC profile. This last statement can be motivated by observing that the  $\beta$  ratio affects both the isentropic mass flow rate and the impingement holes’ discharge coefficient (i.e., as the  $\beta$  ratio increases both the  $C_d$  and the  $\dot{m}_{ideal}$  result augmented). In order to obtain the same mean HTC value at the last hole of the array, the nozzles’ diameter is then reduced. Thus the  $A_r$  increases significantly as the design pressure ratio is increased explaining the trend shown in Figure 14.

The reduction of the impingement holes’ cross section leads, as the pressure ratio is increased, to an appreciable reduction of the coolant cumulative mass flow rate (Figure 15).

When  $\beta = 1.2$ , the HTC profile’s variations lie below 5% and the total coolant mass flow rate is reduced by 13% with respect to the case when  $\beta = 1.05$ .

**7.4. Impact of the Nozzles’ Diameter Distribution on the Jet Mean HTC Profile.** In the previous sections, for each considered geometry, the nozzles’ diameter is uniform moving from the first to the last hole of the array. However in order to mitigate the changes in the nozzles’ mass flow rate, the impinging manifold could be designed considering a non-uniform holes’ diameter distribution. The 1-D code is then used to design manifold geometries characterized by nozzles with different diameter. Each hole’s diameter is determined imposing the same mean HTC value (i.e., the designed impinging manifold guarantee a uniform HTC level moving from the first to the last nozzle of the array). When considering a manifold diameter  $D = 12$  mm,  $\beta = 1.05$ , and  $t/d = 2$ , the nozzles’ diameter distribution across the manifold calculated by the 1-D program is shown in Figure 16.

The first nozzle’s diameter is increased by 80% with respect to the last one. For this manifold geometry, the calculated cumulative coolant mass flow rate is roughly



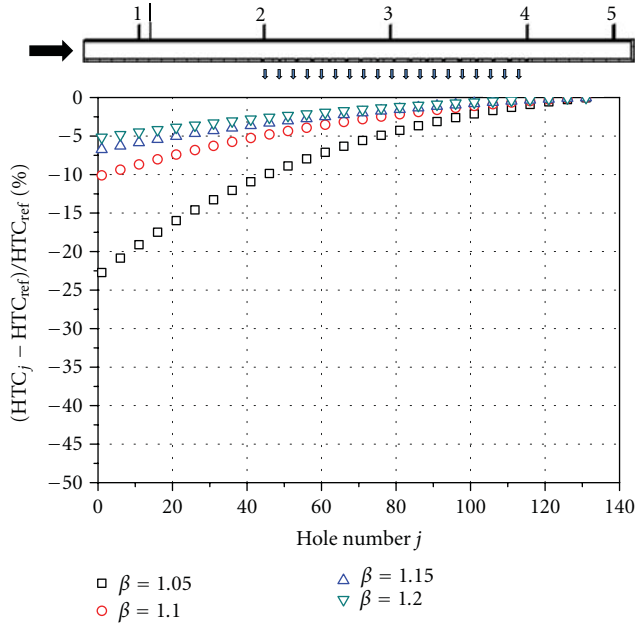


FIGURE 14: Mean heat transfer coefficient distribution varying the  $\beta$  parameter.

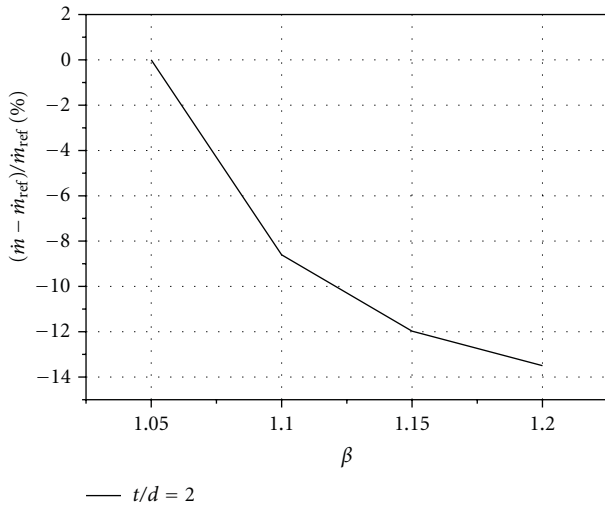


FIGURE 15: Total coolant mass flow rate varying the  $\beta$  parameter.

26% higher than those obtained in case of uniform holes' diameter  $d = 1$  mm.

Figure 17 reports the nozzles' diameter distribution calculated in case of different manifold diameter  $D$ . As expected, the changes in the impinging holes diameter is reduced as the feeding pipe cross section is augmented. The last evidence also results in a reduction of the total coolant mass flow rate, with respect to the case for which  $D/D_{ref} = 1$  (i.e.,  $D = 12$  mm), Figure 18.

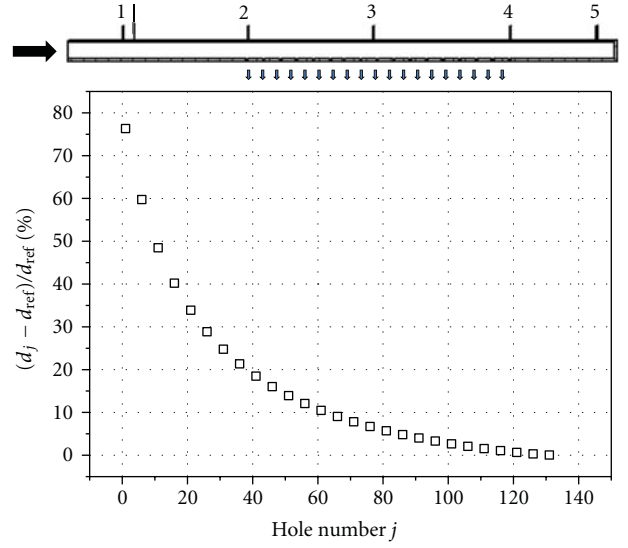


FIGURE 16: Nozzles' diameter distribution across the manifold  $\beta = 1.05$ ,  $D = 12$  mm, and  $t/d = 2$  ( $d_{ref} = 1$  mm).

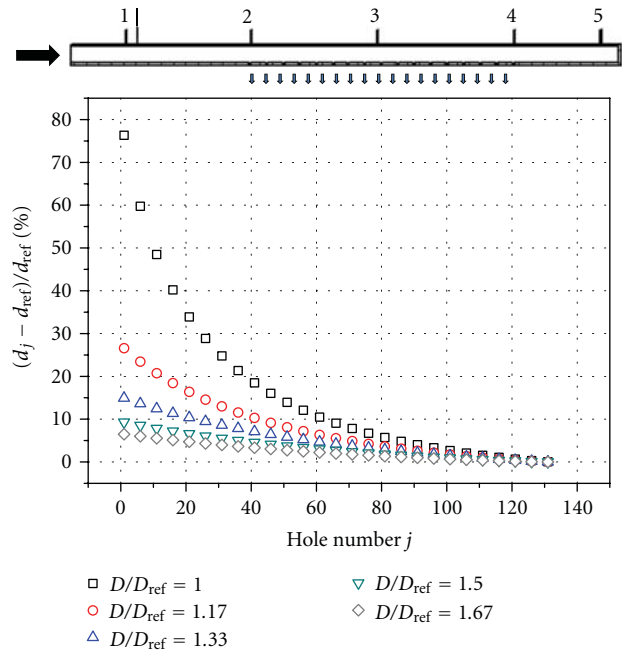


FIGURE 17: Nozzles' diameter distribution across the manifold  $\beta = 1.05$ ,  $t/d = 2$  varying the manifold diameter ( $d_{ref} = 1$  mm and  $D_{ref} = 12$  mm).

## 8. Conclusions

This paper deals with a simplified 1-D code aimed at the design of the multiple jet section of an ACC cooling tube. The 1-D program is able to evaluate the mass flow rate through each nozzle of the array and then to calculate the related heat transfer coefficient (HTC) achieved on the target surface.

The code has been validated by means of both numerical and experimental data. Once validated, the program has been

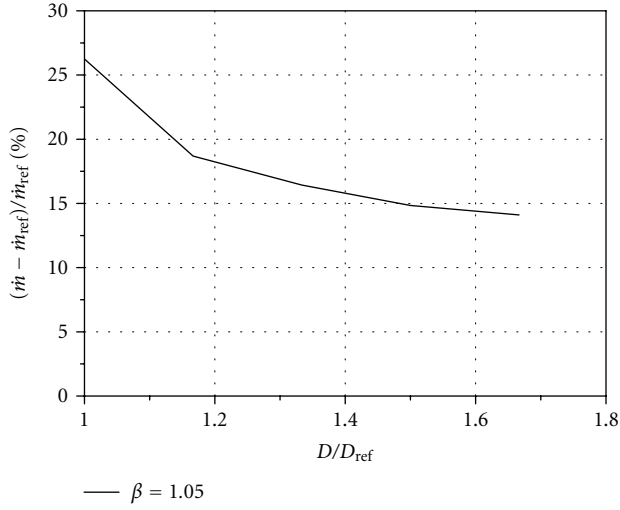


FIGURE 18: Total coolant mass flow rate varying the  $D/D_{ref}$  parameter.

used to point out some design practices for such cooling systems.

It emerges from the study that the mass flow rate split across an ACC cooling tube can be largely variable. In that way, the key parameter is the pipe area ratio  $A_r$  defined as the ratio of the manifold inlet area and the holes cumulative exit area. More in detail, geometries for which the  $A_r$  is greater than 5 lead to a roughly constant impingement jet mass flow rate distribution while, in case of geometries characterized by a low  $A_r$ , relevant differences in jet mass flow rates across the feeding pipe are expected. Variations in the mass flow rate split across an ACC cooling tube result in HTC profile nonuniformities that should be avoided or reduced for a correct system design.

The augmentation of the pipe  $A_r$  (by means of the increase of the manifold diameter) has a direct positive effect on the HTC profile uniformity. However, these solutions have few drawbacks: the increase of both the weight and size of the cooling system.

The role of the operating conditions on the manifold design has been considered. The calculations reveal that once designed considering high overall pressure ratio, the impinging system performs rather better. This last evidence has been motivated when observing that the increase of the pressure ratio leads to an augmentation of both the nozzles' discharge coefficient and the related isentropic mass flow rate. Thus, when imposing always the same mean HTC value at the last hole of the array, the increase of the  $\beta$  ratio involves a higher pipe  $A_r$ . The coolant total mass flow rate is also reduced as the overall pressure ratio is augmented.

Finally, manifold geometry with non-uniform nozzles' diameter have been considered. In order to assure a uniform heat load, the impinging holes' diameter changes considerably across the manifold and the cumulative coolant mass flow rate is increased as well. In case of coolant air extracted from the fan flow, this kind of arrangement could be considered to limit the ACC system size and weight.

## Nomenclature

$A_c$ :	Tube internal area(m <sup>2</sup> )
$A_j$ :	Impingement hole area (m <sup>2</sup> )
$A_r$ :	Area ratio $A_c/(n_{holes} \cdot A_j)$ (—)
$d$ :	Cooling hole diameter (mm)
$d_{ref}$ :	Cooling hole reference diameter (1 mm) (mm)
$D$ :	Tube internal diameter (mm)
$D_{ref}$ :	Tube internal reference diameter (12 mm) (mm)
$h$ :	Holes exit to target surface distance (m)
$k$ :	Surface thermal conductivity (W/mK)
$L$ :	Tube length (mm)
$\dot{m}$ :	Mass flow rate (kg/s)
Ma:	Mach number (—)
Nu:	Nusselt number $HTCd/k$ (—)
$P$ :	Pressure (Pa)
$\dot{Q}$ :	Heat flux (W/m <sup>2</sup> )
$R$ :	Gas constant (J/kgK)
Re:	Reynolds number (—)
$S$ :	Pitch (mm)
$t$ :	Nozzle length (mm)
$T$ :	Temperature (K)
$x$ :	Distance between the considered point and the stagnation point (m).

## Acronyms

ACC:	Active clearance control
$C_d$ :	Discharge coefficient (—)
HTC:	Heat transfer coefficient $\dot{Q}/(T_{aw} - T_w)$ (W/m <sup>2</sup> K)
MV:	Mass velocity $\rho v$ (kg/sm <sup>2</sup> )
MVR:	Mass velocity ratio $(\rho v)_j/(\rho v)_c$ (—).

## Greek Letters

$\beta$ :	Global pressure ratio (P@manifold inlet/P discharge) (—)
$\beta_L$ :	Local pressure ratio (—)
$\mu$ :	Air viscosity (kg/ms)
$\rho$ :	Air density (kg/m <sup>3</sup> ).

## Subscripts

av:	Averaged value
aw:	Adiabatic wall
c:	Main channel
d:	Discharge conditions
exp:	Experimental value
max:	Maximum value
$n$ :	Last hole of the array
is:	Isentropic
$j$ :	Jet impingement hole
ref:	Reference value
$s$ :	Static
$t$ :	Total

$w$ : Wall

$x$ : Streamwise direction.

## Acknowledgment

The authors wish to express their gratitude to F. Maiuolo and L. Tarchi for providing the experimental data.

## References

- [1] J. C. Han, J. S. Park, and C. K. Lei, "Heat transfer enhancement in channels with turbulence promoters," *Journal of Engineering for Gas Turbines and Power*, vol. 107, no. 3, pp. 628–635, 1985.
- [2] J. F. Justak and C. Doux, "Self-acting clearance control for turbine blade outer air seals," in *Proceedings of ASME Turbo Expo (GT2009-59683)*, pp. 1229–1237, June 2009.
- [3] E. Halila, D. Lenahan, and T. Thomas, *High Pressure Turbine Test Hardware*, NASA CR-167955, 1982.
- [4] B. Beck and W. Fasching, *CF6 Jet Engine Performance Improvement—Low Pressure Turbine Active Clearance Control*, NASA CR-165557, 1982.
- [5] F. Ahmed, B. Weigand, and K. Meier, "Heat transfer and pressure drop characteristics for a turbine casing impingement cooling system," in *Proceedings of the ASME International Heat Transfer Conference, IHTC14-22817*, vol. 5, Washington, DC, USA, August 2010.
- [6] F. Ahmed, R. Tucholke, B. Weigand, and K. Meier, "Numerical investigation of heat transfer and pressure drop characteristics for different hole geometries of a turbine casing impingement cooling system," in *Proceedings of ASME Turbo Expo, GT2011-45251*, pp. 1095–1108, Vancouver, BC, Canada, 2011.
- [7] A. H. Lefebvre, *Gas Turbine Combustion*, Taylor & Francis, 1998.
- [8] N. Hay and D. Lampard, "The discharge coefficient of flared film cooling holes," in *Proceedings of ASME Turbo Expo, 95-GT-15*, June 1995.
- [9] A. Andreini and R. DaSoghe, "Numerical characterization of aerodynamic losses of jet arrays for gas turbine applications," *Journal of Engineering for Gas Turbines and Power*, vol. 134, no. 5, article 052504, 8 pages, 2012.
- [10] M. Gritsch, A. Schulz, and S. Wittig, "Method for correlating discharge coefficients of film-cooling holes," *AIAA Journal*, vol. 36, no. 6, pp. 976–980, 1998.
- [11] M. Gritsch, A. Schulz, and S. Witting, "Effect of internal coolant crossflow orientation on the discharge coefficient of shaped film cooling holes," in *Proceedings of ASME Turbo Expo, 99-GT-40*, 1999.
- [12] D. A. Rowbury, M. L. G. Oldfield, and G. D. Lock, "A method for correlating the influence of external crossflow on the discharge coefficients of film cooling holes," *Journal of Turbomachinery*, vol. 123, no. 2, pp. 258–265, 2001.
- [13] A. Schulz, M. Gritsch, and S. Wittig, "Effect of crossflows on the discharge coefficient of film cooling holes with varying angles of inclination," in *Proceedings of ASME Turbo Expo, 2001-GT-0134*, 2001.
- [14] B. Facchini, F. Maiuolo, L. Tarchi, and D. Coutandin, "Heat transfer and effectiveness evaluation of multiple impingement jet arrays for an active clearance control system," *ISAIF (ISAIF10-58)*, 2010.
- [15] H. Martin, "Heat and mass transfer between impinging gas jets and solid surfaces," *Advances in Heat Transfer*, vol. 13, pp. 1–60, 1977.
- [16] J. C. Han, S. Dutta, and S. V. Ekkad, *Gas Turbine Heat Transfer and Cooling Technology*, Taylor & Francis, 1st edition, 2000.
- [17] R. DaSoghe, B. Facchini, F. Maiuolo, M. Micio, and L. Tarchi, "Discharge coefficient characterization of jet array impingement holes for an active clearance control system," in *Proceedings of the 9th ETC Conference*, vol. 252, Istanbul, Turkey, March 2011.
- [18] R. DaSoghe and A. Andreini, "Numerical characterization of pressure drop for turbine casing impingement cooling system," in *Proceedings of ASME Turbo Expo, GT2012-68787*, 2012.
- [19] L. W. Florschuetz, C. R. Truman, and D. E. Metzger, "Streamwise flow and heat transfer distributions for jet array impingement with crossflow," *Journal of Heat Transfer*, vol. 103, no. 2, pp. 337–342, 1981.